NASA/CR-20205011099/VOL1

Acoustics of Future Low-Emissions Combustor Technology

Volume 1: Final Report

Duane McCormick, Jordan Snyder, Wookyung Kim, and Jeffrey Mendoza
United Technologies Research Center, East Hartford, Connecticut

December 2020

NASA STI Program . . . in Profile

Since its founding, NASA has been dedicated to the advancement of aeronautics and space science. The NASA Scientific and Technical Information (STI) Program plays a key part in helping NASA maintain this important role.

The NASA STI Program operates under the auspices of the Agency Chief Information Officer. It collects, organizes, provides for archiving, and disseminates NASA's STI. The NASA STI Program provides access to the NASA Technical Report Server—Registered (NTRS Reg) and NASA Technical Report Server—Public (NTRS) thus providing one of the largest collections of aeronautical and space science STI in the world. Results are published in both non-NASA channels and by NASA in the NASA STI Report Series, which includes the following report types:

- TECHNICAL PUBLICATION. Reports of completed research or a major significant phase of research that present the results of NASA programs and include extensive data or theoretical analysis. Includes compilations of significant scientific and technical data and information deemed to be of continuing reference value. NASA counter-part of peer-reviewed formal professional papers, but has less stringent limitations on manuscript length and extent of graphic presentations.

- TECHNICAL MEMORANDUM. Scientific and technical findings that are preliminary or of specialized interest, e.g., "quick-release" reports, working papers, and bibliographies that contain minimal annotation. Does not contain extensive analysis.

- CONTRACTOR REPORT. Scientific and technical findings by NASA-sponsored contractors and grantees.

- CONFERENCE PUBLICATION. Collected papers from scientific and technical conferences, symposia, seminars, or other meetings sponsored or co-sponsored by NASA.

- SPECIAL PUBLICATION. Scientific, technical, or historical information from NASA programs, projects, and missions, often concerned with subjects having substantial public interest.

- TECHNICAL TRANSLATION. English-language translations of foreign scientific and technical material pertinent to NASA's mission.

For more information about the NASA STI program, see the following:

- Access the NASA STI program home page at http://www.sti.nasa.gov

- E-mail your question to help@sti.nasa.gov

- Fax your question to the NASA STI Information Desk at 757-864-6500

- Telephone the NASA STI Information Desk at 757-864-9658

- Write to:
  NASA STI Program
  Mail Stop 148
  NASA Langley Research Center
  Hampton, VA 23681-2199

NASA/CR-20205011099/VOL1

Acoustics of Future Low-Emissions Combustor Technology

Volume 1: Final Report

Duane McCormick, Jordan Snyder, Wookyung Kim, and Jeffrey Mendoza
United Technologies Research Center, East Hartford, Connecticut

Prepared under Contract NNC16CA39C

National Aeronautics and
Space Administration

Glenn Research Center
Cleveland, Ohio 44135

December 2020

Acknowledgments

This is the Final Report for the NRA effort "Acoustics of Future Low-Emissions Combustor Technology," Principal Investigator Dr. Duane McCormick. The work was sponsored by the NASA Advanced Air Vehicles Program, Advanced Air Transport Technology Project, under Contract NNC16CA39C. The NASA Technical Monitor was Dr. Lennart S. Hultgren, NASA Glenn Research Center.

This work was sponsored by the Advanced Air Vehicle Program
at the NASA Glenn Research Center

Level of Review: This material has been technically reviewed by NASA technical management.

Available from

NASA STI Program
Mail Stop 148
NASA Langley Research Center
Hampton, VA 23681-2199

National Technical Information Service
5285 Port Royal Road
Springfield, VA 22161
703-605-6000

This report is available in electronic form at http://www.sti.nasa.gov/ and http://ntrs.nasa.gov/

Table of Contents

Acoustics of Future Low-Emissions Combustor Technology
Volume 1: Final Report

Duane McCormick, Jordan Snyder, Wookyung Kim, and Jeffrey Mendoza
United Technologies Research Center
East Hartford, Connecticut 06108

Executive Summary

This document is the final report of NRA contract NNC16CA39C that was conducted over the period September 2016 through November 2019. This study leveraged hardware developed under NRA N+3 Combustor Technology Contract (NNC14CA30C) which developed, designed and tested a N+3, low-emissions, high-OPR compact combustor for a single-aisle advanced concept aircraft.

The overall goal of this program was to develop a first of its kind database of detailed unsteady measurements characterizing noise sources of advanced (N+3) low-emissions aero-combustors. The program addresses the need for fundamental combustion noise experiments which, in the near term, enable improvements to reduced-order models for use in system level noise assessments at the preliminary design stage for advanced air transport vehicles. In the long term, this program addresses validation needs of high-fidelity prediction methods suited for detailed multi-disciplinary acoustics/emissions combustor design.

The key finding of this study was a modified pressure scaling which employs a model-based acoustic transfer function to relate combustor dynamic pressure to unsteady heat release was found to enable legacy scaling laws over a wide range of the N configuration (RQL-type combustor) and the N+3 configuration. Certain off-design conditions for the N+3 configuration, specifically, combustor dynamic pressure for *FAR* and T_3 excursions were found to vary significantly from the legacy scaling laws. Positive *FAR* excursions actually reduced the noise level apparently by improving the flame stability. Such results may suggest broadband combustor noise reduction strategies for advanced aero-combustors.

UHR (Unsteady Heat Release) imaging (via chemiluminescence) was used to compute the direct noise field and perform multi-point statistical analysis of the UHR field from which integral length scales, convective speeds and propagation directions of UHR structures, and dominate source locations were quantified. Comparison of the computed direct noise field to measured dynamic pressures suggests the indirect noise field was a significant component of the total dynamic pressure inside the combustor for this study.

Introduction

Acoustic assessments of future low-emissions combustor technology currently rely on semi-empirical OEM-developed tools rooted in 1970's era combustor technology, and little capability exists today to reliably assess the acoustic impact of emerging combustor technologies. Fundamental combustion noise experiments are needed, in the near term, to enable improved reduced-order models for use in system level noise assessments at the preliminary design stage and, in the long term, to address validation needs of high-fidelity prediction methods suited for detailed multi-disciplinary acoustics/emissions combustor design. Without combustion noise research, there is a significant risk of setting long-term (N+3) combustor technology directions that unnecessarily compromise community-noise impact and thereby jeopardize overall goals. The work directly supports the NASA Aeronautics Mission Research Directorate's Ultra-Efficient Commercial Vehicles thrust area.

The goal of this NRA contract is to perform tests on a representative N+3 combustor design, as well as a reference N design, to assess how well existing scaling laws capture the new combustor features and conditions needed to meet N+3 emissions and performance requirements. Detailed multi-point unsteady heat-release measurements, in combination with unsteady pressure measurements, were obtained to provide noise source data for the statistical characterization of the direct noise field. Analysis of this data has determined which legacy scaling parameters require reassessment to enable accurate combustion noise predictions via semi-empirical scaling laws for advanced N+3 air transport vehicles. In addition, an optical technique for unsteady temperature measurements was evaluated near the combustor exit as a means for providing boundary conditions for indirect-noise models.

This work provides a first-time understanding of the N+3 combustor direct noise source given the radical departure from legacy N combustor designs, operating conditions, fuel-air distribution, and flame anchoring techniques. A first of its kind database of detailed unsteady measurements characterizing noise sources of advanced (N+3) low-emissions combustors has been developed. The resulting understanding will inform improvements needed for legacy semi-empirical models used to make far-field combustion noise predictions.

Background

Development of future aircraft configurations targeting dramatic reductions in noise and emissions will require consideration of non-traditional engine and airframe noise sources. In particular, combustion noise is now recognized as a key technical challenge in meeting future N+2 and N+3 targets (Table 1).

v2013.1

TECHNOLOGY BENEFITS*	TECHNOLOGY GENERATIONS (Technology Readiness Level = 4-6)		
	N+1 (2015)	N+2 (2020**)	N+3 (2025)
Noise (cum margin rel. to Stage 4)	-32 dB	-42 dB	-71 dB
LTO NOx Emissions (rel. to CAEP 6)	-60%	-75%	-80%
Cruise NOx Emissions (rel. to 2005 best in class)	-55%	-70%	-80%
Aircraft Fuel/Energy Consumption‡ (rel. to 2005 best in class)	-33%	-50%	-60%

* Projected benefits once technologies are matured and implemented by industry. Benefits vary by vehicle size and mission. N+1 and N+3 values are referenced to a 737-800 with CFM56-7B engines, N+2 values are referenced to a 777-200 with GE90 engines

** ERA's time-phased approach includes advancing "long-pole" technologies to TRL 6 by 2015

‡ CO_2 emission benefits dependent on life-cycle CO_{2e} per MJ for fuel and/or energy source used

Table 1: NASA goals for next-generation aircraft performance, emissions, and noise

The continuing trend toward higher bypass ratio in modern turbofans has significantly reduced jet and fan noise, elevating the importance of core noise **[1]**. In addition, current scaling laws suggest a 6 dB increase in combustion noise due to higher operating pressure **[2]**. The situation is further aggravated by the low-frequency character of combustion noise (200-500Hz) which is less amenable to shielding by the airframe.

Because of the historically important ranking of noise sources, the jet exhaust and fan have benefited from decades of sustained research investment in acoustic modeling, simulation, experimental diagnostics, and noise control technology, while aero-engine combustor acoustics has received comparatively little attention. As a result, acoustic assessments of future low-emissions combustor technology have relied on semi-empirical OEM-developed tools rooted in 1970s era combustor technology, and no capability exists today to reliably assess the acoustic impact of emerging technologies. Meanwhile, low-emissions technology has been rapidly advancing through joint NASA-Industry efforts over the past 5 years. Without complementary efforts aimed at combustor acoustics, there is significant risk of setting long-term combustor technology directions which unnecessarily compromise community noise impact and thus jeopardize overall N+2/N+3 goals.

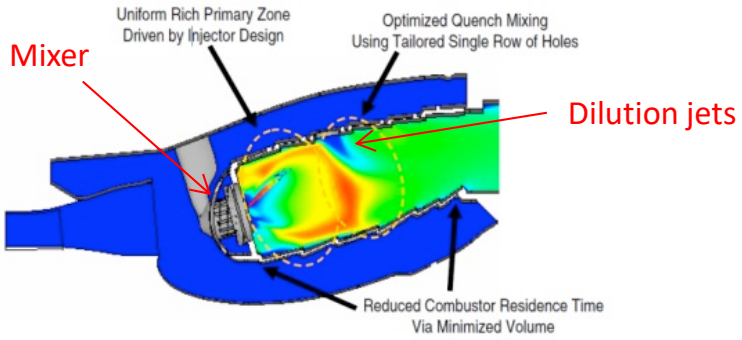

Figure 1: N+1 combustor design

Legacy combustor designs have all had generic features that create a rich front-end to provide robust flame stabilization, and a variety of secondary/dilution air holes along the length of the combustor to provide high combustion efficiency (i.e. complete CO burnout) and tailoring of the temperature profile entering the turbine. Throughout the years this combustor design was refined and became known as a rich-quench-lean or "RQL" combustor. Some manufacturers have started to move away from this design given challenges with minimizing emissions, primarily nitrogen oxide, but this basic combustor design still maintains a strong presence in legacy products and in some cases even N+1 combustor designs as shown in Fig. 1 **[3]**. In these RQL combustors, fuel and air are mixed using high shear created by a multi-pass injector at the front of the combustor. The rich flame is stabilized by the recirculation zones created by strong residual swirl from the mixer. Downstream of the stabilization region, the flame is quenched by dilution air jets to create an overall lean flame for the remainder of the fuel burn.

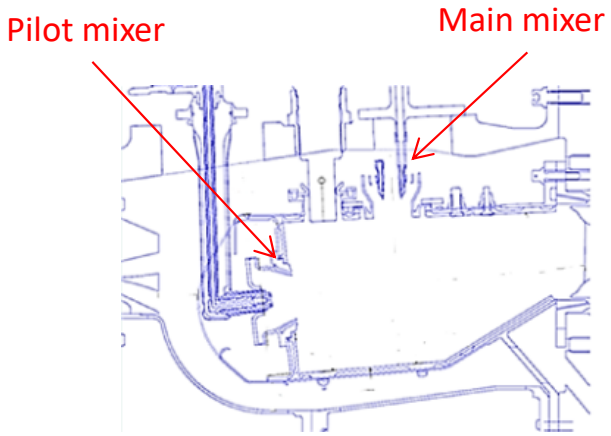

Figure 2: N+2 combustor design

NASA, Pratt & Whitney, and UTRC have partnered to develop an N+2 combustor design (Contract NNC10BA12B) **[4]** to meet future emissions requirements and higher thermal efficiency. The former requirement is achieved by lean burning throughout the combustor and the latter is achieved by higher OPR. Figure 2 shows the basic features of the proposed design **[5]**, an Axially Controlled Stoichiometry (ACS) combustor. The N+2 combustor introduces

axial staging using separate pilot and main injectors, having distinct functions and design. The pilot and main injectors both mix fuel and air, however, the pilot injector provides a stable lean flame for low power conditions and the main is fueled at higher power conditions and is stabilized by hot products from the pilot flame.

In addition to an N+2 combustor design NASA, UTRC, and Pratt & Whitney have just recently have explored combustor designs to meet more challenging N+3 requirements (NRA Contract NNC14CA30C) **[6]**. The N+3 combustor being designed under this contract leverages the combustor architecture developed to meet N+2 requirements but will be a scaled variant to meet the more stringent N+3 requirements.

Working from the D8.6 concept aircraft and corresponding SGTF2065 engine cycle **[7]** the N+3 combustor program defined an overall layout of the N+3 combustor. Given the engine cycle and thrust class of the SGTF2065 study cycle a mean-line turbomachinery analysis was completed to calculate compressor and turbine information including vane and blade elevations. This geometric information was then used, together with the cycle conditions, to calculate approximate combustor dimensions, ensuring an appropriate match to the compressor exit and turbine inlet geometries, and allowing adequate length and volume for the combustor-section aerodynamic and aerothermal functions **[8]**. With these inputs taken into consideration, a rig design (Fig. 3) has been developed which accurately represents a single sector consistent with the SGTF2065 engine cycle.

Table 2 summarizes some of the key differences between legacy and future-generation aero-combustors. Changes in these key characteristics are expected to influence the nature of the combustion noise sources and thus impact the ability of legacy modeling tools to accurately predict the generation of combustion noise.

		Generation			
		Legacy	N and N+1	N+2	N+3
Characteristics	$\phi_{front\text{-}end}$	Stoichiometric	Rich	Lean	Lean
	Fuel Injection	Non-PM	Non-PM	Non-PM / PM	Non-PM / PM
	Flame Anchoring	RZSF	RZSF	RZSF/ RJIC	RZSF/ RJIC

PM: Pre-mix
RZSF: Recirculating Zone Stabilized Flame
RJIC: Reacting Jet In Crossflow

Table 2: Summary of differences between aero-combustor generations expected to impact combustion noise

Combustion noise physics & prediction

In the context of aero-engine applications combustion generates so-called “direct noise” resulting directly from the unsteady combustion process, as well as “indirect noise” generated as

temperature fluctuations (caused by combustion) and vortical structures that are convected through the turbine and exhaust nozzle. The relative importance of these mechanisms is uncertain, but modeling of indirect noise has received increased attention in recent years (see e.g. **[9]**). A key missing piece required to close the indirect noise problem is knowledge of unsteady thermal boundary conditions imposed by the combustion process. Since the combustion phenomena driving direct noise also drive temperature fluctuations which cause indirect noise, the direct noise problem is arguably the more fundamental of the two; thus, in the interest of brevity the following discussion focuses on direct noise.

Methods for predicting direct combustion noise can be broadly categorized in a hierarchy of approaches, similar in principle to those used in the more mature jet and fan noise areas. At the highest level of fidelity are approaches which aim to solve the compressible Navier-Stokes equations via large-eddy simulation (LES) to directly capture the acoustic field while resolving the unsteady reactive flow (for example, Ihme, et al. **[10]**). With the most advanced reacting LES computational tools, detailed flame/ turbulence interactions can be captured, but these are still limited by the quality of the turbulent sub-grid scale models and combustion sub-models. These methods are computationally expensive and have limited utility as OEM design tools.
The next level of fidelity is offered by hybrid methods, which rely on acoustic analogies in various forms where equivalent sources describing sound generation are introduced in acoustic propagation models. Here, the space-time characteristics of the acoustic sources are first computed or estimated using simplified CFD models and then analytical or Finite-Element based tools are used to solve linearized propagation models to determine the acoustic field.
Although hybrid methods for combustion noise prediction have made significant strides in recent years, their application has been limited to canonical problems and simplified geometries, and significant further development and validation is needed before such methods can be reliably used for acoustic assessment of advanced combustor technologies.

Due to the aforementioned challenges, combustor noise assessments have relied heavily on semi-empirical methods. These include commonly used methods based on OEM-proprietary engine and rig data, such as the models by Mathews and Rekos **[11]** and Ho and Doyle **[12]**. Such methods aim to use physics-based foundations to define scaling laws and engine data to determine unknown factors.

Semi-empirical methods have proven valuable for many OEM applications, but the databases underpinning these methods are narrow in scope with limited geometric variations. Thus, their applicability to revolutionary new combustor architectures as outlined above is questionable at best without significant model enhancements to address emerging technologies. However, ongoing system-level assessments of advanced engine-airframe architectures using acoustic tools such as ANOPP continue to rely on these methods rooted in 1970s era combustor technology.

Objectives and Significance Study

The objective of this research is, in part, to statistically characterize the direct noise field for N and N+3 aero-combustors under realistic operating conditions. This first-ever characterization provides critical understanding of how the dominant source locations, length scales and convective features differ in current and advanced, low-emissions combustors. Specifically,

detailed multi-point statistics of the unsteady heat release and simultaneous pressure fluctuations for N and N+3 combustors have been obtained for improved direct acoustic source description. Also, data analysis of measured power spectra verified scaling principles underpinning current reduced-order models, and modifications to extend and generalize such principles to advanced combustors is proposed.

The database obtained by this research provides critical understanding which should help develop improved semi-empirical models for the short-term that will enable acoustic assessment of advanced aircraft configurations at the preliminary design stage. In addition, the database provides validation data for longer-term efforts to develop higher fidelity methods suited for detailed design. In addition, unsteady temperature measurements were obtained at the combustor exit (input for indirect noise models) to evaluate the capability of advanced, non-intrusive technique at high pressure conditions for the purpose of determining the usefulness in future studies of indirect noise.

Technical Approach

The approach of the proposed research is to statistically characterize the direct noise field for N and N+3 aero-combustors under realistic operating conditions using unsteady heat release (UHR) imaging data, obtained by chemiluminescence, and unsteady surface pressure fluctuations using ITP's (Infinite Tube Probe). A potential non-intrusive and robust combustor exit temperature measurement approach of TDLAS (Tunable Diode Laser Absorption Spectroscopy) for indirect noise modeling was applied to obtain limited unsteady temperature measurement at the combustor exit. The research leveraged hardware developed under NRA N+3 Combustor Technology Contract (NNC14CA30C*)* which developed, designed and tested a N+3, low-emissions, high-OPR compact combustor for a single-aisle advanced concept aircraft.

The base N+3 combustor configuration for this studied (developed under NRA Contract NNC14CA30C) is shown in Fig. 3. The configuration is representative of a single sector of a 14-sector annular combustor. The side-wall inserts provide an approximate annular segment (a true annular segment would have circular-arced OD and ID walls). For the current contract, hardware modifications include side-wall window insert for imaging the UHR and upper and lower walls to provide the dilution jets of the N (RQL) combustor (see Fig. 4). The design of the N configuration walls (specifically the dilution jets) is described in Appendix B. In addition, an instrumentation flange and TDLAS probes (i.e., Laser beam transmitter and receiver tubes) were designed and fabricated for the current contract. Figure 5 summarizes the hardware that has been designed and fabricated for the combustion noise testing.

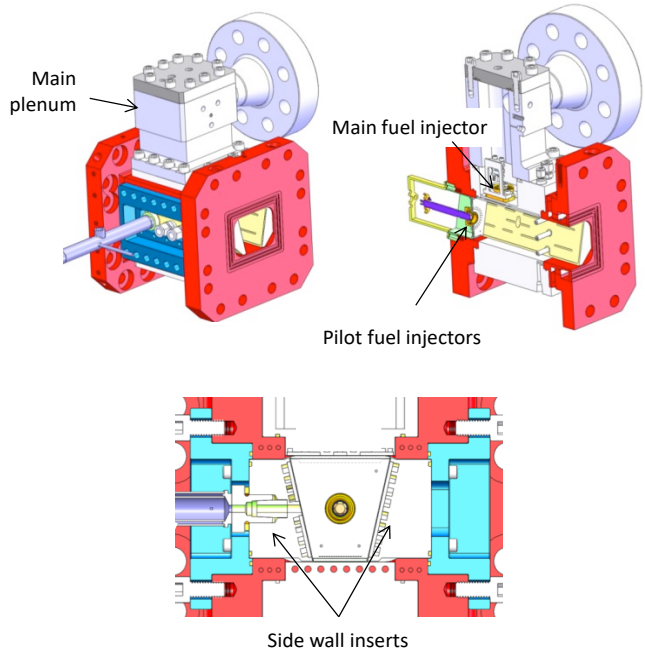

Figure 3: Base N+3 combustor configuration developed under NRA Contract #*NNC14CA30C*

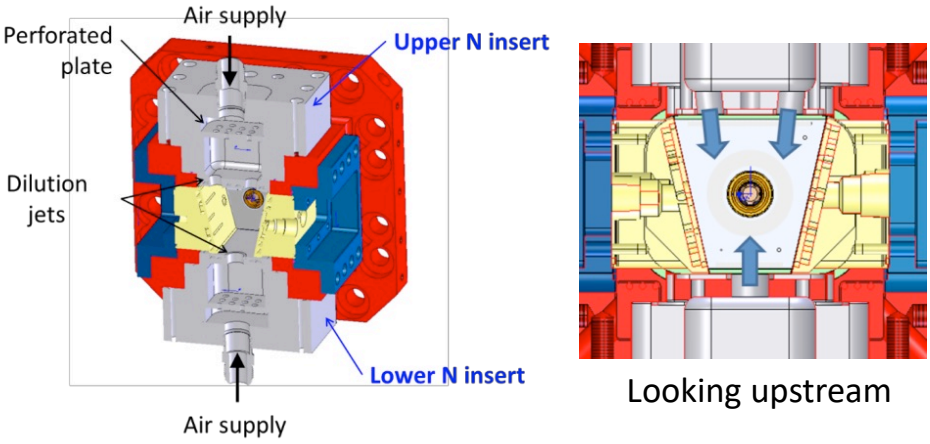

Figure 4. N combustor configuration

- Visualization window

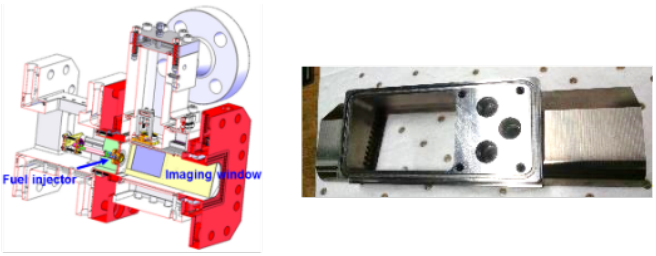

- N combustor inserts

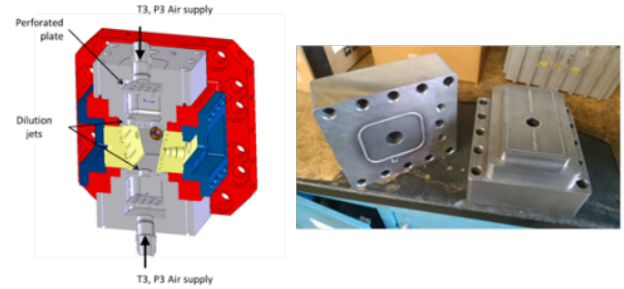

- Instrumentation flange

- TDLAS probes

Figure 5. Fabricated hardware for combustion noise test

Test Matrix Definition

N+3 Test Matrix

Details of the operating points for the N+3 combustor as defined by the NRA Combustor Technology Contract (NNC14CA30C) are given in Table A1 and plotted qualitatively in Fig. 6 in terms of P_3 and T_3. The operating conditions selected for the combustor noise investigation are approach, climb, and sea-level take-off (SLTO) which have the biggest impact on community noise (max take off (MTO) condition, as noted in Table A1, is outside the range of the test rig). In addition, at each nominal operating point, sweeps of fuel-to-air (FAR), flow parameter ($FB_b = \dot{m}_b\sqrt{T_3}/P_3$), P_3, and T_3 were varied independently while holding all other combustor conditions approximately constant. This range of operating points and associated parameter sweeps enabled an assessment of how legacy combustor noise scaling laws capture the measured acoustic pressure variation.

N Test Matrix

For the N combustor the operating conditions are also plotted in Fig. 6. The PW6000 (single-aisle jet liner) engine cycle has been selected as the representative cycle of the N configuration. Like the N+3 configuration, data will be obtained at approach, climb, and SLTO. In addition, in order to provide a relative comparison of the combustion noise for the N and N+3 configurations at the same P_3 and T_3, the operating conditions of the N combustor will be extended to higher OPR and the operating conditions of the N+3 combustor will be extended to lower OPR to provide a back-to-back comparison. This operating point is notionally shown in Fig. 6 ("New N-N+3 comparison point" or so-called "matched" operating point) for approach. Similar points were defined for climb and SLTO.

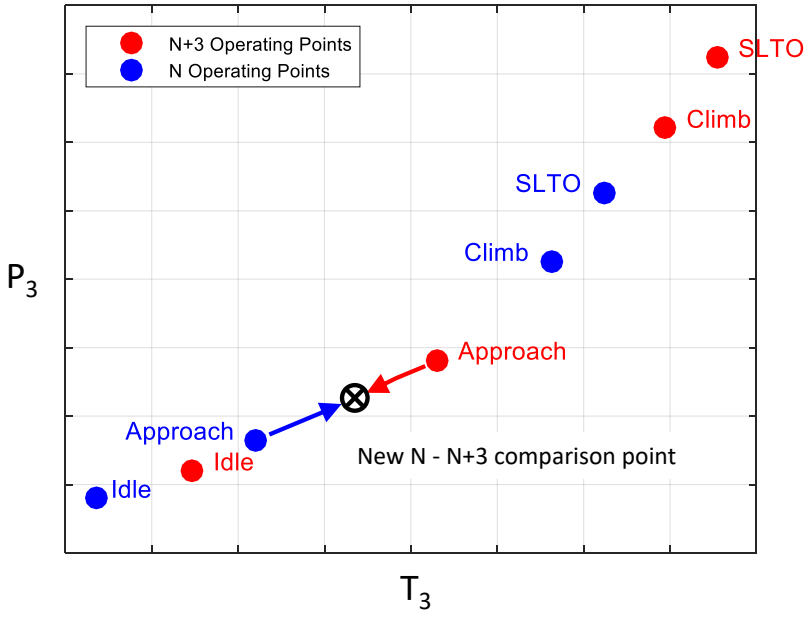

Figure 6. N and N+3 operating conditions

Combustion Test Sections and VRASC Test Rig

Figure 7 shows the two test sections developed for the combustion noise test. The N+3 combustor configuration developed under the NRA N+3 Combustor Technology Contract (NNC14CA30C) was modified with a relatively large chemiluminescence imaging window. For the N configuration, the top and bottom walls of the N+3 configuration were replaced with dilution jet inserts (design described Appendix B).

Both combustor configurations were installed in the VRASC (Variable Resonance Acoustic Screening Capability) test rig which is shown in Fig. 8. There are separate heated air streams that feed the centerline (the pilot for the N+3 configuration) and the side branches (the mains for the N+3 configuration and the dilution jets for the N configuration). Downstream of the combustor section is a side branch pipe of variable length ("VRASC tube") that is control by a movable plunger. The maximum length of the plunger stroke is about 54 inches. The purpose of this arrangement is to enable varying the longitudinal acoustic modes in the combustion section to evaluate sensitivity of fuel/air mixers to thermo-acoustic instability at different frequencies (i.e., map out the frequency response of the heat release transfer function). For the current investigation, the stroke of the VRASC plunger was fixed at a location that minimizes in-band acoustic modes so that the broadband, direct noise field can be studied. Downstream of the VRASC tube is a variable-area choke to provide a realistic boundary condition, typical of an aero-combustor.

Figure 9 shows the basic locations of the dynamic pressure instrumentation. The dynamic pressure measurements are all made with ITP (Infinite Tube Pressure) probes that are calibrated at atmospheric conditions and data-matched to a frequency-based acoustic model for post-test corrections. Locations include the pilot and main plenums (P5 and P6, respectively), pilot bulkhead (P7), aft-test section (P8), and VRASC flange (P9). Other locations include the end of the VRASC tube and plunger face.

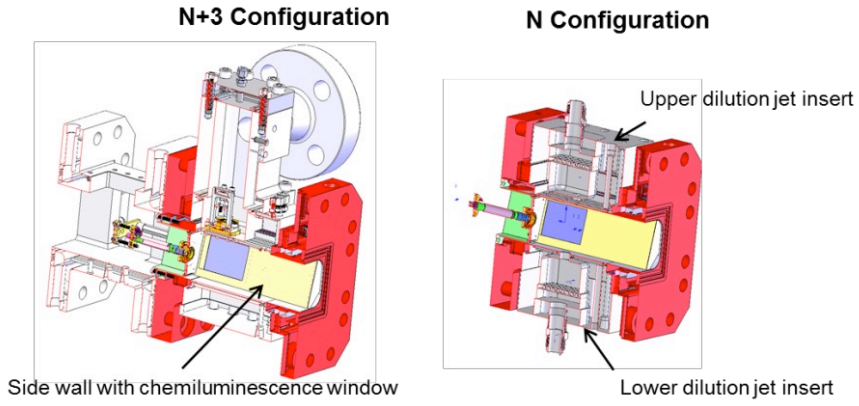

Figure 7. Test combustor configurations for current investigation

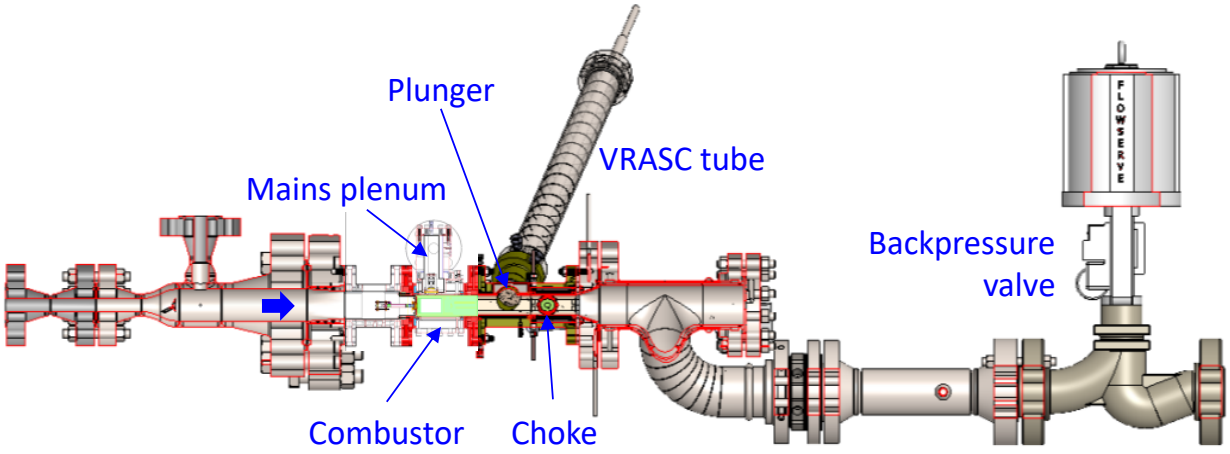

Figure 8. VRASC test rig with N+3 combustor test section

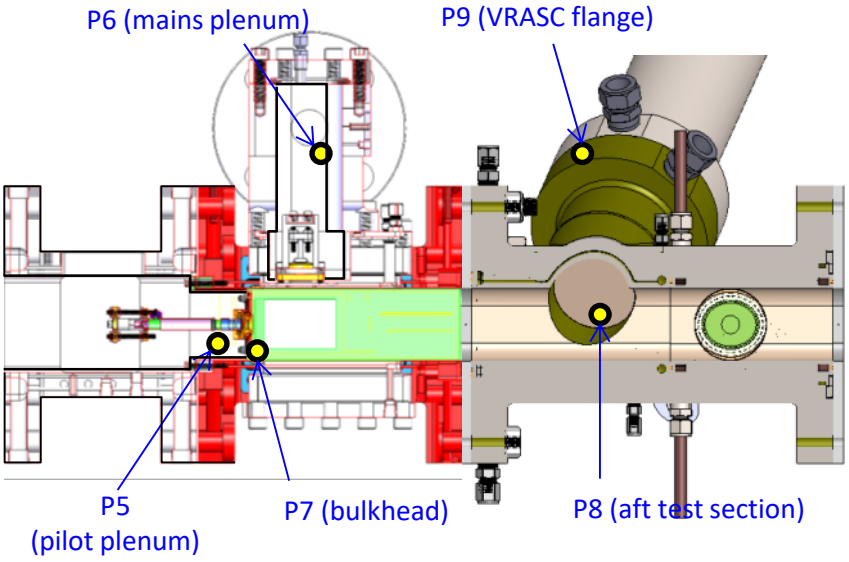

Figure 9. Dynamic pressure instrumentation

Pilot Fuel Atomizer Selection

Figure 10 shows the combustion dynamic response for three of the four pilot fuel atomizer evaluated under the NRA Combustor Technology Contract (NNC14CA30C). The horizontal axes are plunger stroke and frequency. The vertical axis is dynamic pressure amplitude. The colors (blue=low, red=high) are auto-scaled, however the physical height of the vertical axes is consistent between maps. Examining the cruise maps for the high-shear atomizer shows an

elevation in pressure along the longitudinal modes and harmonic (~6) that sweep from high frequency to low frequency as the plunger moves from shorter to longer stroke (see light blue "ridge" lines). For this condition and atomizer, the pressure response to the modes is approximately frequency independent. However, the same atomizer at approach conditions, there is a strong response at a preferred frequency. Given these atomizer dynamic responses for the limited conditions of cruise and approach, the air-blast atomizer (shown in sectional view in the figure) was selected for the combustion noise tests of the current contract due to is apparent reduced propensity to thermo-acoustic instability.

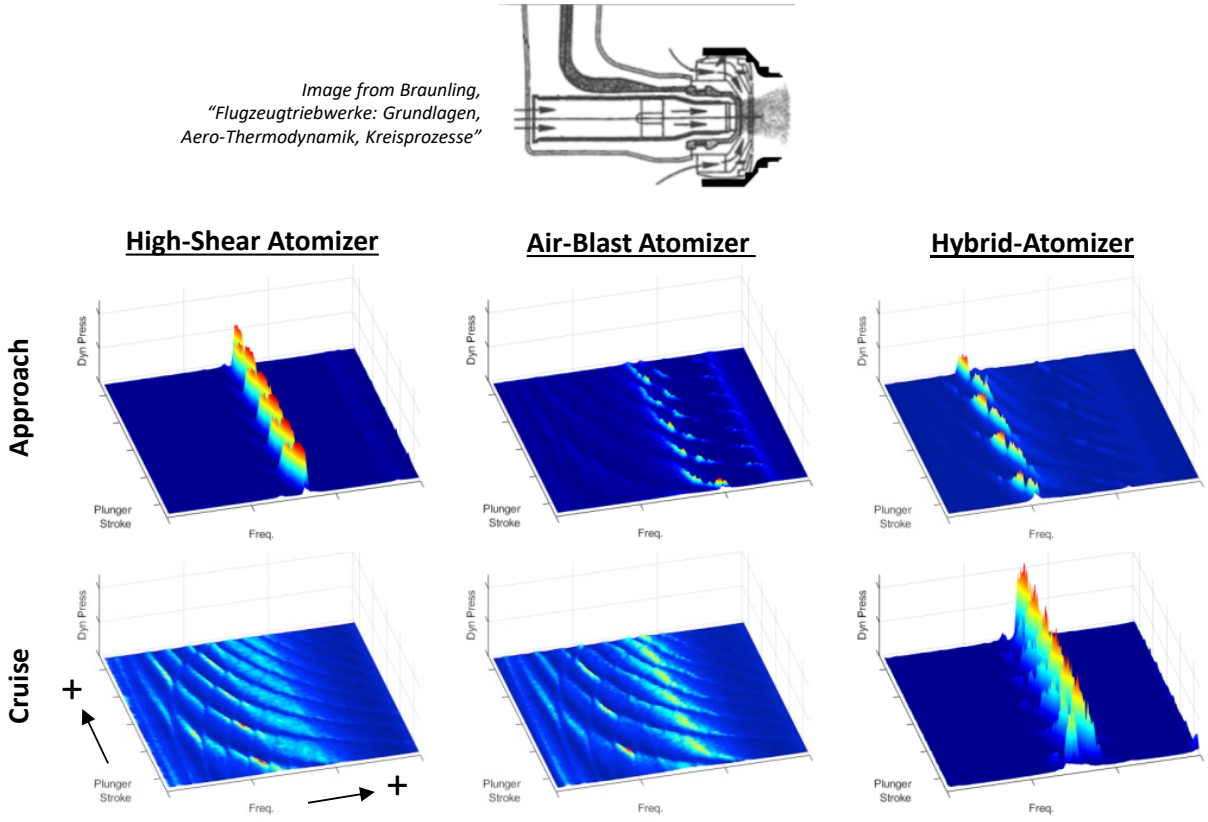

Figure 10. Combustion dynamics for each atomizer type

Chemiluminescence Imaging Window Performance

Chemiluminescence imaging was used to capture the unsteady heat release (UHR) field and so the performance of the imaging window is critical for the success of the project. The window that was designed and fabricated for the chemiluminescence testing was used by the NRA N+3 Combustor Technology Contract (NNC14CA30C) to image the combustion dynamics using visible and CH-filtered light. This testing provided an opportunity to access the window performance as well as obtain preliminary UHR field data and chemiluminescence species identification.

Figure 11 shows the design of the window including the wall cooling (water) and window cooling (air). Figure 12 shows photographs of the window during installation and Fig. 13 shows example instantaneous CH-filtered images for an idle condition (pilot only) and cruise condition (pilot and mains). The locations of the pilot and main injectors are illustrated in the images. The images appear to provide good resolution of the larger turbulent structure. However, despite an aggressive design to maximize window size, clearly significant portions of the UHR field are not captured. To overcome this limitation, oblique view angles were used to improve the captured field during the combustion noise testing.

During the N+3 Combustor Technology Contract testing, the imaging window was successfully used for six test cycles (heat up, testing, cool down), each cycle lasting about 6 hours up to pressures of 200 psia without leaking. Figure 14 shows photographs of the window after this testing. Three areas of distress are apparent. First is the melted metal damage to the slot injection lip which occurred during the first heat up cycle due to an error of not increasing the window cooling air pressure with rig pressure, thereby starving the lip of cooling air. Second and third areas of distress are the cracking of the inner window and fouling with residual combustion products and/or coking of fuel during start up and shutdown. Despite these failure (which were subsequently repaired), the window continued to perform and provide good images.

To improve the imaging area of the combustion zone for the combustion noise testing, the high-speed video camera was mounted on an x-y traverse slides and a pan-tilt head with a remote focusing actuator (shown in Fig. 15). With this arrangement, the camera viewing angle was optimized during combustion to maximize the combustion zone viewing. To account for the oblique viewing angle, a reference grid was installed in the test section post testing. The reference grid images provided a means to relate pixel location to rig coordinate location using a linear fit (e.g., x=linear f(vertical pixel, horizontal pixel)).

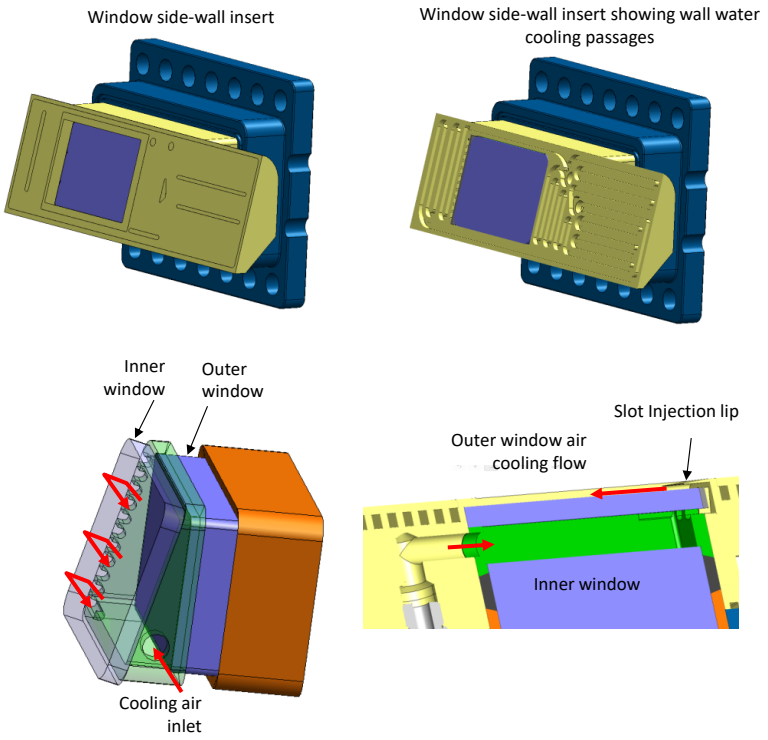

Figure 11. Combustion imaging window cooling design

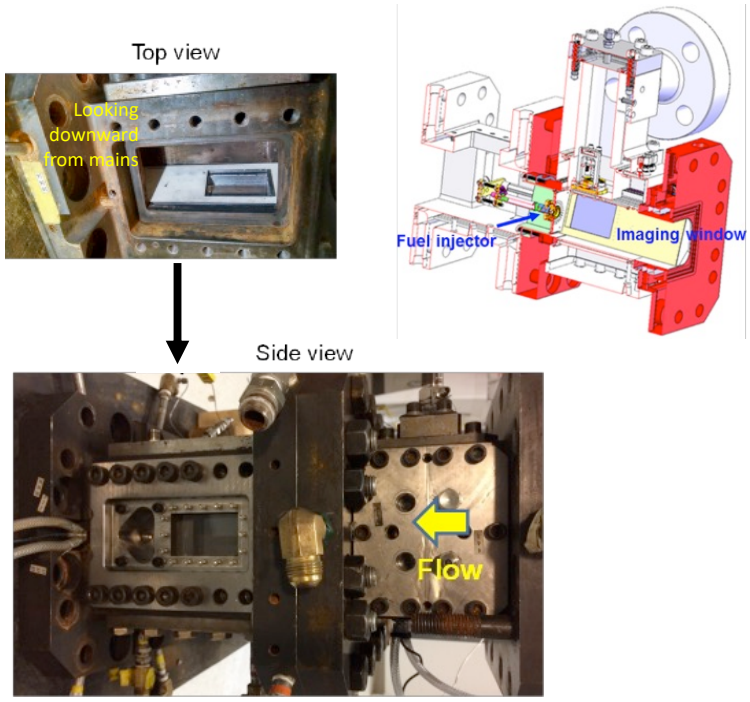

Figure 12. Combustion imaging window installation

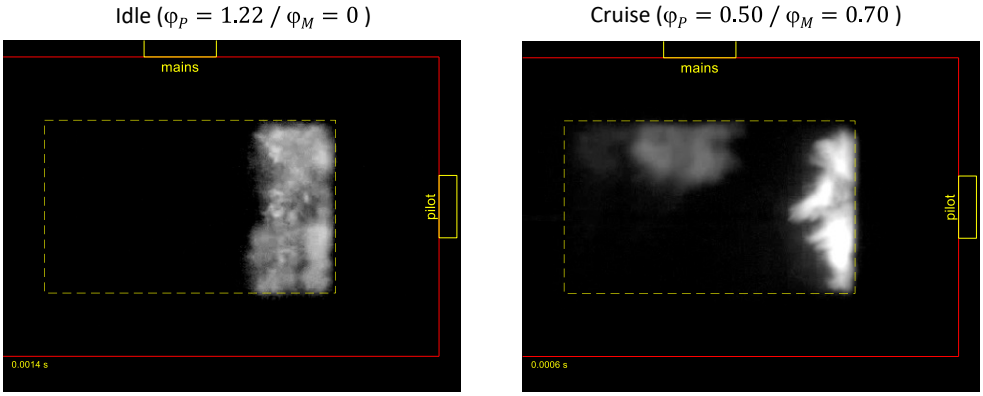

Figure 13. Example CH-filter images

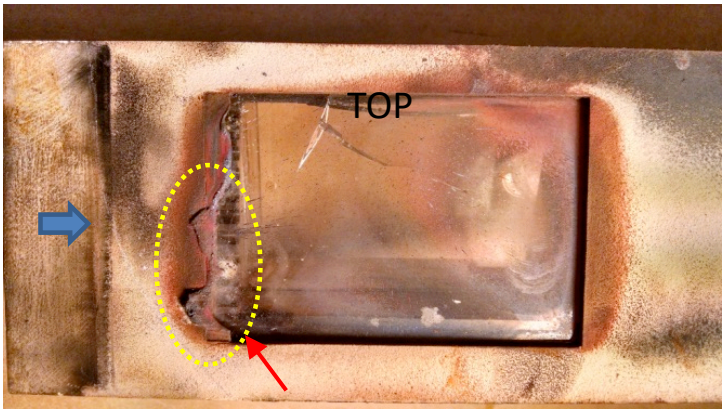

Damage to slot injection lip early on due to lack of cooling air flow while increasing rig pressure (repaired)

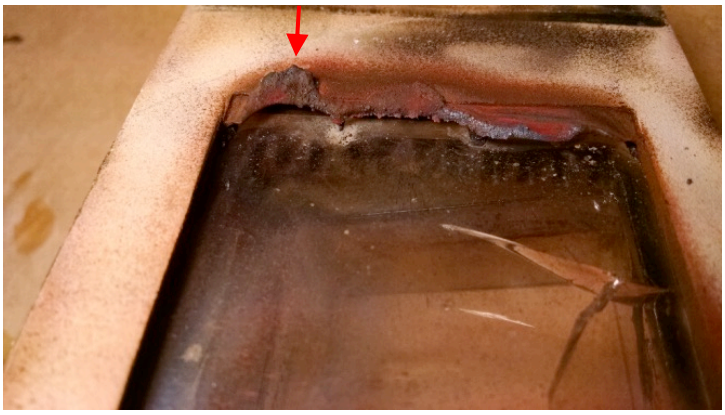

Figure 14. Imaging window after testing

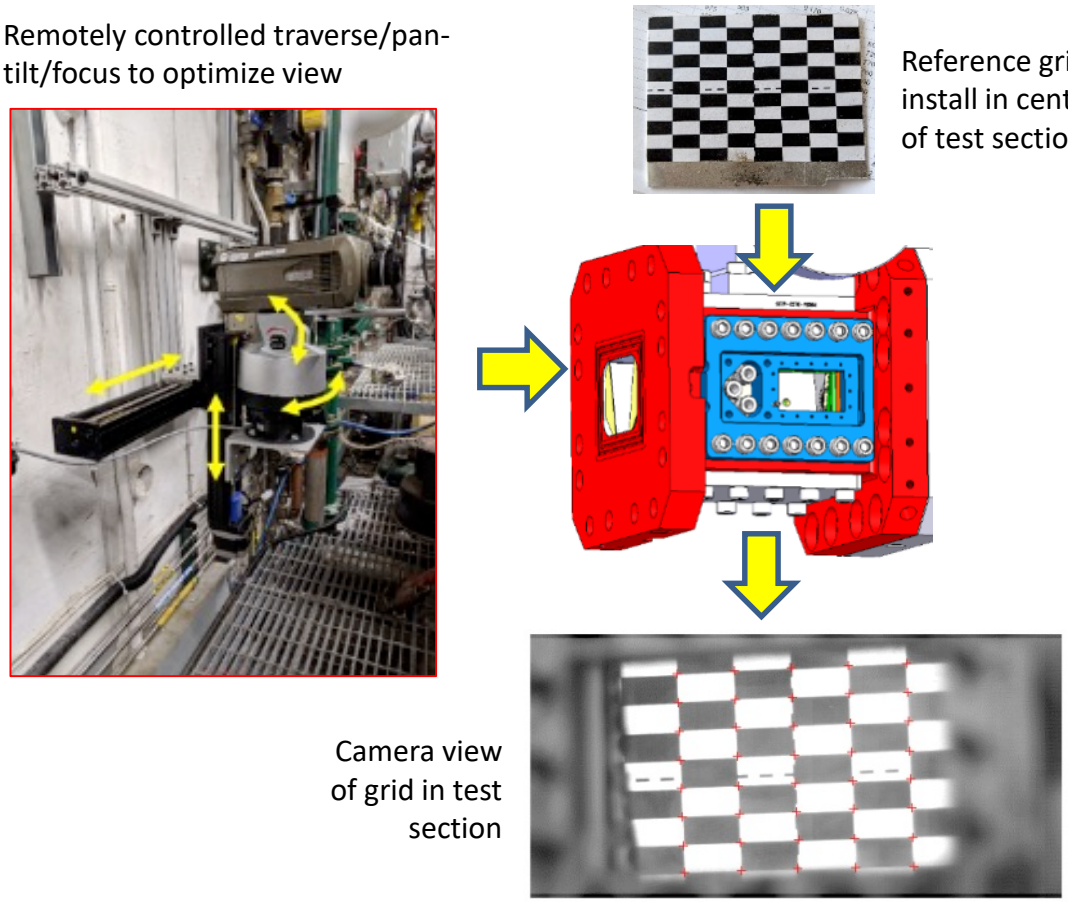

Figure 15. Reference grid for imaging processing

FEA Model Validation

As discussed later, an accurate FEA model of the combustor section and test rig piping is needed to provide the numerical basis functions for the acoustic direct noise computation. In addition, it was found this accurate FEA model is useful for normalizing the measured dynamic pressure to better isolate the broadband noise. This section describes the FEA model validation.

Figure 16 shows the domain of the FEA model for the VRASC test rig and combustion section. A similar model was described in FY2017 annual report **[13]** that was for the unchoked combustor exit condition and without the VRASC tube. As described in the FY2017 annual report, the injector impedance models were validated with a flowing impedance tube test as illustrated briefly in the figure. The domain temperatures for the FEA model are shown in the figure as T_3 (supply temperature), T_{4F} (combustor front end temperature), and $T4$ (combustor temperature after mains). The combustor temperatures were computed based on the known fuel-to-air ratio assuming complete combustion and adiabatic wall conditions. Due to significant wall water-cooling in the stagnated air of the VRASC tube, the adiabatic assumption was found not to be a good approximation. Instead the temperatures in front of and behind the plunger were determined by tuning temperature to match observed modes in the VRASC tube.

Figure 17 shows this temperature tuning process. Plotted in the bottom left is a surface map of the magnitude of the P8/P7 pressure ratio (aft test section/bulkhead) versus frequency and plunger stroke position (the pressure locations and plunger are schematically shown above the surface plot). The dominate peaks and valleys of the surface map are associated with the longitudinal modes between the bulkhead and plunger face which decrease in frequency with increasing plunger stroke. On close inspection, there are "wrinkles" in these modes that increase in frequency with increasing plunger stroke. These wrinkles are due to longitudinal modes behind the plunger. Together with the known length of the tube behind the piston (L_B), the average temperature behind the piston can therefore be found by fitting the even longitudinal mode frequencies (rigid-rigid boundary conditions) to the wrinkles in the surface plot of P8/P7. As can be seen in the plot, a temperature of 180 F (82 C) is a good approximation for all stroke positions for these data sets.

A similar process is performed for the portion of the VRASC tube on the front side of the plunger. Here the pressure ratio P10/P9 (plunger face/VRASC flange) is used for the temperature tuning which is shown in the bottom right of Fig.17 (note, the P10 signal is greatly attenuated by a 10-foot-long feed line to the ITP which results in a noisy pressure ratio). It was discovered that unlike the VRASC tube behind the plunger, a constant temperature was found to be insufficient. By discretizing the tube in front of the plunger into five elements, assuming an initial temperature in the first element, and a logarithmic temperature drop/distance, a reasonable accurate fitting to the measured modes could be found as illustrated in the figure. To efficiently tune these temperature parameters, a surrogate five-element transmission matrix model was built and the modes were found by peak searching of the P10/P9 pressure ratio.

Figure 18 shows a qualitative comparison of the P8/P7 pressure ratio of data versus model at the top of the figure with a visualization of modes associated with the map's features. The bottom

gives a quantitative comparison of several pressure ratios for five plunger locations from 6 to 54 inches which shows reasonable agreement for all plunger locations and dynamic pressure ratios.

Acoustic Transfer Function

One of the key outputs of the FEA Model is the acoustic transfer function that relates the dynamic pressure response to the UHR. Figure 19 shows how this transfer function is typical thought of as the forward leg of a thermo-acoustic feedback loop (see block "A", **[14]**). From the forced-response FEA model (see upper left image in Fig. 20), the acoustic transfer function can be estimated using the volume velocity (V_S) of the spherical forcing to represent the flame UHR (q) and the bulkhead dynamic pressure (P_B), hence

$$A = \frac{p_B}{q} \approx \frac{p_B(\gamma_4 - 1)}{\rho_4 c_4^4 V_S} \sim \frac{p_B}{V_S} \tag{1}$$

where the volume velocity has been related to the approximation $q = \rho_4 c_4^2 V_S/(\gamma_4 - 1)$ **[15]**.

The image in the top right of Fig. 20 shows a typical acoustic transfer function for a range of plunger stroke locations. The "ridge" lines that sweep from high to low frequency with increasing plunger stroke correspond to the half-wavelength longitudinal mode (and even harmonics) from the bulkhead to the plunger face (as illustrated in the bottom left image). These are the so-called "VRASC" modes. The "kinks" or discontinuities in the VRASC modes correspond to intersection of longitudinal modes that exist behind the plunger in the VRASC tube. The peaks (colored yellow/orange) occur were the VRASC mode aligns with the half-wavelength mode of the bulkhead-to-choke (as illustrated in the bottom right image). Depending on the operating conditions, this frequency is between 750-850 Hz. Also present is 90-100 Hz mode that is nearly independent of stroke location. This corresponds to a full-wavelength mode from the bulkhead to the end of the VRASC tube. Though not visible with this linear pressure map, significant harmonics of this mode are measurably present and influence the pressure spectra as discussed in the next section.

It should be pointed out that since the plunger was fixed for the entire study at a four-inch stroke location, only the edge of the acoustic transfer function map closest to the reader is relevant to the data obtained for this investigation.

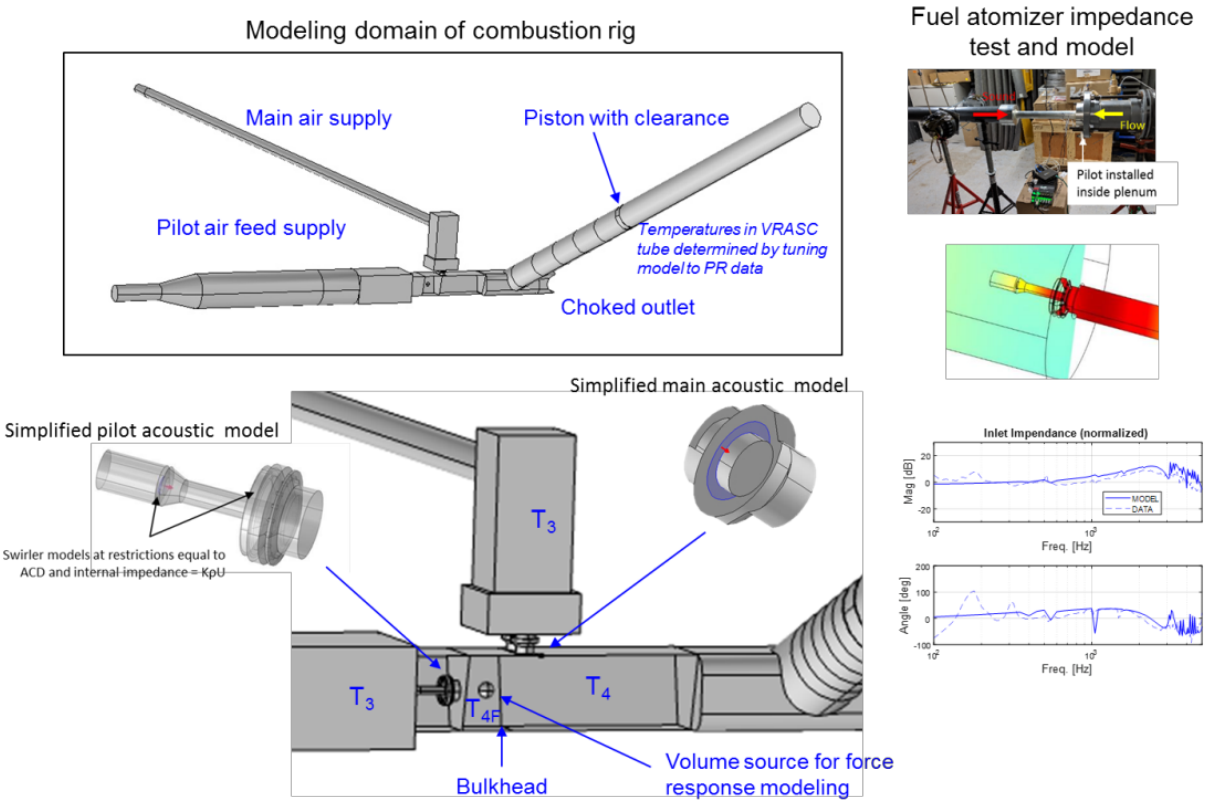

Figure 16. FEA model elements

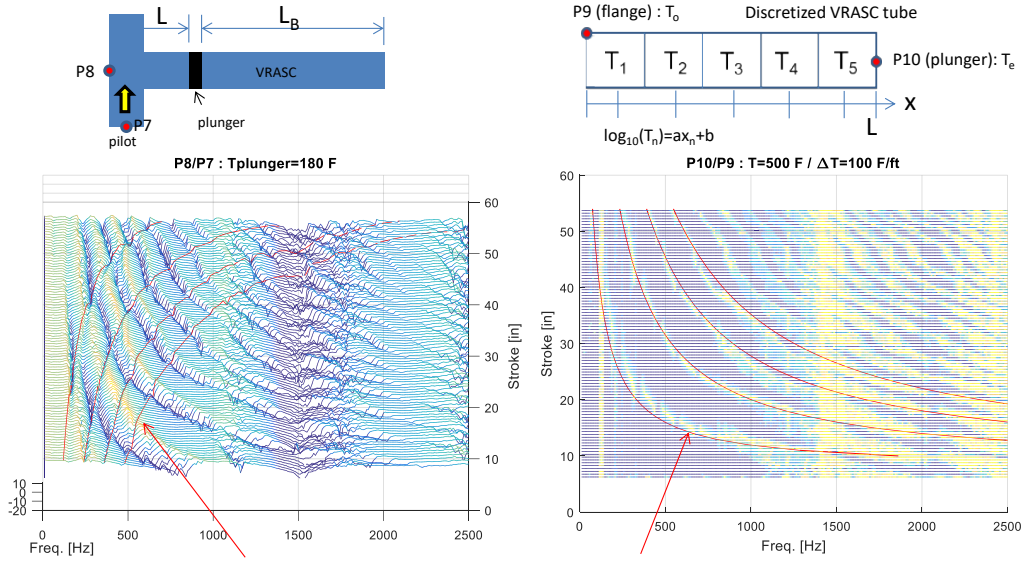

Long modes behind are slightly visible in P8/P7 response. Manually varied $T_{plunger}$ (constant throughout back side) to match modes.

Used a 5-element transmission matrix model of a duct with variable temperature. Manually varied T_o and $\Delta T/ft$ to match measured P10/P9.

Figure 17. Temperature tuning for FEA model

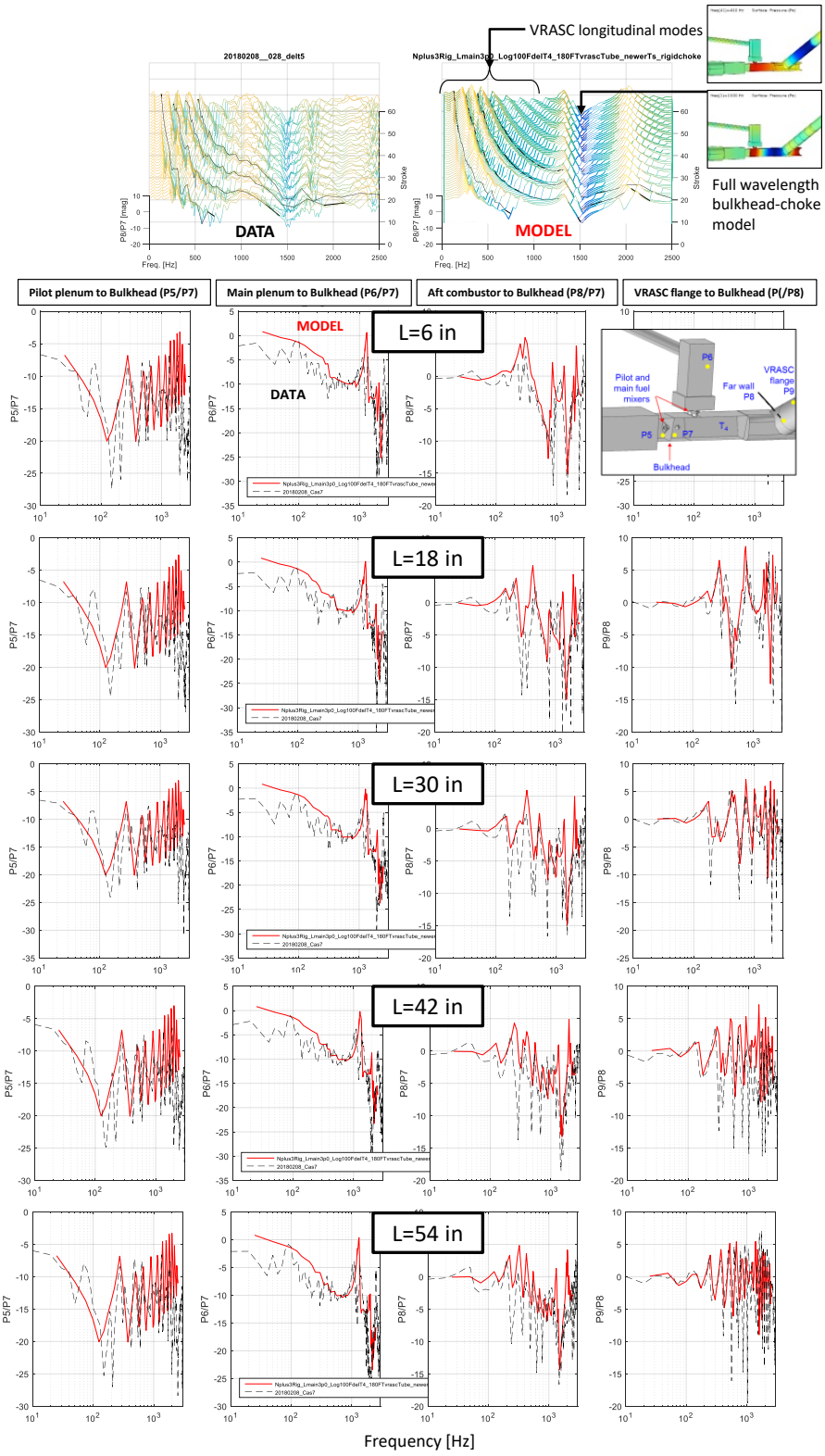

Figure 18. FEA model validation

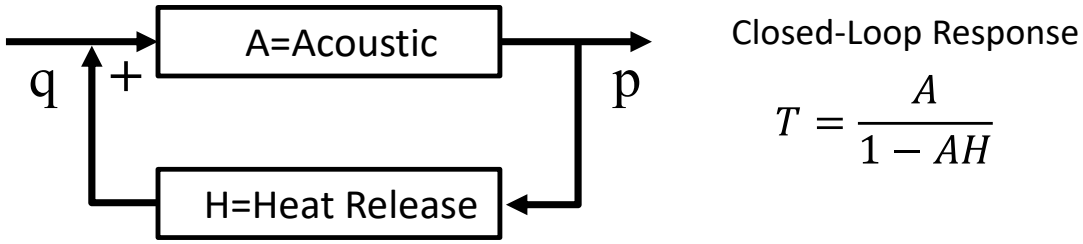

Figure 19. Typical thermo-acoustic feedback loop

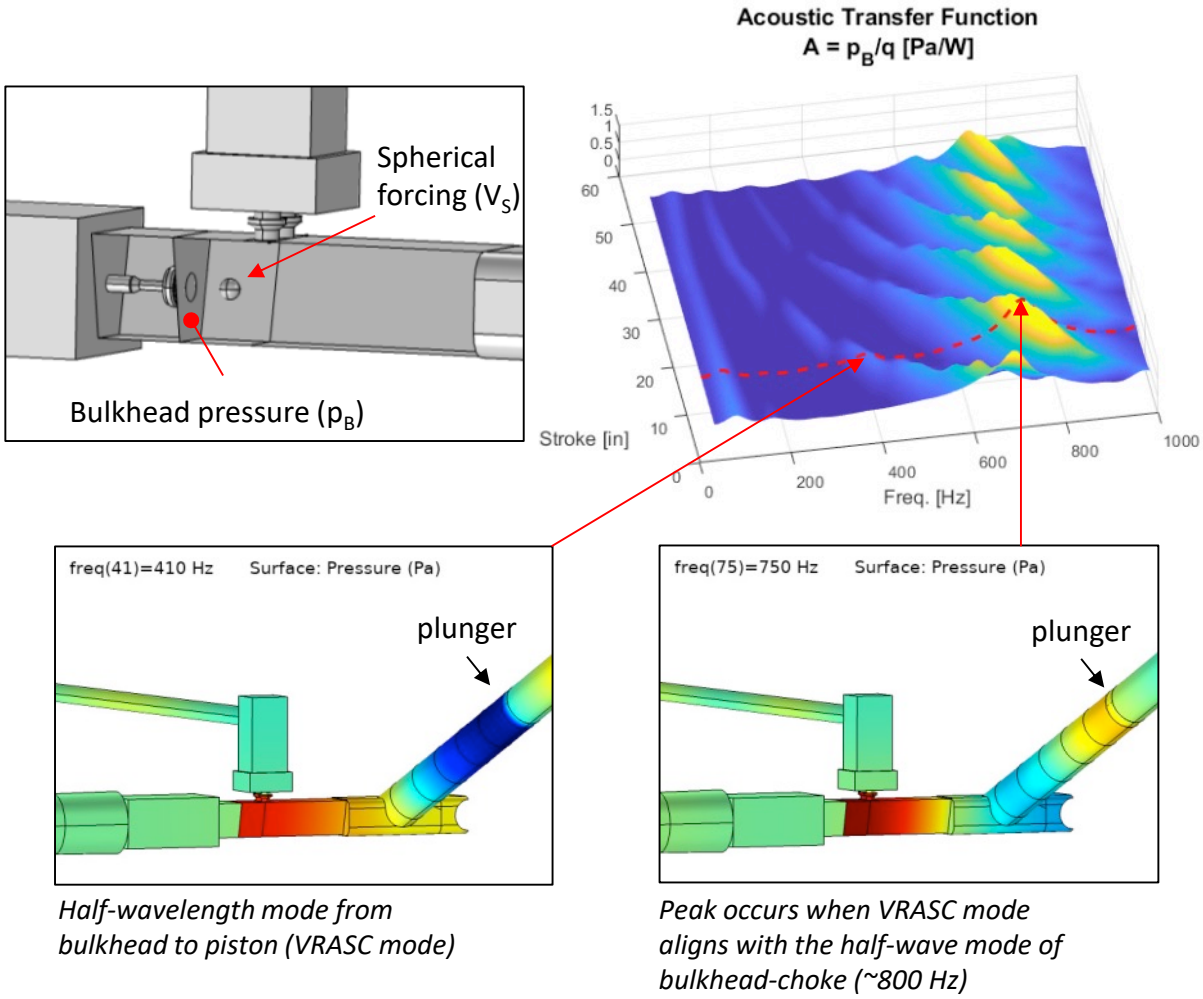

Half-wavelength mode from bulkhead to piston (VRASC mode)

Peak occurs when VRASC mode aligns with the half-wave mode of bulkhead-choke (~800 Hz)

Figure 20. Acoustic transfer function from FEA model

Dynamic Pressure Scaling Analysis

In this section the dynamic pressure spectra and OASPL trending are compared with legacy scaling laws **[11, 12]**. Due to the significant presence of longitudinal modes in the frequency band of the broadband combustion noise (100-600 Hz), different spectrum normalizations (but not dimensionless) are considered to minimize the effect of these modes on the pressure spectra and OASPL level. Primary to all the normalizations considered here is the acoustic transfer function, $A = p_B/q \sim p_B/V_S$, from the data-matched FEA model (discussed in the preceding section) for each operating point.

Dynamic Pressure Normalizations

Figure 21 illustrates one of the considered normalizations. The plot on the left is the so-called "Normalization Function" (NF), which is a non-dimensional acoustic transfer function wherein the acoustic transfer function is normalized by the average magnitude over the 10-500 Hz range (see equation in plot). The plot on the right side shows the raw narrow-band data (black line) and the same data scaled by NF (red line). Though not perfect, the normalization significantly reduces the modal content yielding a spectrum which much more akin to the expected spectrum shape of broadband combustion noise than the raw data. The circular symbols in the plot are the corresponding third octave band spectra. The normalized third octave band peak in general occurs at the 315 Hz band.

This normalization assumes there is no or minimal feedback coupling via the heat release transfer function (Fig. 19). During the course of testing, any observed thermo-acoustic coupling or instability occurred at ~800 Hz where the acoustic transfer function magnitude is highest (see previous section's discussion of Fig. 20). For this reason, in addition to normalizing the spectra, the OASPL was summed over the limited frequency band of 50-500 Hz to highlight the contributions due to broadband combustion noise. It should be pointed out that indirect noise that is radiating upstream from the choke region is not capture by this normalizing approach which, no doubt, contributes to its less than perfect scaling function.

In total, four pressure normalizations were considered. The first normalization is,

$$p_{nA} = p/NF \quad \text{[Pa]}$$

which is described above (note, for simplicity, the "B" subscript for the burner or bulkhead pressure has dropped). The second normalization is,

$$p_{nB} = P\left|\frac{q}{p}\right| = P\left|\frac{V_S}{p}\right|\frac{\rho_4 c_4^2}{\gamma_4 - 1} \quad \text{[W]}$$

which uses the acoustic transfer function form with heat release in the dominator (Eqn. 1). The dimensionally of this normalization is less than satisfactory which is attempted to be rectified by the third and fourth normalizations. The third normalization is,

$$p_{nC} = P\left|\frac{q}{p}\right|\frac{P_4}{Q_f} = p\left|\frac{V_S}{p}\right|\frac{\rho_{f4} c_{f4}^2}{\gamma_4 - 1}\frac{P_4}{Q_f} \quad \text{[Pa]}$$

which is similar to p_{nB} except that the front-end mean heat release rate (Q_f), front-end temperature (T_{f4}), and the mean pressure (P_4) are used to make it dimensional correct. The final normalization is,

$$p_{nD} \left|\frac{q}{p}\right| \frac{P_4}{Q} == p \left|\frac{V_S}{p}\right| \frac{\rho_4 c_4^2}{\gamma_4 - 1} \frac{P_4}{Q} \quad \text{[Pa]}$$

which is the similar to p_{nC} except that the total heat release rate (Q), exit temperature (T_4), and the mean pressure (P_4) are used to make it dimensional correct.

ANOPP and Matthews-Rekos Scaling

Two legacy scaling laws, ANOPP and Matthews-Rekos, were assess with the dynamic pressure data from the current study, specifically, the bulkhead pressure data. For ANOPP, the original formulation (GE/SAE model) was applied (using sea-level reference conditions, since the ambient conditions are not relevant for a test rig).

The predicted ANOPP radiated OAPWL applied to OASPL (at the bulkhead) without turbine/nozzle attenuation can be written as

$$OASPL = 10 \log_{10} \left[c_o^2 \dot{m}_b \left(\frac{T_4 - T_3}{T_3}\right)^4 \left(\frac{P_3}{P_o}\right)^2 \right] + K \tag{2}$$

where $c_o = 340.3\ m/s$, $P_o = 101.325\ kPa$, $\dot{m}_b$ is the burner mass flow rate and K is a data-matched constant.

The predicted Matthews-Rekos (M-R) radiate OAPWL applied to OASPL without turbine/nozzle attenuation and one fuel nozzle can be written as

$$OASPL = 10 \log_{10} \left[A_b^2 P_3^2 \left(1 + \frac{H \cdot FAR_{st}}{c_p T_3}\right)^2 \left(\frac{FP_b}{A_b^2}\right)^4 FAR^2 \right] + K \tag{3}$$

where $A_b$is the combustor cross-sectional area, FAR_{st} is the stoichiometric fuel-to-air ratio, H is the fuel heating value, $FP_b$is the flow parameter ($= \dot{m}_b \sqrt{T_3}/P_3$), and K is a data-matched constant.

In terms of the predicted spectra, comparisons were made with the spectrum given **[12]** for ANOPP and **[11]** for Matthews-Rekos. Both predictions are applied here in terms of ΔdB from the SPL at the peak frequency. Though the former prediction assumes 400 Hz as the peak frequency and the latter a formulation based on reaction length and operating conditions, the current data typically had a peak SPL (when normalized as described earlier in this section) at the 315 Hz third octave band, so this value was used in the following figures for the current data.

The left two plots in Fig. 22 shows the raw (bulkhead) pressure data in terms of OASPL versus the ANOPP and M-R scaling described above. The operating condition (approach, climb, and SLTO) and combustor configuration (N and N+3) are noted in the legend. Note the displayed data corresponds to the entire data set of parameter sweeps of *FAR*, FP_b, P_3, and T_3. The solid

lines correspond to the predicted OASPL (Eqns. 2 and 3) with the K values (derived from an "eye-ball" best fit) listed in the plot title. The dashed lines correspond to ±3 dB bands. The plot on the right side of the figure shows the corresponding raw third octave spectra relative to the SPL at 315 Hz.

The primary take away from this figure is without normalizing the measured pressure to remove the strong influence of the longitudinal modes, the data bears little resemblance to the legacy scaling laws, particularly with the third octave spectra.

Figures 23a-d show the same plots for the four different pressure normalizations described above. Clearly the normalization greatly improves the agreement with the predicted spectra and reduces the scatter in the OASPL plots. The p_{nB} normalization appears to be the best at reducing the scatter and shows for most of the operating points, the legacy scaling law provide a good predictor of the noise.

In the subsequent Figures 24-26, this pressure normalization (p_{nB}) is replotted for the individual parameter sweeps to provide clarity of deviations from legacy scaling and insight as to why. These figures repeat the trio of plots in Fig. 22 but add two additional non-scaled plots of OASPL versus the swept parameter and spectra in terms of SPL versus frequency in Hertz.

Approach

Figures 24a, b, c and d show the approach condition results for the *FAR*, FP_b, P_3, and T_3 parameter sweeps respectively. Both the N (red symbols) and N+3 (blue symbols) configurations are plotted. The legend identifies the excursion value with symbol type (e.g., circle, square, etc.). Also, the number in parenthesis identifies the point number of the test. Referring to the corresponding appendix Tables A3 and A4 (sorted by configuration and operating condition), the exact operating conditions can be identified.

The approach data, for both the N and N+3 configuration, nominally follow the legacy scaling laws and spectrum shapes reasonably well (with the exception of where thermo-acoustic instability can occur between 800-2000 Hz, or 3 to 6 octave bands above the peak amplitude frequency band, f_{pk}).

Climb

Figures 25a, b, c, and d show the climb conditions results for the parameter sweeps and both combustor configurations. For this operating condition, the N configuration follows the legacy scaling laws and spectrum shapes. For the N+3 FP_b and P_3 parameter sweeps (Figs. 25b and c, respectively), the OASPL follow the legacy scaling laws (particularly well for the ANOPP scaling), however, there is moderate deviation from the spectrum shapes at lower frequencies. For the N+3 *FAR* parameter sweep (Fig. 25a) the OASPL shows a moderate trending of decreasing with increase *FAR*, opposite of the legacy scaling and N configuration trending. There is also a noticeable movement in the spectrum shapes toward the legacy shape with increasing *FAR*. For the N+3 T_3 parameter sweep, an OASPL trending opposite the legacy scaling laws is observed, specifically for the M-R scaling. For the lower T_3 values, the spectra shape deviates significantly from the legacy spectrum shapes at lower frequencies.

The N+3 deviation noted above from legacy scaling laws are believed to be due to the relatively weaker flame anchoring of the main combustion flame (RJIC, Reacting Jet In Cross-flow) compared with the RZSF (recirculating Zone Stabilized Flame). This weaker anchoring of the RJIC is likely more prone to low-frequency oscillation, whereas, increasing T_3 and *FAR* would likely tend to stabilize.

Sea Level Takeoff (SLTO)

Figures 26a, b, c, and d show the SLTO conditions results for the parameter sweeps and both combustor configurations. For the N configuration, again the legacy laws (OASPL trending and spectrum shape) provide good predictions. For the N+3 configuration, with the exception of the *FAR* sweep, the same is true (with some deviation in T_3 spectra, Fig. 26d). For the *FAR* sweep (Fig. 26a), the trending is markedly different than the legacy scaling law for OASPL. Like for the climb condition, the OASPL decreases with increasing *FAR*, though the spectral shapes better match the legacy spectrum shapes than those for the climb condition.

Unlike the climb condition, the spectra shapes are better predicted by the legacy spectrum shapes (with some exception for the T_3 sweep). Apparently the increased T_4 for SLTO (see Table A3) helps minimize the low frequency oscillations that were observed for climb. Like the climb condition, the OASPL decreases with increase *FAR*, however, to a greater extent. Examining the raw spectra (Fig. 26a, upper right), there is a very noticeable, broadband reduction in SPL with increasing *FAR*. This suggests, that under certain conditions, the axially staged RZSF pilot and RJIC main can offer a path to possible noise reduction over traditional RQL combustors.

Matched Operating Points

As discussed in the test matrix section of this report, for each operating condition (approach, climb, and SLTO), new N-N+3 comparison points or "matched" points were established where the P_3, T_3 were increased (while maintaining other combustion parameters) for the N configuration and decreased for the N+3 configuration to provide a back-to-back comparison of the two combustors at the same P_3, T_3 (see Fig. 6). Figure 27 shows the results for these three sets of comparisons.

First, it should be pointed out that setting the desired operating points were not always successful due to limitation in maintaining a choked flow exit (choke area control limitations). This limitation can be seen in the top middle plot which plots OASPL versus P_3. Ideally, the N and N+3 corresponding conditions would have the same P_3. This condition is true for the approach, however, no so much for climb and SLTO.

With the above caveat, the following observations are made. The N+3 configuration is a 3-7 dB higher than the N configuration. The low frequency spectra for the climb and SLTO are significantly higher for the N+3 configuration. This result in not directly consistent with the parameter sweep results above, particularly for SLTO where the spectra was consistent with legacy spectrum shapes. This difference is explained by the above-noted N+3 configuration's sensitivity to T_3 which is significantly lower than the cycle point design for the matched data point. Hence, the matched operating point comparison may not be very relevant.

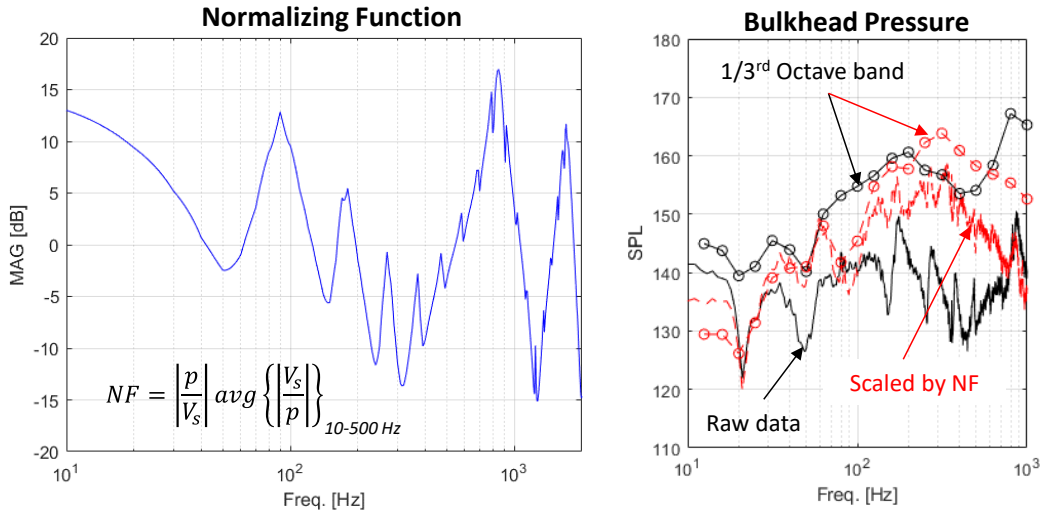

Figure 21. Spectrum normalization to minimize influence of longitudinal modes

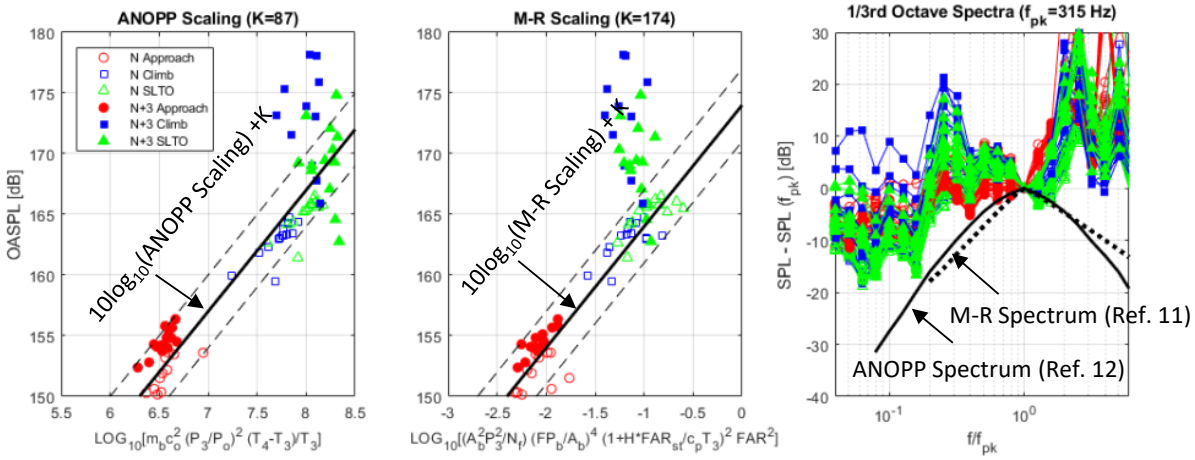

Figure 22. Legacy scaling law analysis with raw pressure

$$p_{nA} = p/NF$$

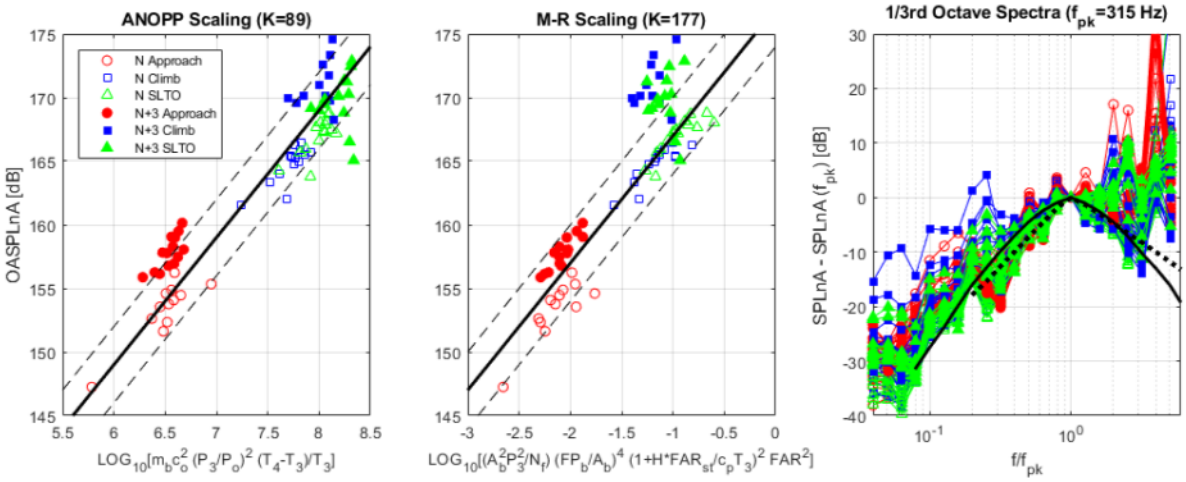

Figure 23a. Legacy scaling law analysis with normalized pressure

$$p_{nB} = p \left| \frac{V_s}{p} \right| \frac{\rho_4 c_4^2}{\gamma_4 - 1}$$

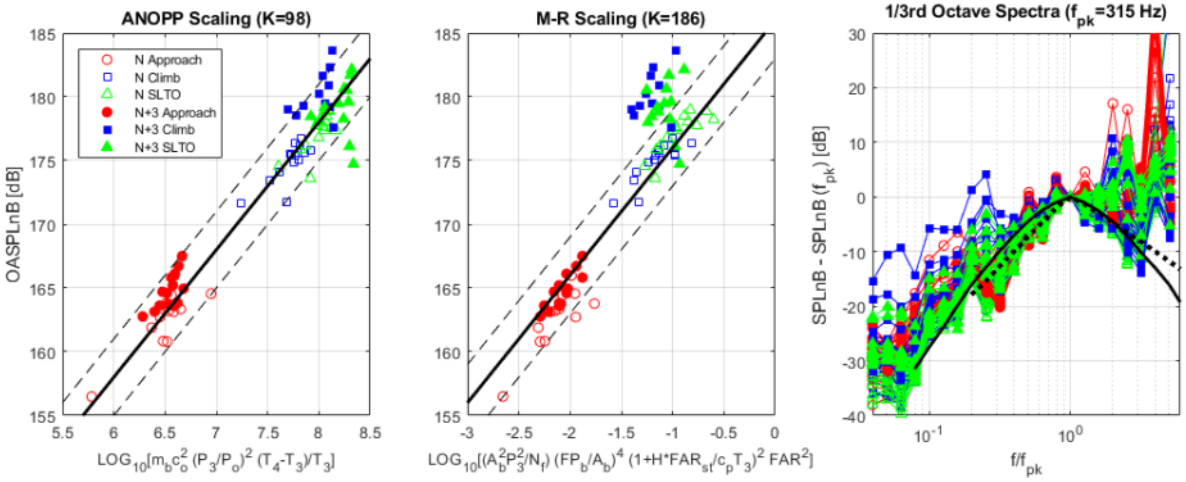

Figure 23b. Legacy scaling law analysis with normalized pressure

$$p_{nC} = p\left|\frac{V_s}{p}\right|\frac{\rho_{f4}c_{f4}^2}{\gamma_4 - 1}\frac{P_4}{Q_f}$$

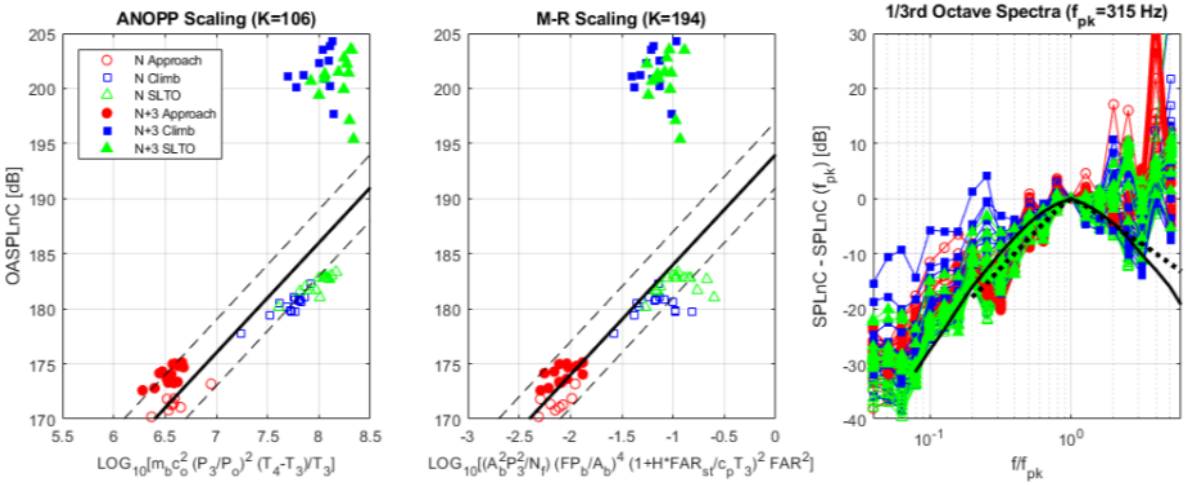

Figure 23c. Legacy scaling law analysis with normalized pressure

$$p_{nD} = p\left|\frac{V_s}{p}\right|\frac{\rho_4 c_4^2}{\gamma_4 - 1}\frac{P_4}{Q}$$

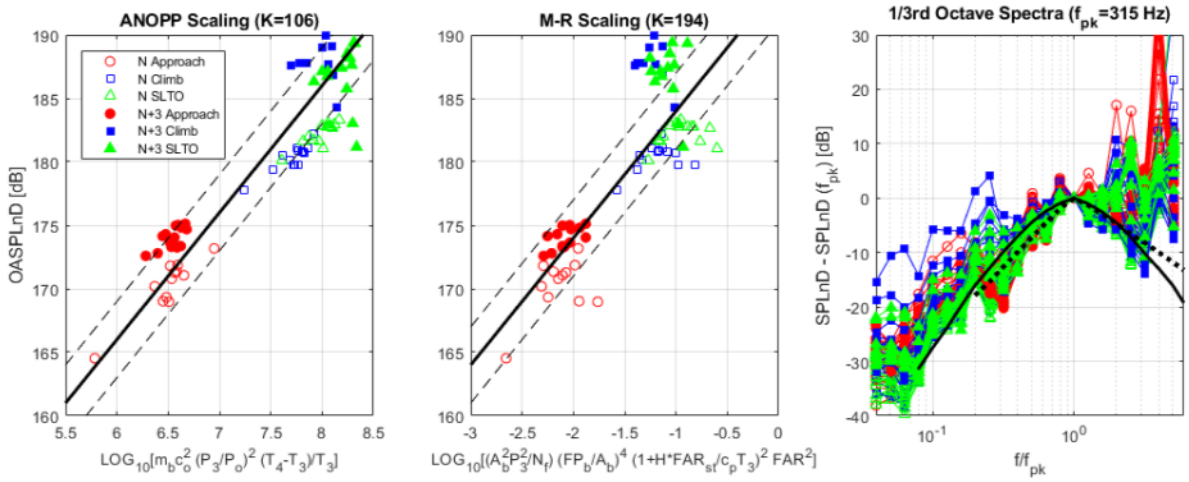

Figure 23d. Legacy scaling law analysis with normalized pressure

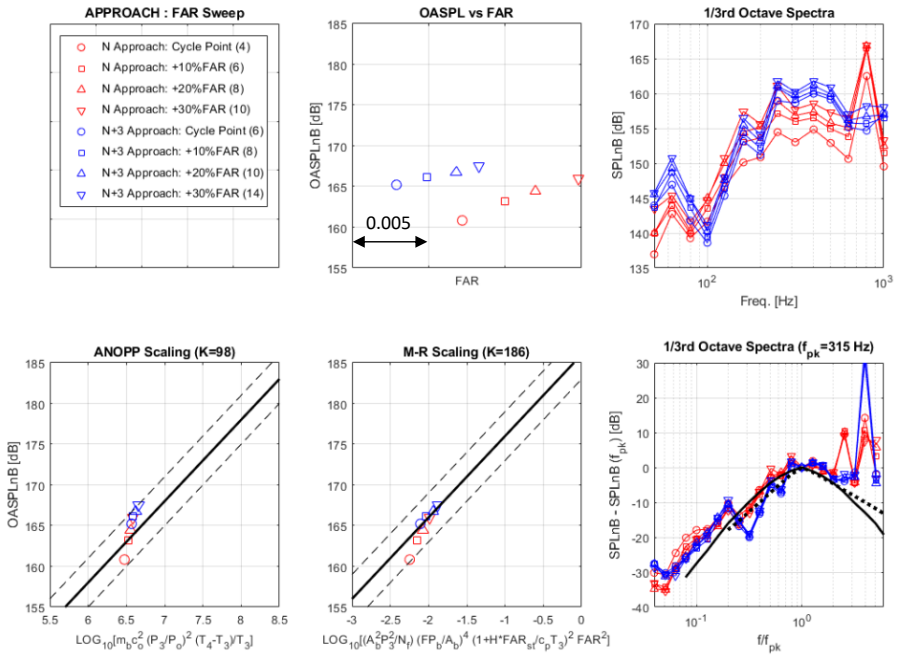

Figure 24a. Legacy scaling law analysis for APPROACH FAR sweep

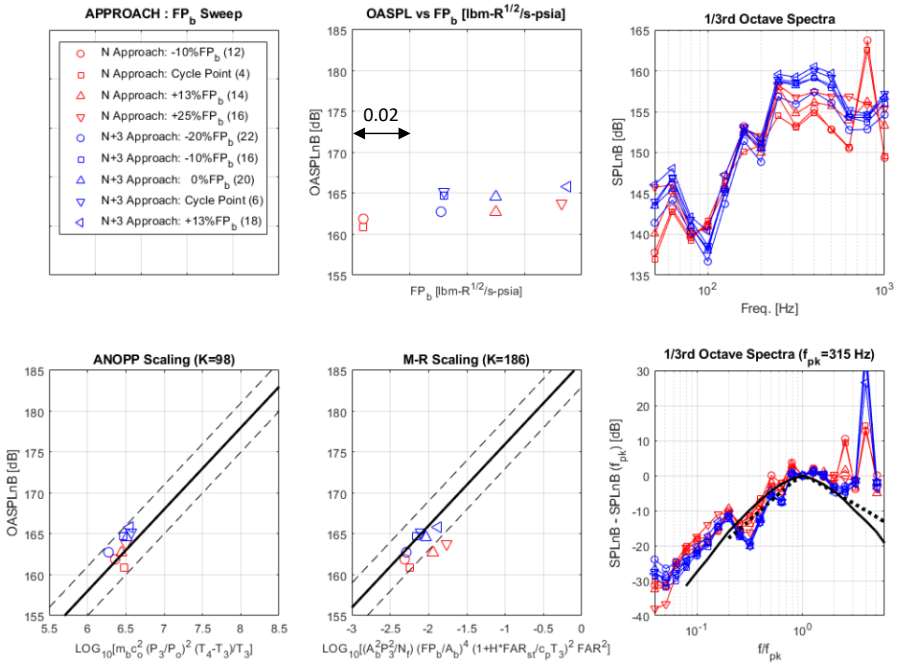

Figure 24b. Legacy scaling law analysis for APPROACH FP_b sweep

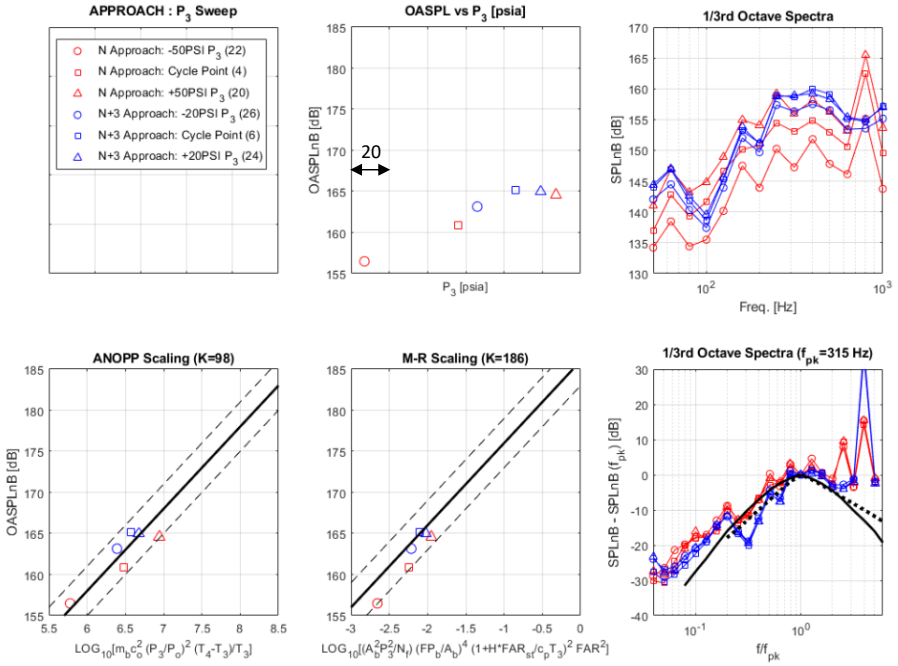

Figure 24c. Legacy scaling law analysis for APPROACH P_3 sweep

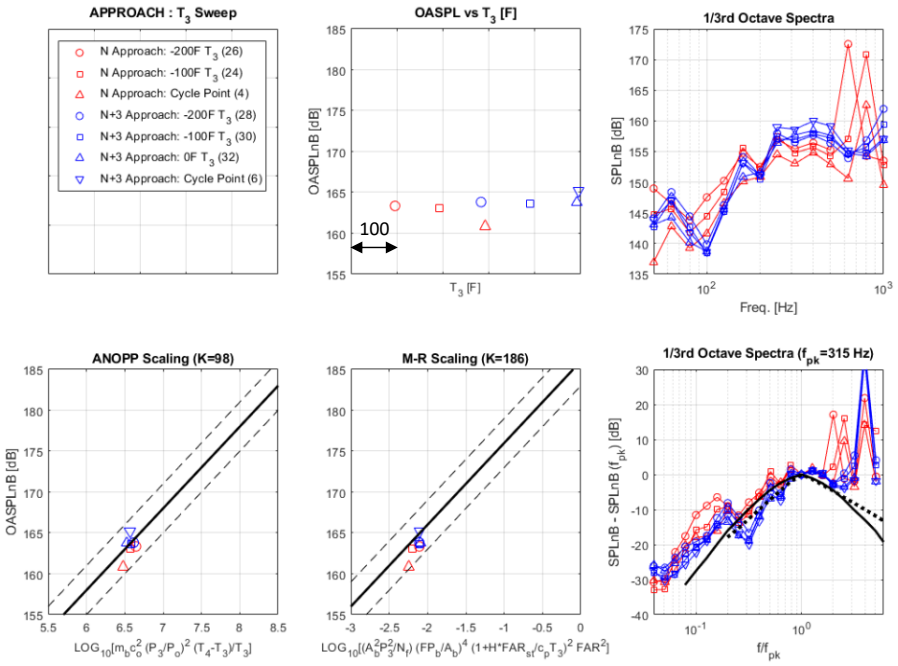

Figure 24d. Legacy scaling law analysis for APPROACH T_3 sweep

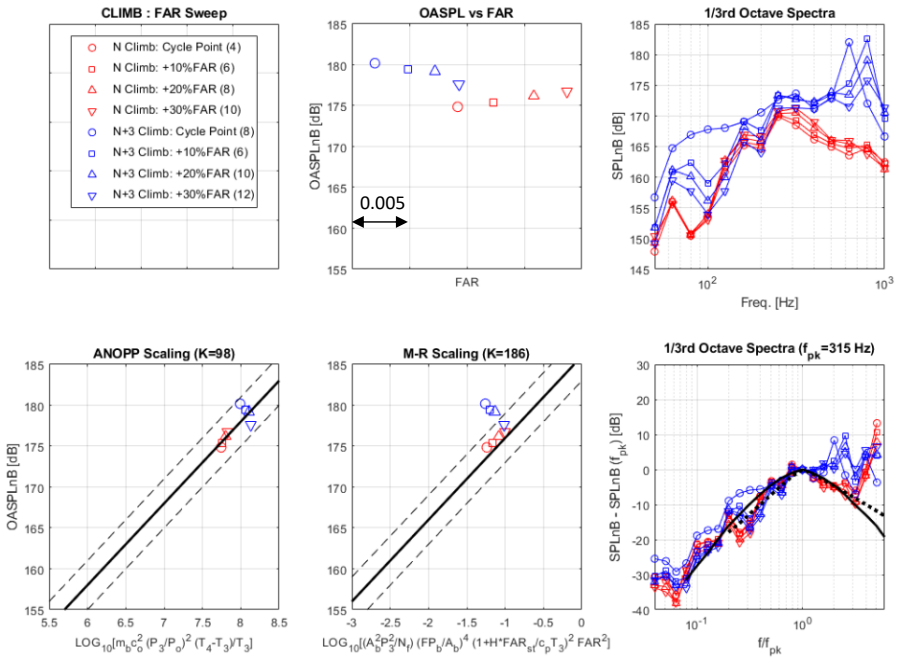

Figure 25a. Legacy scaling law analysis for CLIMB FAR sweep

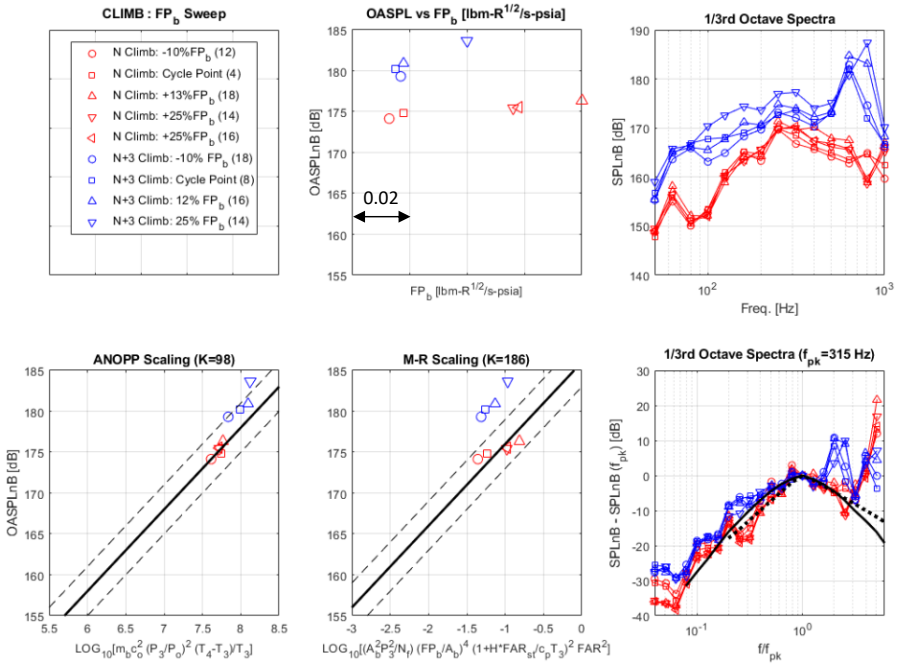

Figure 25b. Legacy scaling law analysis for CLIMB FP_b sweep

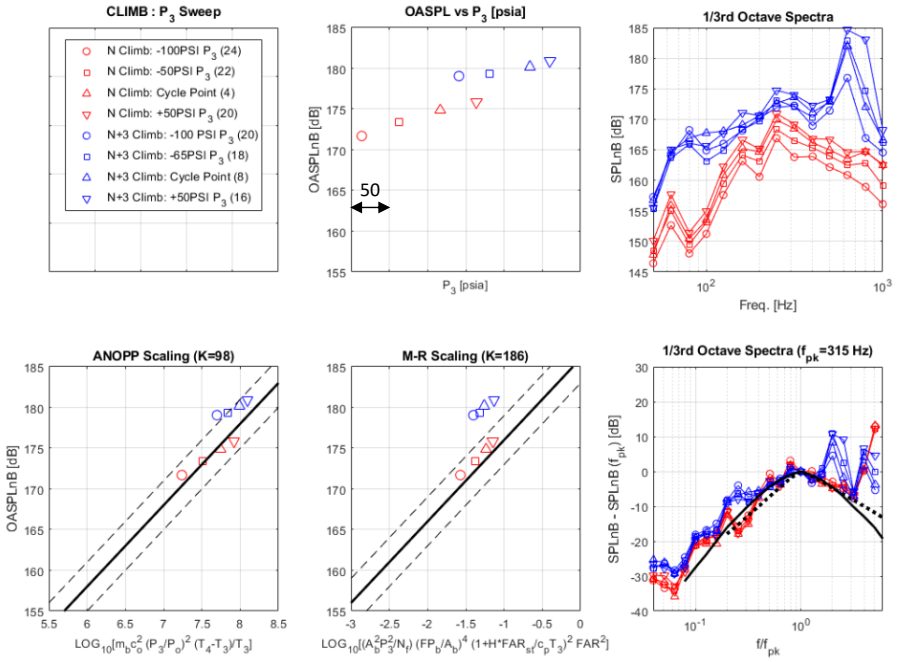

Figure 25c. Legacy scaling law analysis for CLIMB P_3 sweep

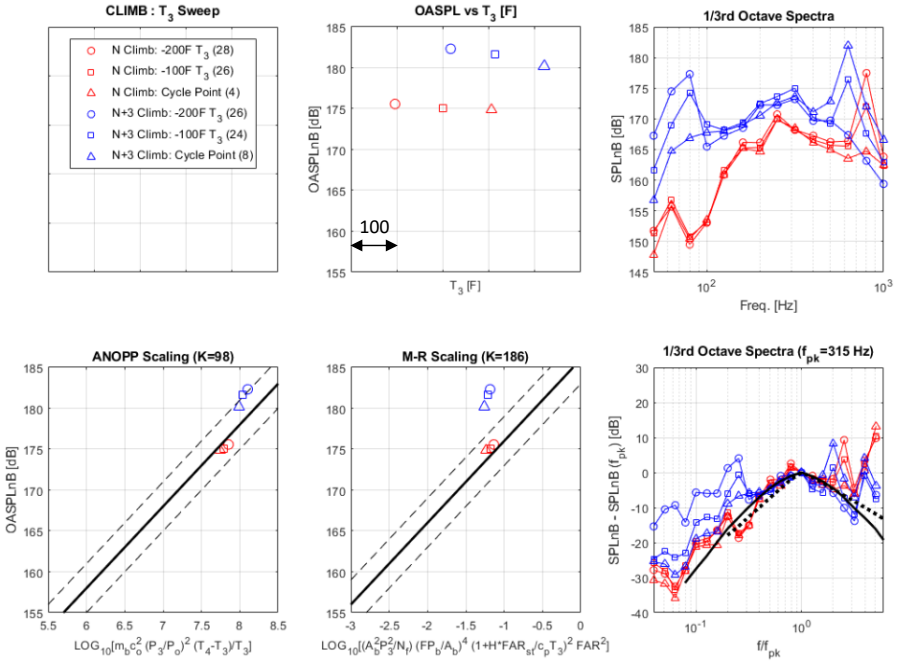

Figure 25d. Legacy scaling law analysis for CLIMB T_3 sweep

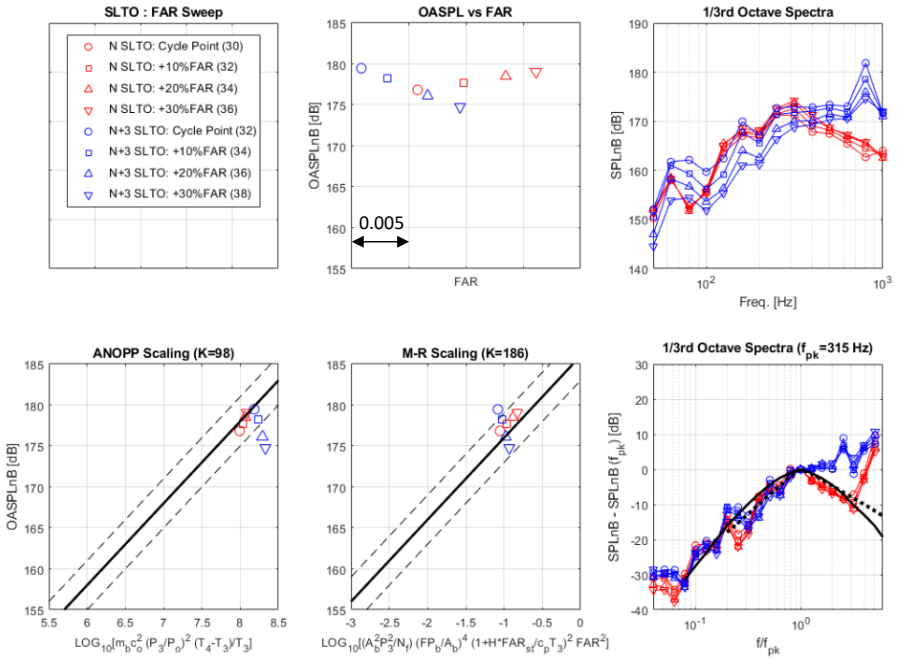

Figure 26a. Legacy scaling law analysis for STLO FAR sweep

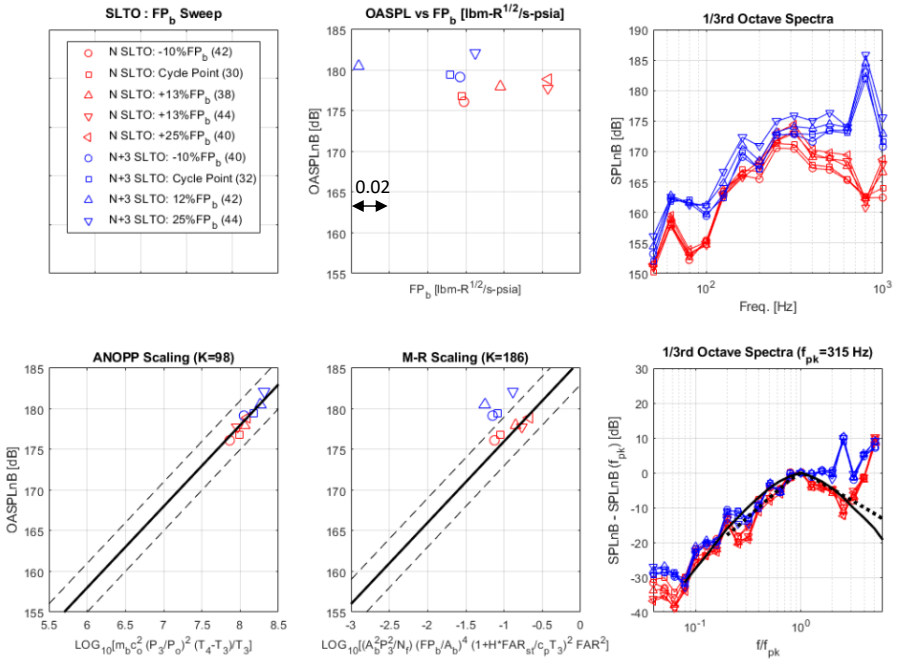

Figure 26b. Legacy scaling law analysis for STLO FP_b sweep

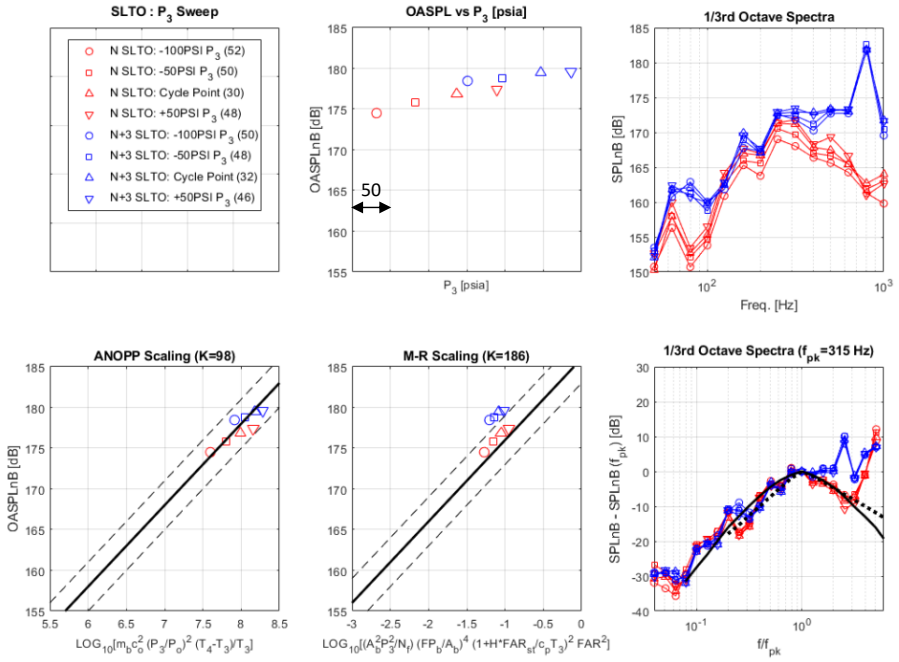

Figure 26c. Legacy scaling law analysis for STLO P_3 sweep

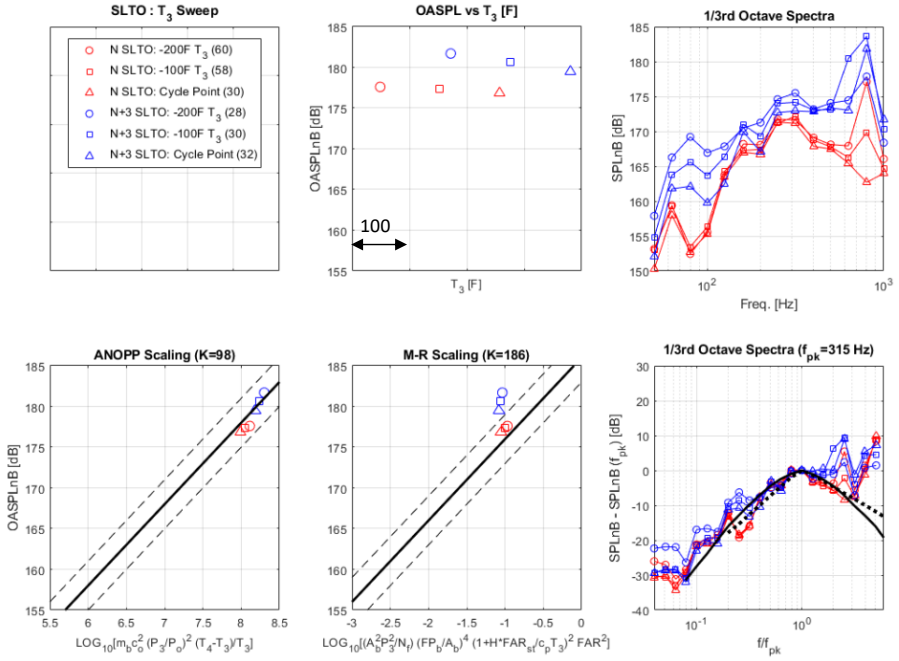

Figure 26d. Legacy scaling law analysis for STLO T_3 sweep

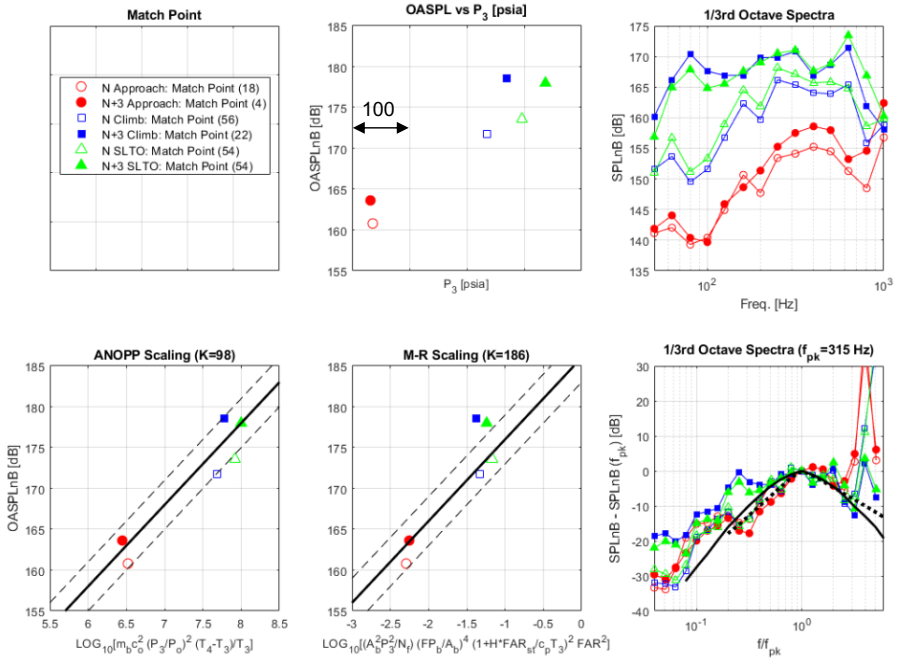

Fig. 27. Legacy scaling law analysis for match points

Direct Combustion Noise Computation

Process Steps

A key aspect of this study is to compute the acoustic power spectrum ($P(\boldsymbol{x}, \omega)$) of the direct noise field by integrating the two-point UHR (Unsteady Heat Release) correlation measurements (via chemiluminescence) with the Green's function of the combustor. The basic formulation is the following equation **[15]**:

$$P(\boldsymbol{x}, \omega) = \int G^*(\boldsymbol{x}, \boldsymbol{s_1}, \omega)\, G(\boldsymbol{x}, \boldsymbol{s_2}, \omega)\, S_{qq}(\boldsymbol{s_1}, \boldsymbol{s_2}, \omega) d\boldsymbol{s_1} d\boldsymbol{s_2} \tag{4}$$

where,

$$S_{qq}(\boldsymbol{s_1}, \boldsymbol{s_2}, \omega) = \int \overline{q(\boldsymbol{s_1}, t)\, q(\boldsymbol{s_2}, t+\tau)} e^{-i\omega\tau} d\tau$$

where G is the Green's function for the test section, and S_{QQ} is the two-point UHR correlation. Because of the complexity of the N+3 test section, in part due to the variable cross section and in part due to the arbitrary boundary conditions at the ends of the combustion section, an analytical Green's function formulation is not possible. Hence, a numerically-based Green's function is needed which is one of the purposes of the FEA model discussed previously.

Figure 28 shows the steps of the direct combustion noise computation. The first step is to process a reference grid image to provide a conversion from pixels to coordinates. This reference grid is taken after a test to provide the most accurate conversion. The second step is to pre-process the UHR images to reduce the resolution from one pixel to 10x10 pixel subareas. In this way, the computational time to integrate the two-point UHR correlations is significantly reduced. The top right images show the mean UHR field before and after pre-processing which indicates the basic large-scale structure remains intact with the resolution reduction. This step is followed by extracting the integrated CH emissions to compute a heat release/CH emissions calibration.

The next step is to extract the relevant eigenfunctions from the FEA model. Since the eigenfunction search tool in COMSOL will return dozens of eigenfunctions, some sort of a down selection is needed to make the computation reasonable. The eigenfunction selection process was developed such that eigenfunctions below 1000 Hz, less than 15% damped and contain significant response in the test section were automatically selected (Fig. 31 illustrates the typical eigenvalue functions).

Before performing the integration of Eqn. 4, a pre-processing step is performed where the Green's function (functions, if multiple receiver points) is (are) computed for each point in the UHR field (using the numerical eigenfunction from the FEA model) and the cross-correlation of UHR for each pair of points. The final step is to combine these two terms to compute the direct field acoustic power spectrum by integrating the Green's functions with the two-point UHR correlations over the combustor volume.

Process Validation

As stated above, an analytical Green's function formulation was not possible and the basis functions had to be extracted from an eigenvalue solution of the FEA COMSOL models (using the data-matched forced response model for each operating point.

From Morse and Ingard **[16]**, the general form of the Green's function is given by:

$$G(\boldsymbol{r}|\boldsymbol{r_o}) = \sum_n \frac{\Psi_n(\boldsymbol{r})\Psi_n(\boldsymbol{r_o})}{V\Lambda_n(k_n^2 - k^2)} \tag{5}$$

where,

$$\Lambda_n = \frac{1}{V}\int_V \Psi_n(\boldsymbol{r})\Psi_n(\boldsymbol{r})dV$$

The Ψ_n are the eigenfunctions and k_n are the corresponding eigenvalues. Λ_n is the volume averaged mode shape. From COMSOL for each mode, the pressure fields can be extracted (which represent the eigenfunction) and the volume averaged mode shapes computed. To save resources, this was only performed in the combustor section where the direct noise (UHR) field and pressure instrumentation to compare with existed.

To validate the numerical Green's function approach, a one-dimensional analytical Green's function for arbitrary boundary conditions was derived for point source at position, x_0, and impedance boundary conditions z_0 and z_L (details of derivation in Fig. 29) and compared with the numerical approach for the block shown in Fig. 30 (upper left). An additional check was obtained by computing a forced response with a small spherical source (Fig. 30 upper right). In the bottom of the figure is the comparison of the Green's functions for a source location in the near corner and response location in far corner of the block. The 1-D analytical solution agrees with both numerical approaches out to the cut-on frequency for the block (1400 Hz) and the two numerical approaches agree out to 4500 Hz (limit of the applied basis function eigenvalues). This result validates the numerical basis function approach for the Green's function.

As mentioned above, to reduce the computation time, a limited set of eigenfunction were extracted from the numerical models. After sensitivity a study, the selection process was automated by extracting eigenfunctions below 1000 Hz with less than 15% damped and also contain significant response in the test section where the source field exist. Figure 31 show the typical set of 14-15 eigenfunctions from 50 Hz to 1000 Hz. It is important to note that applying the data-matched attenuation coefficient (typically $\alpha = 0.35$ Nepers/m in the test section) in the eigensolver resulted in no realistic eigenfunctions found. Only a very low or linear elastic (lossless) value resulted in useful eigenfunctions. This leads to a second validation case to confirm the approach of applying the attenuation coefficient in the direct noise computation (i.e., Eqn. (4)).

This test case is shown in Fig. 32a which consistent of a trapezoidal section similar to the test section, but with simple, rigid boundary conditions. A UHR simulated movie is shown in the figure that was used as a direct noise field in the integration with the Green's function. For comparison, a forced response model with a cylindrical source at the same axial location and diameter as the UHR movie (top of Fig. 32a). To account for the damping needed in the forced

response FEA model to match the data, the wavenumber of Eqn. 5 was made complex using the data-matched attenuation coefficient (i.e., $k = \omega/c - i\alpha$).

Figure 32b shows the results of test case for both linear elastic acoustics and damped ($\alpha = 0.20$). Both the forced response model results and the UHR-Green's function computation are in excellent agreement. In summary, these results validate the approach of applying the data-matched attenuation coefficient in the Green's function and the scripting that performs the integration of the Green's function with the UHR cross-correlation.

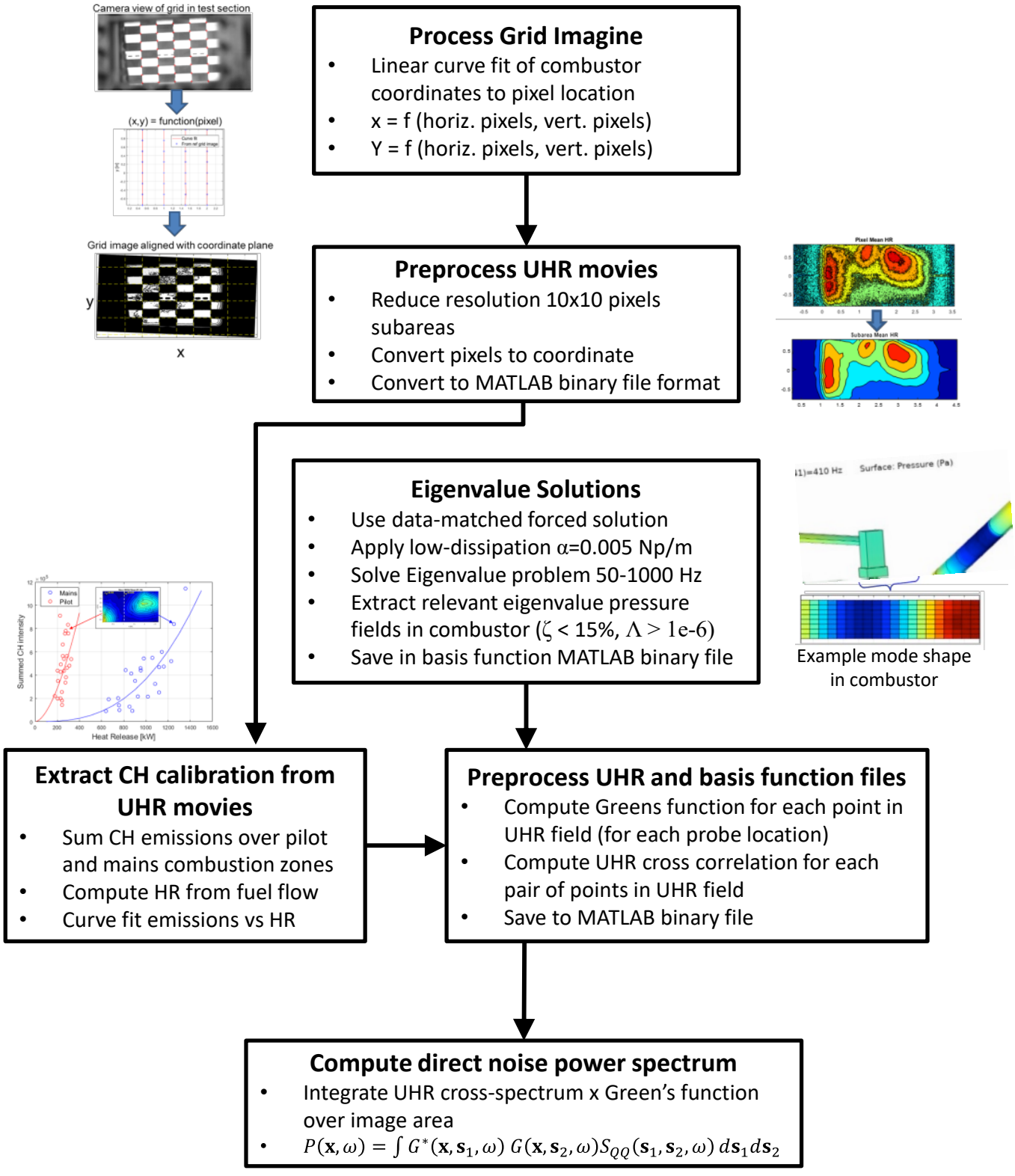

Figure 28. Direct noise computation process

- 1-D Green's function satisfies:

$$\frac{\partial^2 G}{\partial x^2} + k^2 G = \delta(x - x_o)$$

- Look for solution of the form:

$$G^- = Ae^{-ikx} + Be^{ikx}$$

$$G^+ = Ce^{ikx} + De^{-ikx}$$

- At x_o:

$$G^-(x_o) = G^+(x_o)$$

- Integrating the Green's function formulation around x_o

$$\int_{x_o^-}^{x_o^+} \left[\frac{\partial^2 G}{\partial x^2} + k^2 G \right] dx = \int_{x_o^-}^{x_o^+} \delta(x - x_o) dx$$

- gives:

$$\left. \frac{\partial G}{\partial x} \right|_{x_o^-}^{x_o^+} = 1$$

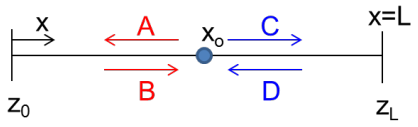

- Together with the specified impedances:

$$\left. \frac{G}{\rho c u} \right|_{x=0} = z_0 \qquad \left. \frac{G}{\rho c u} \right|_{x=L} = z_L$$

- solve for A, B, C and D.
- Exact solution, no frequency limit (other than cut on model limit)

Figure 29. Analytical 1-D Green's function for validation

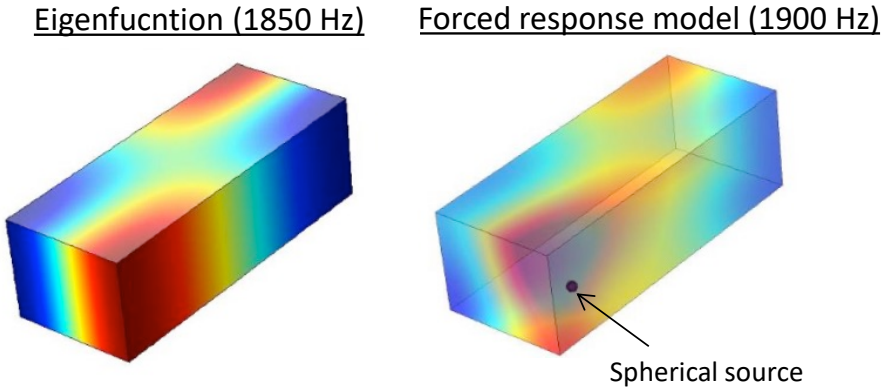

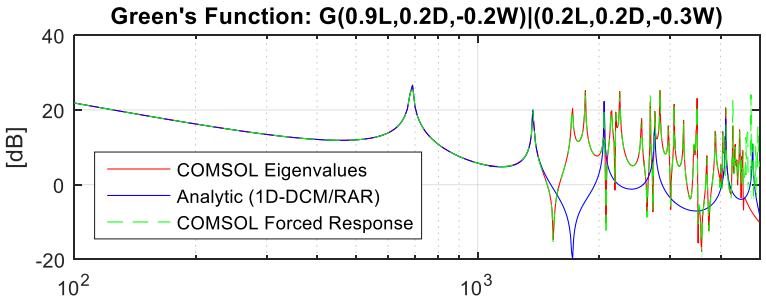

Figure 30. Numerical Green's function validation

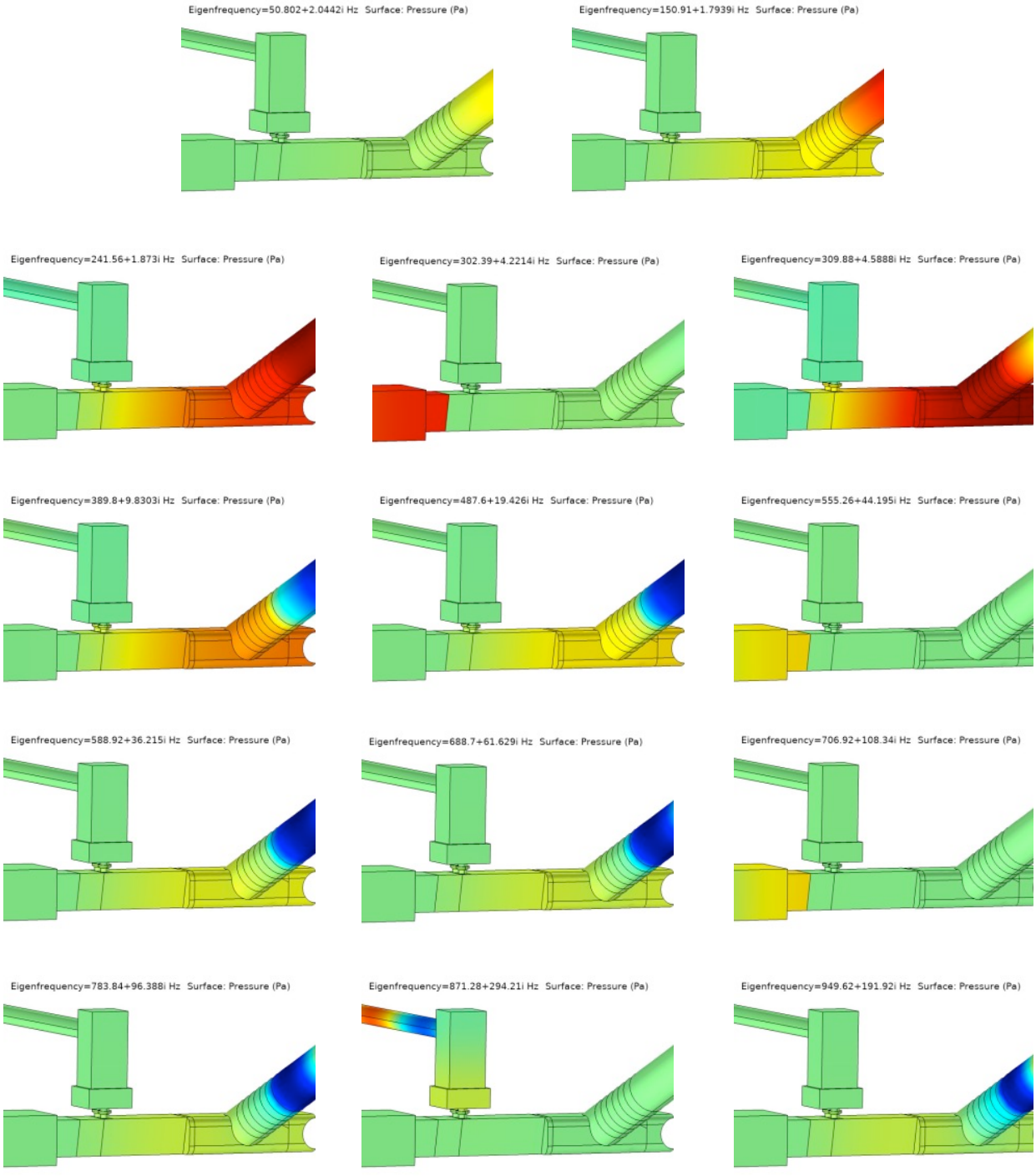

Figure 31. Typical selected eigenfunctions from FEA model for Green's function

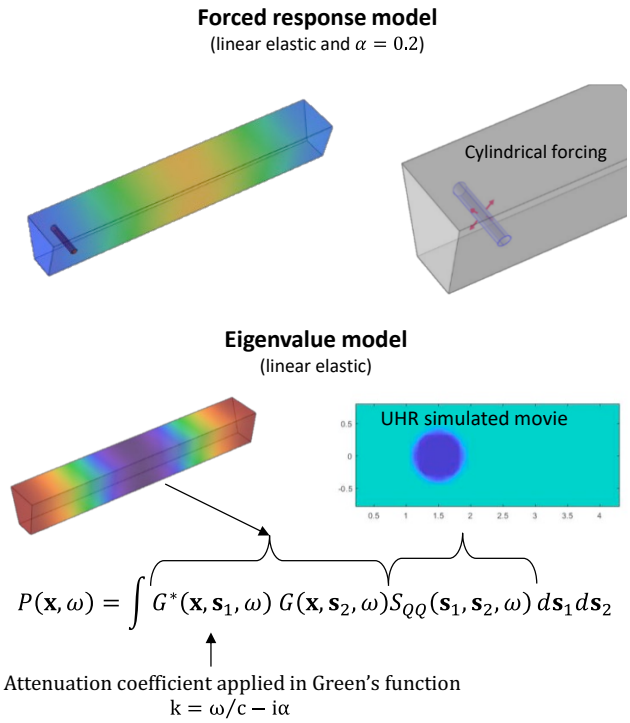

Fig. 32a. Validation of UHR to pressure spectrum computation

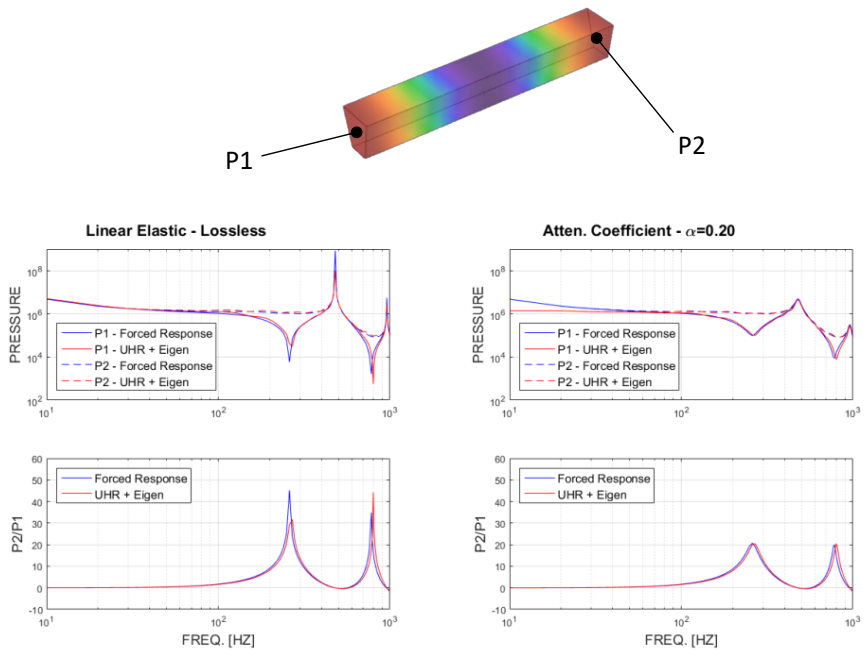

Fig. 32b. Validation of UHR to pressure spectrum computation

Emissions Spectroscopy Study

During the dynamics imaging test for the NRA N+3 Combustor Technology Contract (NNC14CA30C), an additional (low-speed) video camera with a filter wheel was used to perform a preliminary emissions spectroscopy study to identify the best surrogate species radiation for heat release rate. The filter wheel enabled the radiation of different species to be imaged without needing to shut down (which takes hours). Figure 33 shows a photograph of the low-speed video camera with filter wheel next to the high-speed video camera that was being used to image the dynamics of the flame.

Since the main injectors provide a fully pre-mixture of fuel and air, the region near the main exits was used to calibrate the radiation versus equivalence ratio as illustrated on the left side of Fig. 34 which labels this area the "region of interest" (ROI). Here the equivalence ratio is known by the measured air and fuel flow rates. The middle plot shows the radiation intensity for OH, CH and C2 (corrected for broadband radiation of CO2). The data indicates the radiation of the CH species provides the most monotonic relationship between equivalence ratio and signal intensity. The plot on the right side of shows the visible light intensity versus equivalence ratio is somewhat linear until soot radiation dominates the signal. Subsequent measurements at higher pressure provided similar CH results (shown in Fig. 35). In summary, initial in situ species radiation measurements indicate the CH species to be a reasonable surrogate for UHR.

During actual testing to obtain high-speed CH images, attempts to simultaneously obtain CO2 emission were unsuccessful which made relying on the above CH calibrations not possible. Instead calibration was derived from the in-situ, high-speed CH imaging data with the known fuel flow rate of the pilot and mains.

Figure 35 shows the complete results of the spectroscopy screening study with the full range of operating pressures from 121 to 532 psia (larger circular symbols, mostly filled) which show little or no trending with pressure. For comparison, the averaged, peak intensity from the in-situ, high-speed CH imaging data is plotted in the figure for the main (smaller blue circular symbols) and pilot (smaller red square symbols) combustion zones as illustrated in the figure. The data includes all operating conditions for the N+3 configuration. The in-situ main data follows the spectroscopy results well, whereas the pilot trending is significantly different (not surprising since the mains are premixed and pilot is non-premixed).

Given these results of the in-situ peak intensity trending of the mains matching the more carefully area-averaged spectroscopy study results and the higher slope of the pilots, a new calibration approach was developed: 1. Apply different calibrations in the premixed mains and non-premixed pilot zones. 2. Use area-integrated CH radiation versus fuel flow to the two zones to derive the calibrations. Figure 36 show the resulting calibrations for the mains and the pilot zones. Likewise, a similar analysis was performed with the in-situ, high-speed CH imaging data for the N configuration.

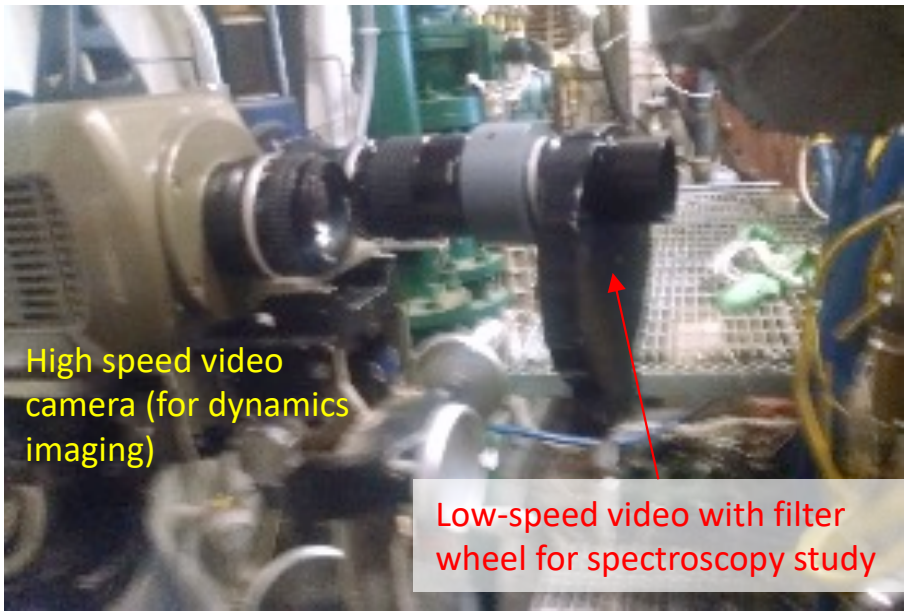

Figure 33. Spectroscopy screening test setup

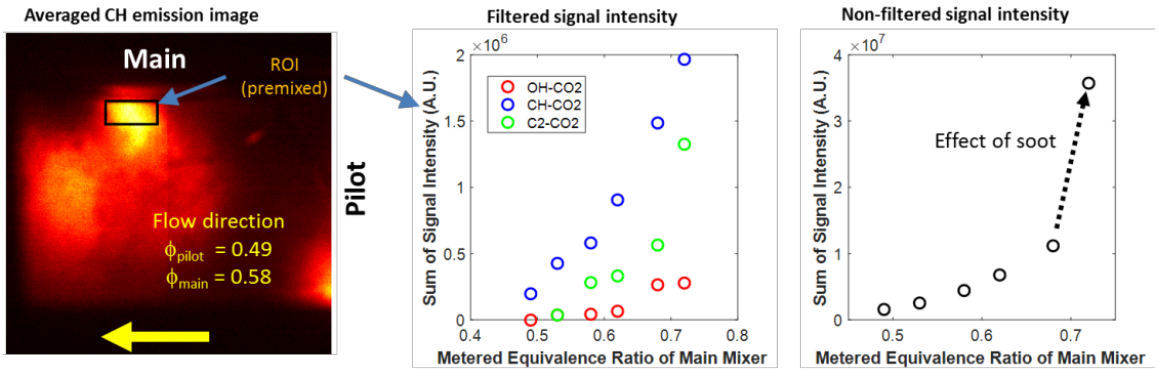

Figure 34. Spectroscopy screening test results

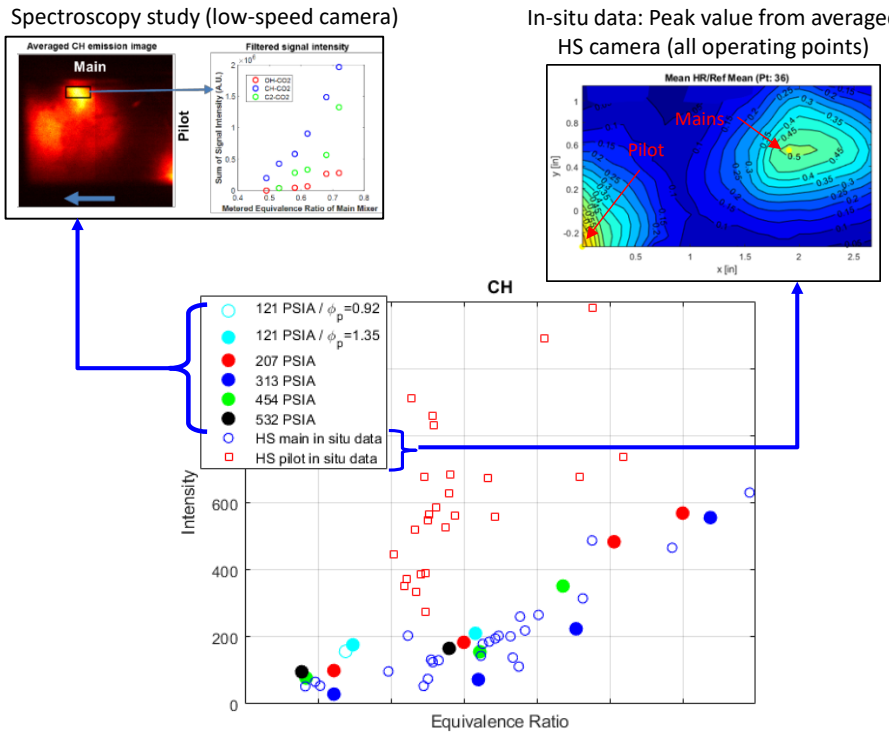

Figure 35. Comparison of spectroscopy study and in-situ, high-speed CH imaging data

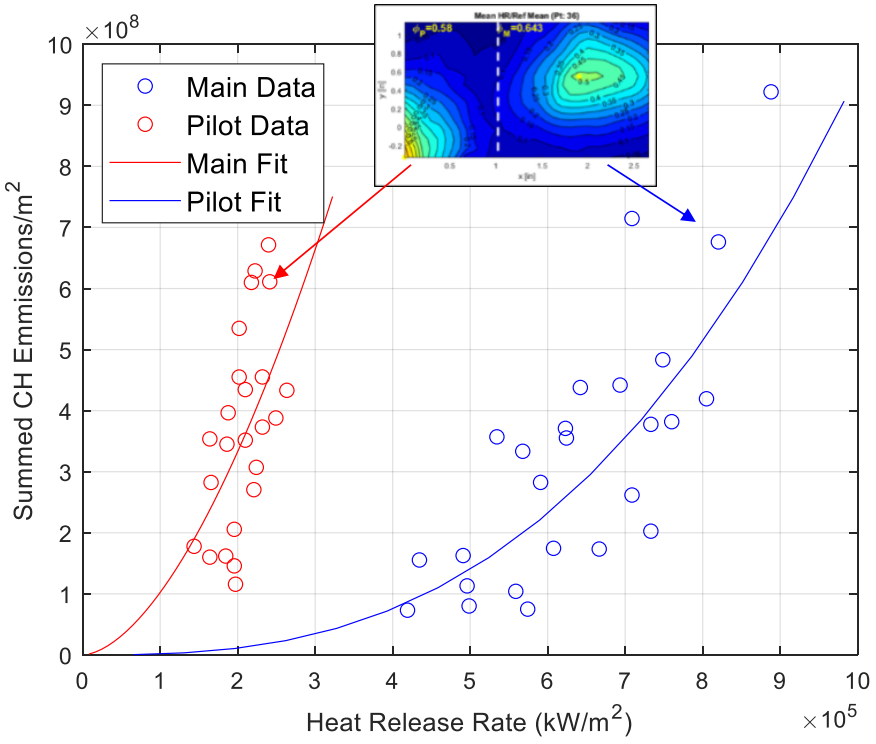

Figure 36. CH intensity/UHR calibration from in-situ, high-speed imaging data

Direct Noise Power Spectrum Analysis

This section shows the results of all the direct noise computations. Note that N configuration UHR imaging data was not obtained for the climb and SLTO conditions due to window failure cause by, in part, high tones experienced while transitioning to desired operating point and possibly due to a residual small raised area on the window seat from the repair of the slot air-cooling injection lip (may have caused a local stress). Due to limited facility availability, a timely window replacement was not possible.

Figure 37 shows the N+3 cycle points for approach, climb, and SLTO. For each condition, the top figure shows the narrow band spectrum of the measured bulkhead pressure (black line) and the spectrum of the computed direct noise (red line) for comparison. In addition, a computed direct noise for an aft location (blue line) is shown, though there is no measurement at that locations to compare with this computed spectrum. These locations are illustrated in image at the top of the figure.

Below are colored contour plots of the mean UHR and RMS UHR (both normalized by peak mean UHR for that condition) with the locations of the bulkhead, pilot, top wall, and mains schematically shown for reference. The peak mean UHR value is labeled in red for each conditions. The colored contour lines are consistent for all conditions (i.e., 0-1.0 mean UHR range and 0-0.3 RMS range corresponds to blue to yellow for all the conditions and the following Figs. 38-41). The solid horizontal line in the contour plots illustrates the vertical middle of the combustor (labeled "CL"). The dots in the mean UHR contour plots correspond to where the two-point integrations were performed.

Clear from the contour plots is the UHR field is only partially captured in the image despite attempts to capture as much of the field as possible using oblique camera viewing angles. Comparing the measured bulkhead spectra (black line) with the computed direct noise spectra (red line), it is also clear that the modal content of the direct noise spectrum is significant less than that of the measured spectrum. This difference is true for all the conditions for which the direct noise was computed. It is speculated that this difference is due to more than integrating over a partial UHR field and that is more related to the measured spectra consisting of both the direct and indirect noise. This would suggest the indirect noise magnitude is on the order of the direct noise magnitude. Another observation is the topological difference in the pilot flame zone for approach versus that of climb and SLTO where the pilot zone is significantly reduced in size. Also, for the approach condition, there are two discernible RMS peaks in the UHR field versus one for climb and SLTO.

Also, notable, is the level of the computed direct noise level is significantly lower than the measured bulkhead spectra for the approach condition (~20 dB). It is speculated that a significant portion of the UHR field is out of the range of the imaging window. This was true for all the approach conditions.

In the following figures, a comprehensive presentation of all the computed direct noise SPL and UHR field data are given in terms of the four parameter sweeps (*FAR*, FP_b, P_3, and T_3). In addition to the plots shown in Fig. 37, and additional plot is given for each case which quantifies

the local source contribution by plotting the vertically summed OASPL versus axially location. For example, see the bottom row of plots in Fig. 38a. The red circular symbols are a sum of all the direct noise contributions at that axial location (the vertical set of points shown in the mean contour plot in Fig. 37 at that axial location) for the bulkhead location (so-called "ΔSPL BLKHD" in the legend). The blue circular symbols are the same for the aft location. The horizontal red and blue lines are the OASPL for the entire UHR field. In addition, at each axial location the local ΔSPL is split between "UPPER ZONE" (dashed line) and "LOWER ZONE" (dotted line) which further subdivides the local OASPL level to above and below the yellow dashed line in the RMS contour plot. This subdivision of the UHR field was suggested by the two distinct peaks in the RMS contours, one in the upper zone, and one in the lower zone.

Similarly, for climb and SLTO it was natural to subdivide the UHR field between the pilot and the main combustion zones. Figure 39a show an example of this subdividing for the OASPL contribution. Like the approach condition plots, the axially local contribution is shown as circular symbols. However, in this case, the noise source field is subdivided by the vertical yellow dashed line in the RMS contour plot (separating, roughly, the main and pilot combustion zones). In the OASPL plot, the dashed lines upstream of that axial location correspond to the contribution from all the UHR field points upstream of the yellow line (pilot zone) and likewise downstream of that axial location corresponds to the contribution from all the UHR field points downstream of the yellow line (main zone).

Note, the number in parenthesis in the title for each condition, identifies the point number of the test. Referring to the corresponding appendix Tables A3 and A4 (sorted by configuration and operating condition), the exact operating conditions can be identified.

Approach N+3

Figure 38a, b, c, and d show the N+3 approach results for the parameter sweeps *FAR*, FP_b, P_3, and T_3, respectively. An area of window fouling is noted in the Fig. 38d contour plot where variation in patterns should be discounted. To a lesser extent this fouling exists for the other conditions.

The *FAR* parameter sweep (Fig. 38a) shows the mean UHR field expanding somewhat as the *FAR* is increased. Also, the RMS field shows a significant change in that the peaked values become more local with increasing *FAR*. Consistent with the measured OASPL, the computed direct noise OASPL increases with *FAR*. For the bulkhead location, the largest contributions to OASPL occur close to bulkhead (likely due to proximity), whereas for the aft location, the contribution are nearly equally spread out over most of the axial distance from pilot to mains and this distance increases with increasing *FAR*. The OASPL contributions between the upper and lower zone appear to be approximately equal.

Climb and SLTO N+3

Figures 39 and 40 show the corresponding direct noise/UHR field results for N+3 climb and SLTO. For the most part, similar observations are made for both operating conditions.

The RMS fields and the computed, direct-noise OASPL for the *FAR* parameter sweep both trend downward with increasing *FAR* (compare solid red and blue lines in the bottom of Figs 39a and 40a). This trending is consistent with the measured OASPL (and opposite the legacy scaling laws).

With one exception, the dominate direct-noise source location for the both the aft locations is observed to be the pilot combustion zone. The exception is the climb temperature excursion (see -200 F and -100 F T_3 in Fig. 39d) where the conditions are equally or nearly equally split between the pilot and main combustion zone (i.e., the dashed red line in the OASPL plots are nearly equal upstream and downstream of the yellow line in the RMS contour plot). For the aft OASPL, the contribution is nearly equally split between the pilot and main combustions zone for most conditions.

Approach N

For the N configuration, as noted above, UHR imaging data was only obtained for the approach condition (Figs a-d. 41). This data set suffered from a cracked and fouled window (noted in the Figs a-d. 41). In addition to obscuring the image data analysis, it also biases the calibration to overestimate the UHR (i.e., the heat release rate computed from fuel flow represents the total heat release rate, however, only part of the CH emissions is captured). Of course, this partial realization of the UHR field is true for the previously presented data since, due to window limitations, the heat release field was partially not realized, it is more extreme for this data. The large difference between the computed direct noise spectra of the bulkhead and the aft location (aft location is over 20 dB higher) is likely due to the above problems (obscured view from fouling near the bulkhead and biased CH-heat release rate calibration.

Comparing the N+3 approach (Fig. 38) with the N approach, the UHR images, from what is visible, show the combustion zone is much larger and extends beyond the axial limit of the window. With additional air introduced by the dilution jets (just at the downstream end of the window) into a fuel rich zone, the flame likely to extend significantly further downstream.

Since the UHR field is partially obscured, there is some risk analyzing the local contributions to the OASPL for source location identification. Despite this comprise, the axial distribution of OASPL is shown as with the previous data set, though no attempt was made to further subdivide the contributions (e.g., upper vs lower combustion zone). The results appear to show the contributions to the OASPL to be equally spread out over most of the combustion zone, somewhat similar to the N+3 approach results for the aft location.

In summary, the UHR field analysis shows distinctively difference combustion zones between the approach N and N+3 and between N+3 approach and N+3 climb/SLTO. For N+3 climb and SLTO, the dominate noise source for most conditions for the bulkhead OASPL was determined to be the pilot combustion zone but nearly equally split between the pilot and main zones for the aft OASPL. Spectrum comparison between measured and computed direct-noise using UHR field/Green's functions suggests the indirect noise field to be significant.

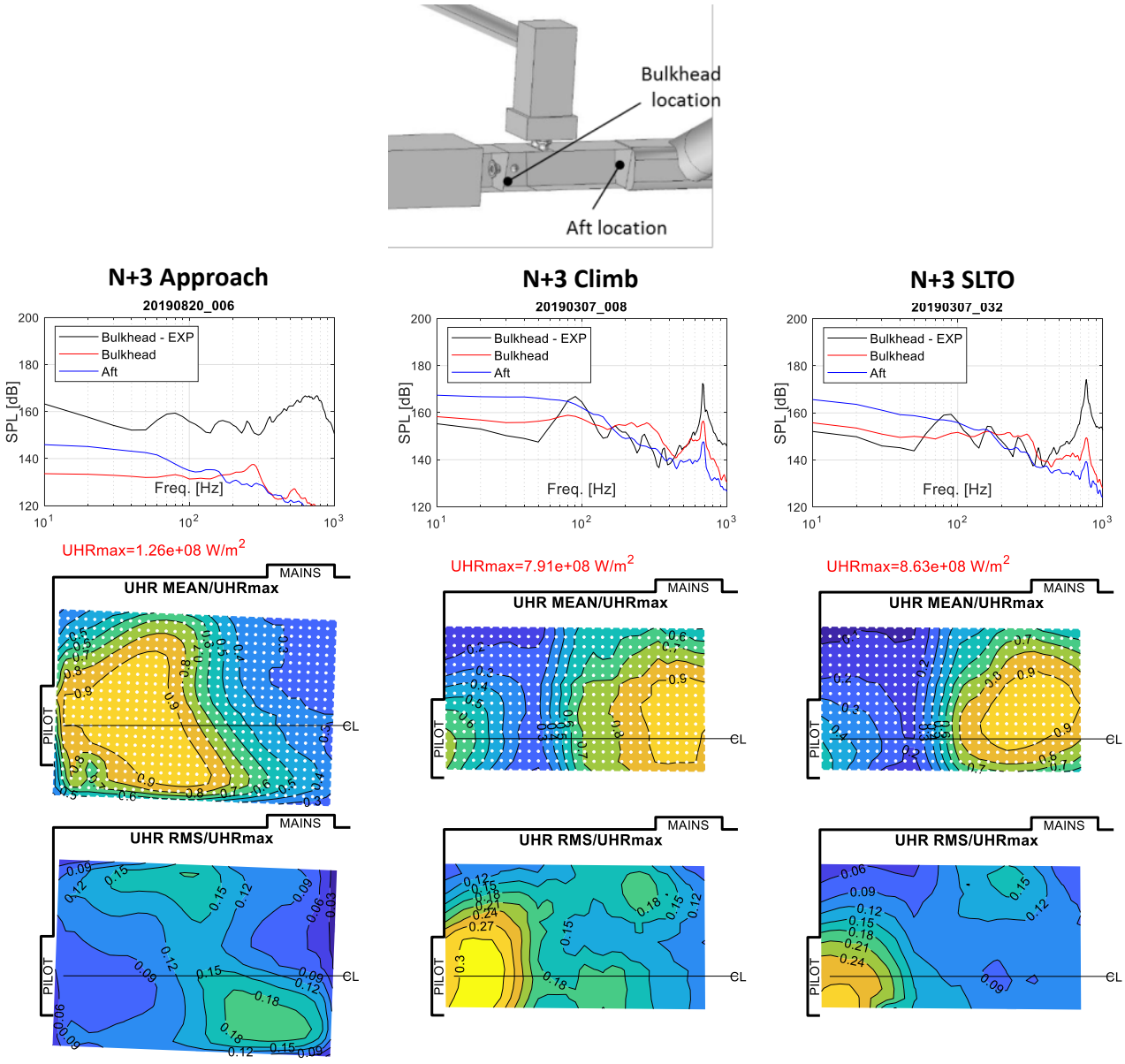

Figure 37. Comparison of computed direct-noise spectra with measured spectra

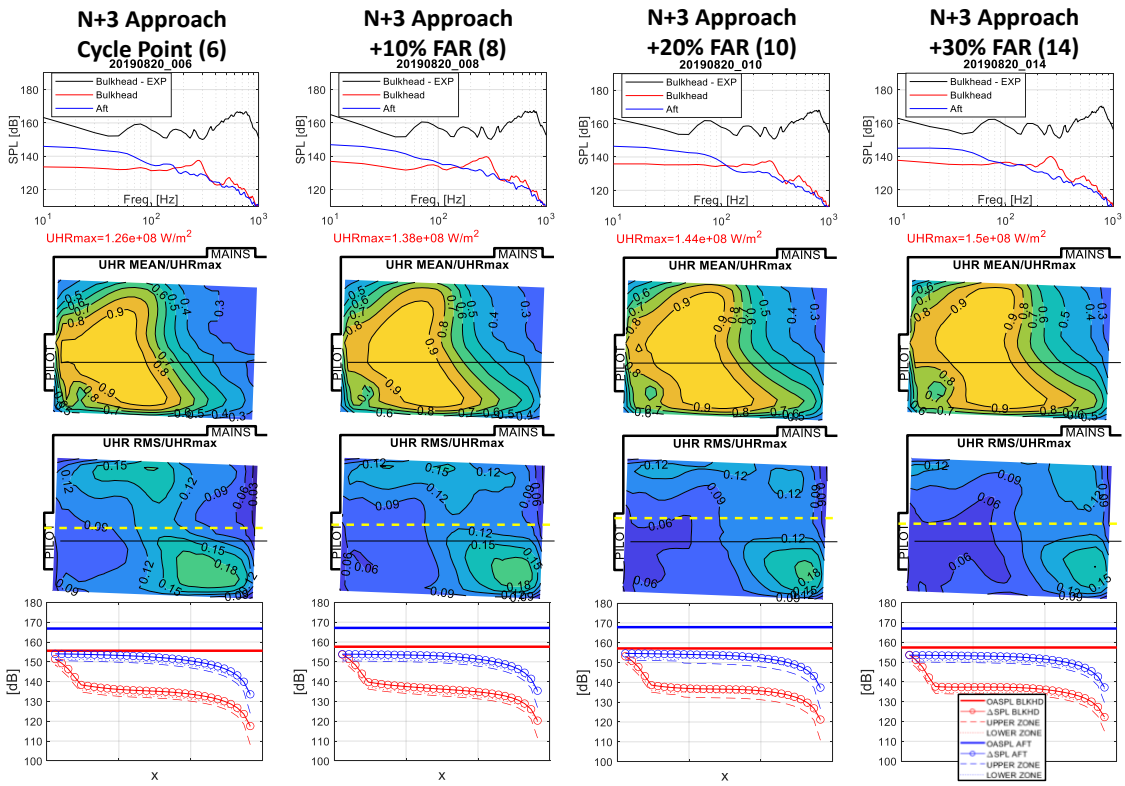

Figure 38a. Direct-noise analysis for N+3 APPROACH FAR sweep

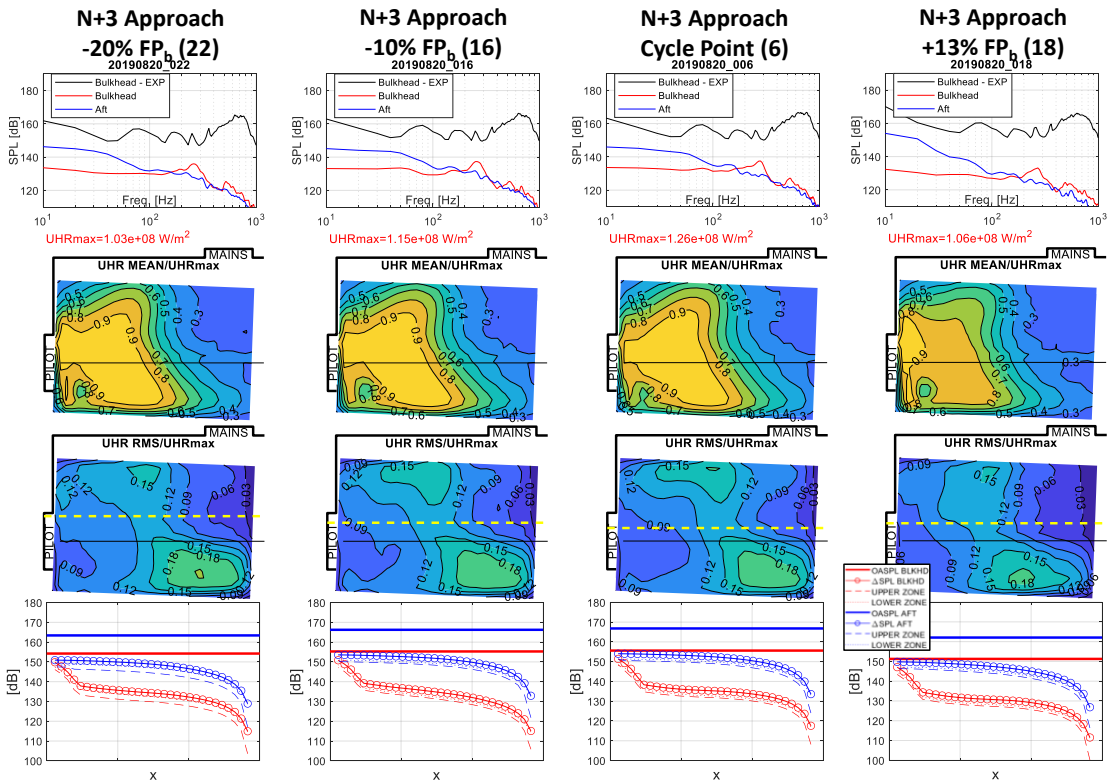

Figure 38b. Direct-noise analysis for N+3 APPROACH FP_b sweep

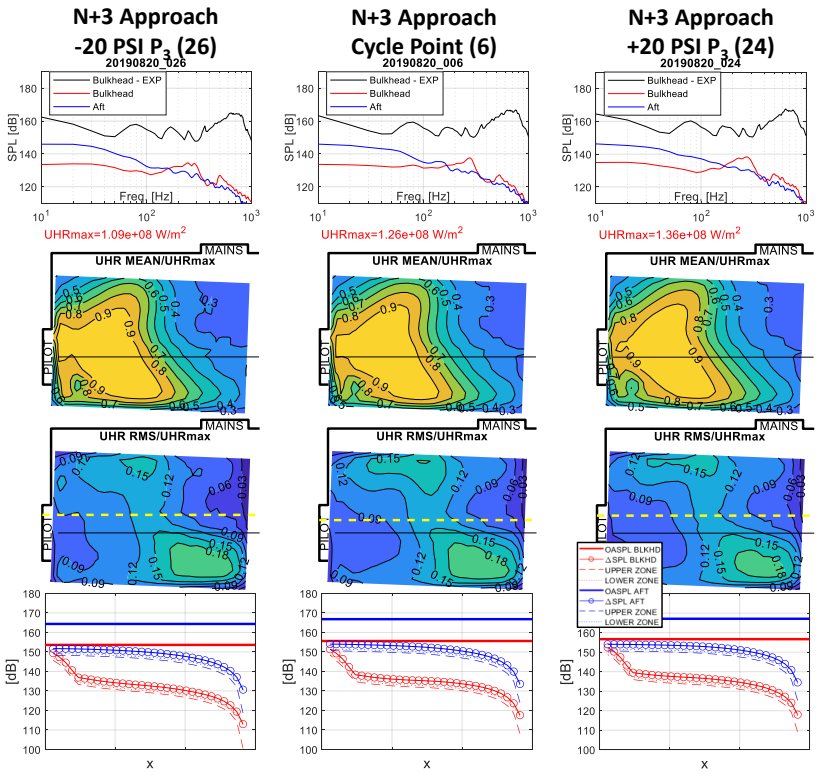

Figure 38c. Direct-noise analysis for N+3 APPROACH P_3 sweep

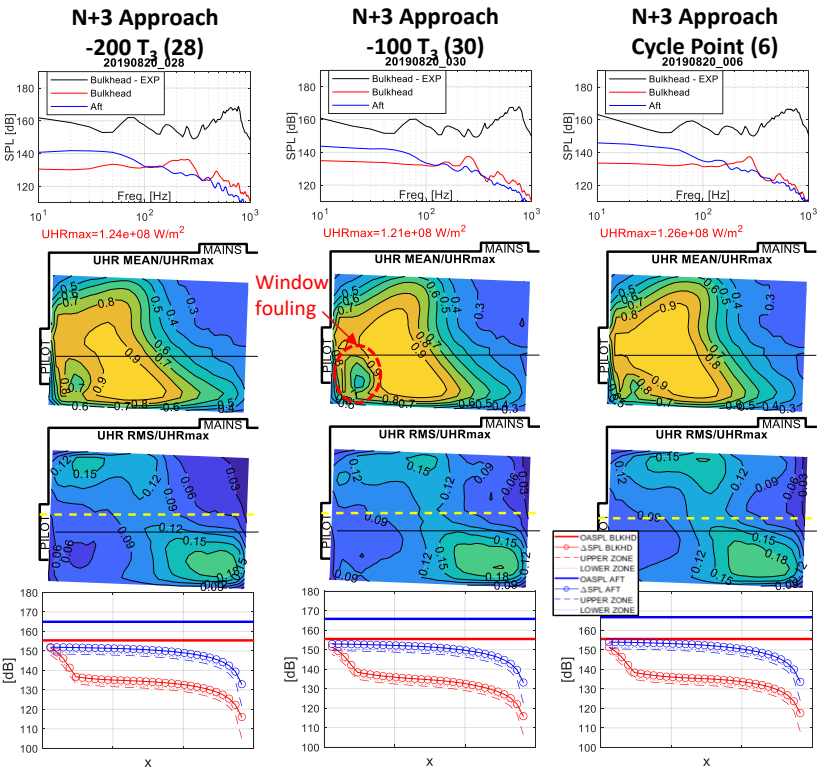

Figure 38d. Direct-noise analysis for N+3 APPROACH T_3 sweep

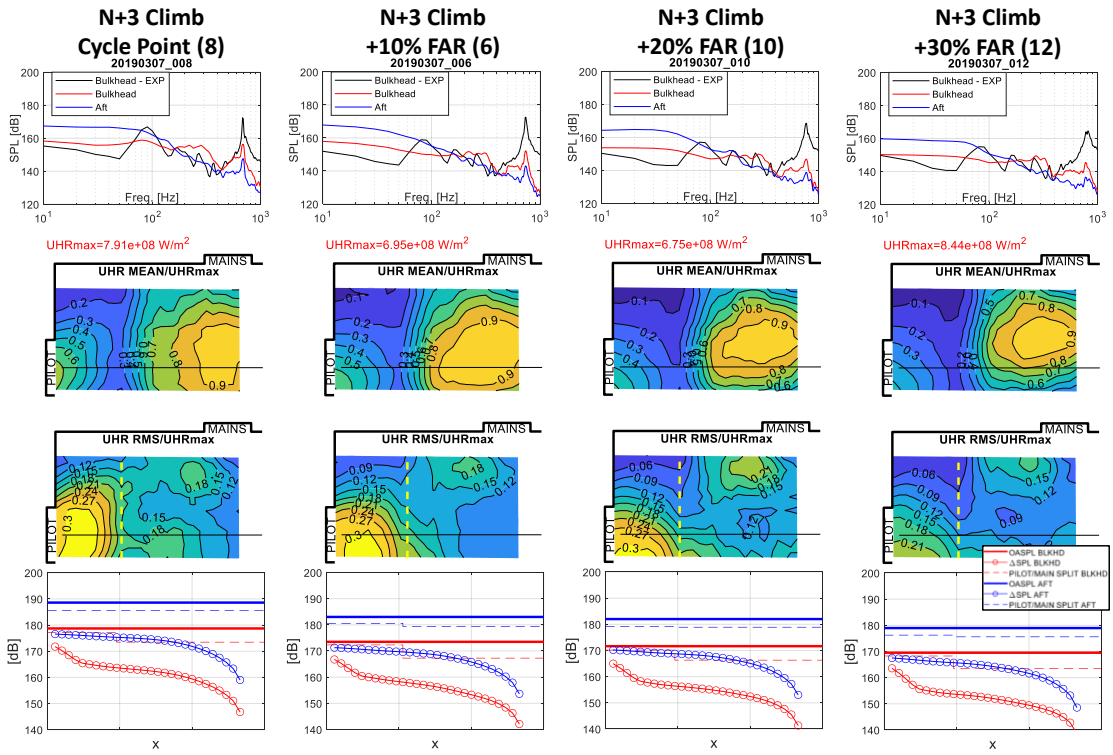

Figure 39a. Direct-noise analysis for N+3 CLIMB FAR sweep

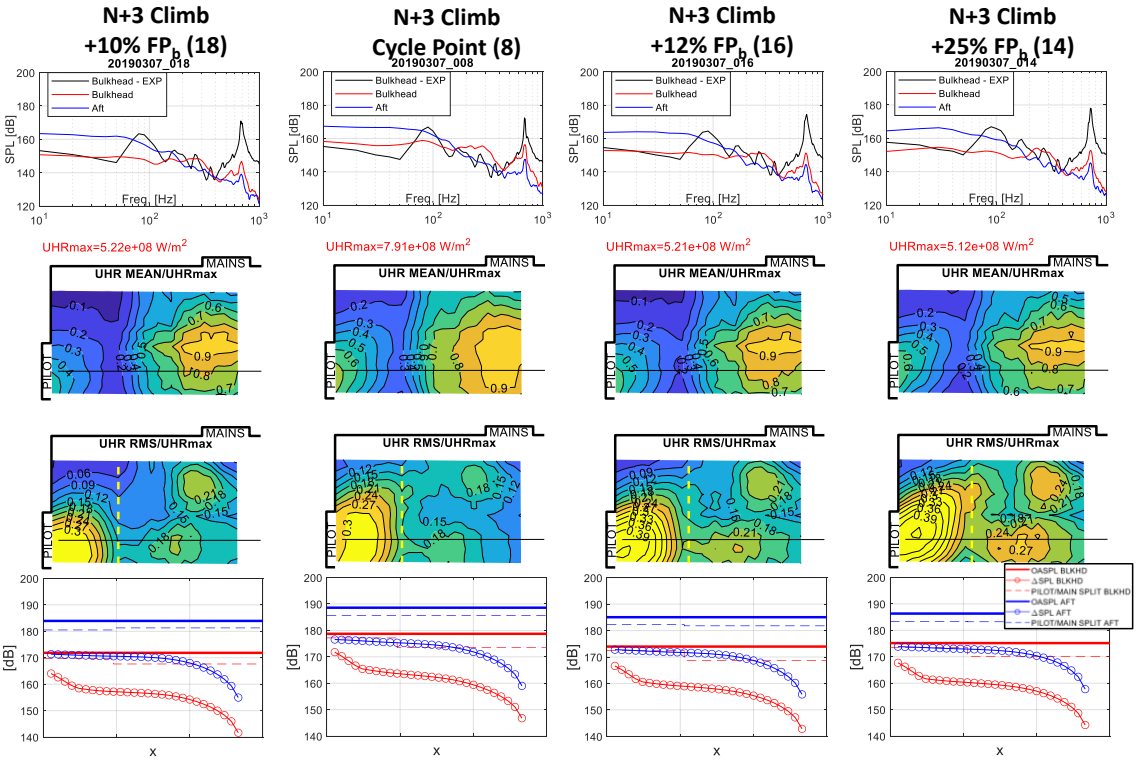

Figure 39b. Direct-noise analysis for N+3 CLIMB FP_b sweep

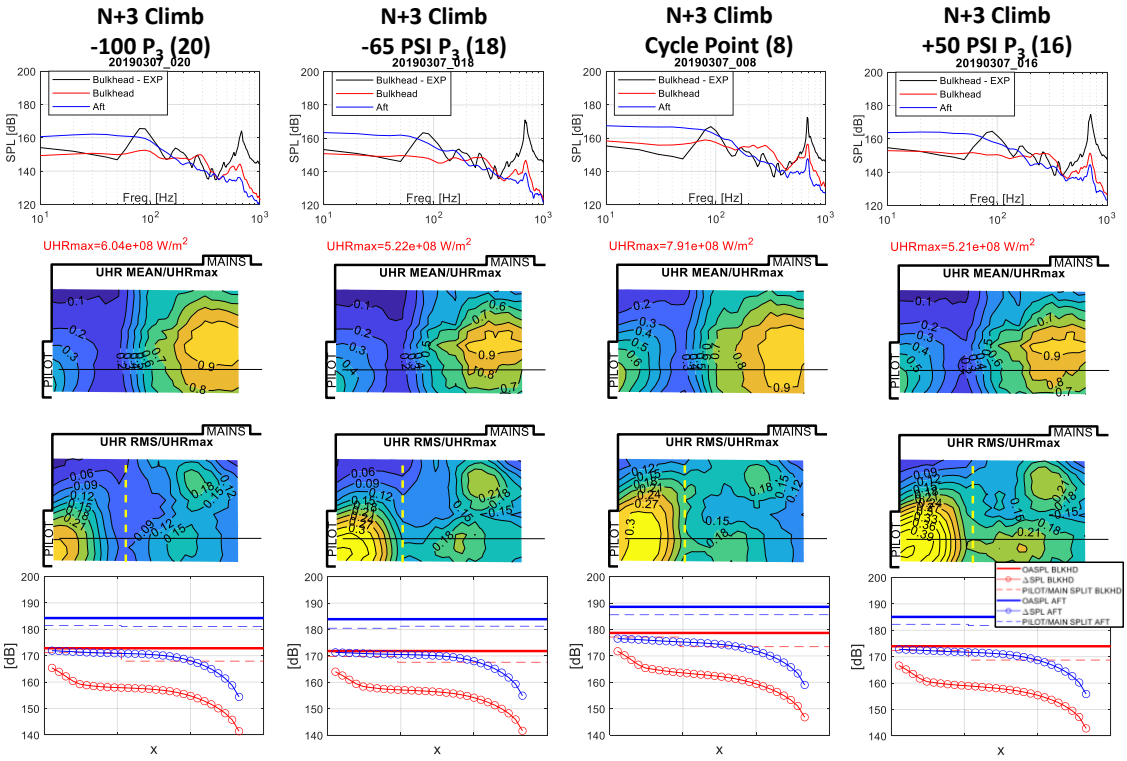

Figure 39c. Direct-noise analysis for N+3 CLIMB P_3 sweep

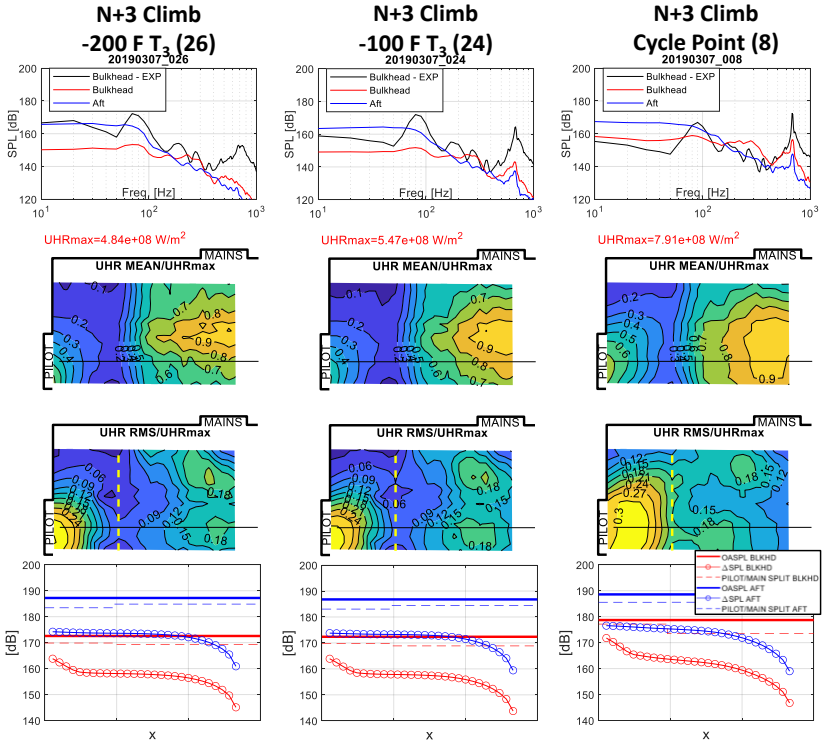

Figure 39d. Direct-noise analysis for N+3 CLIMB T_3 sweep

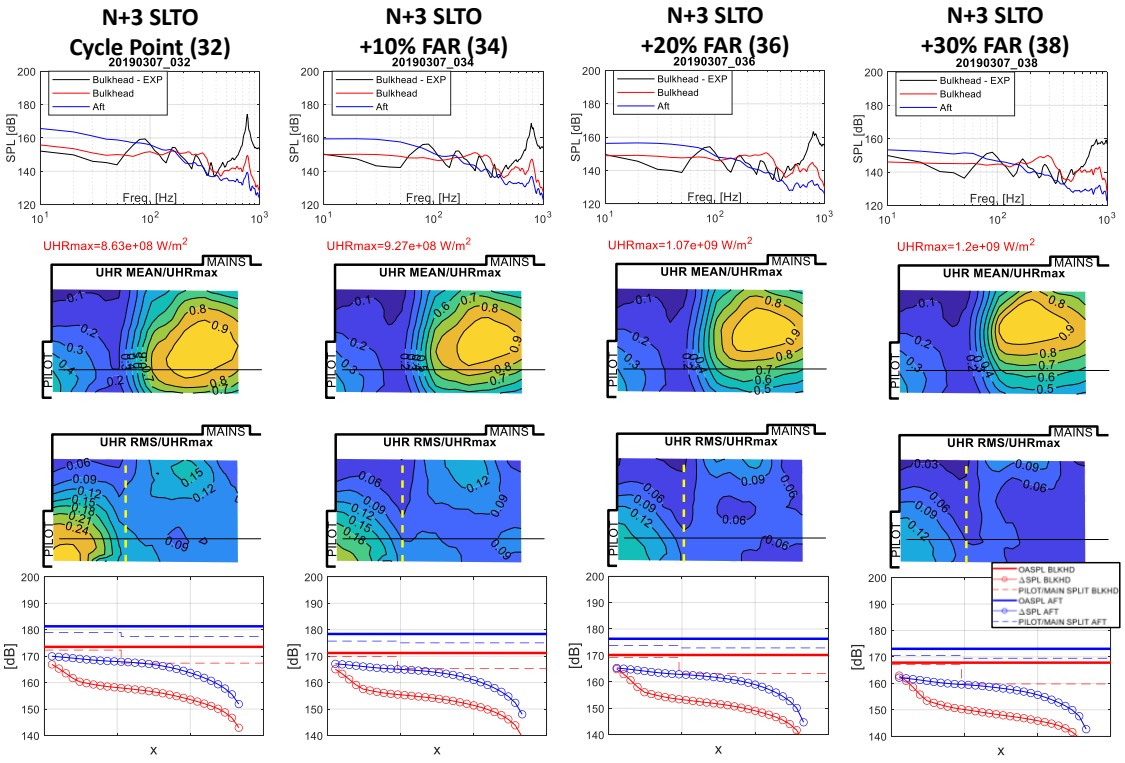

Figure 40a. Direct-noise analysis for N+3 SLTO FAR sweep

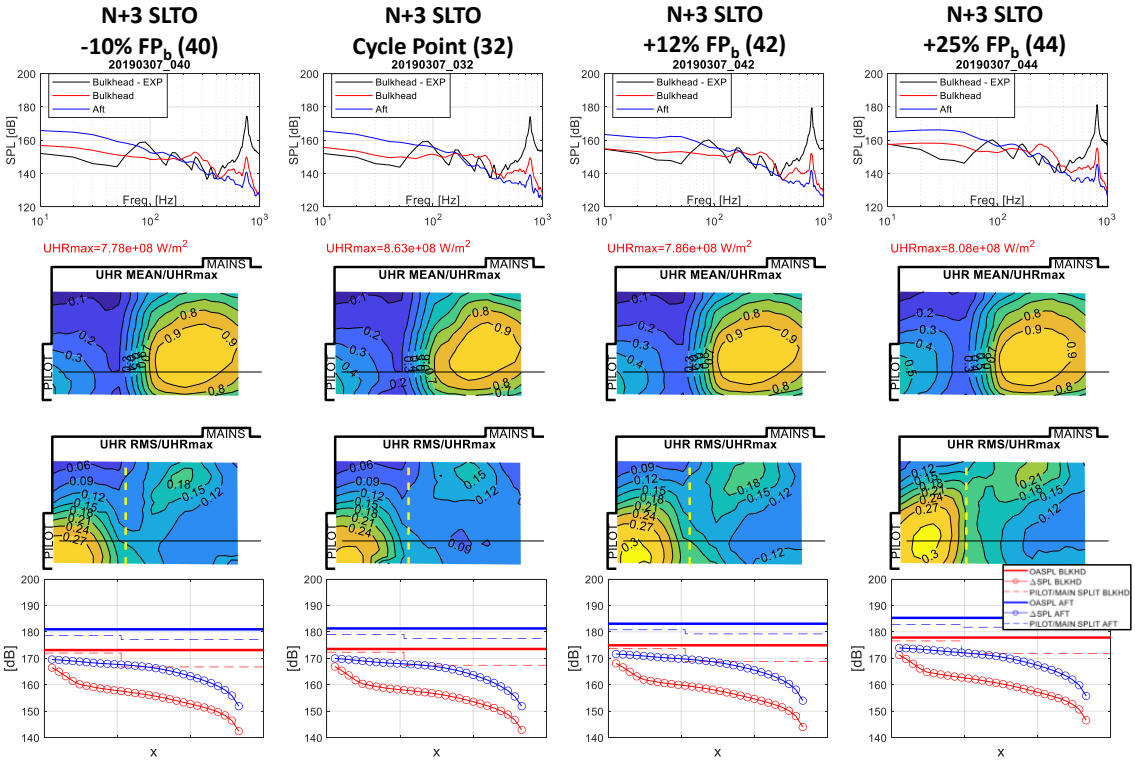

Figure 40b. Direct-noise analysis for N+3 SLTO FP_b sweep

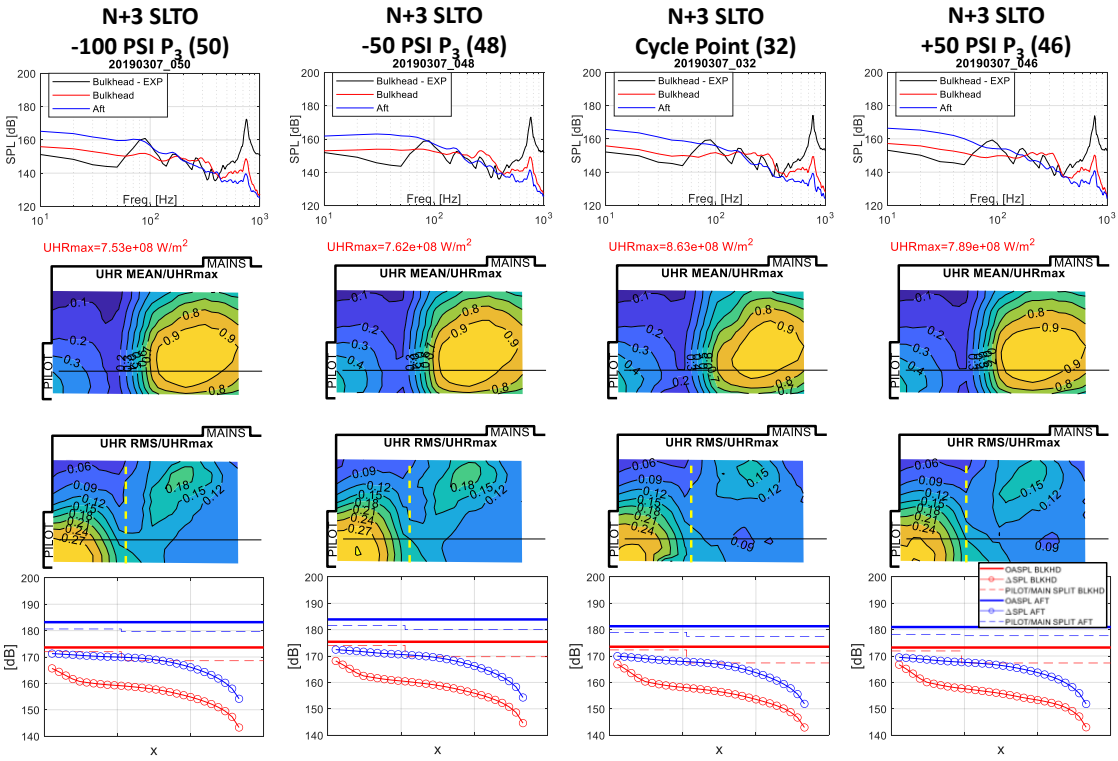

Figure 40c. Direct-noise analysis for N+3 SLTO P_3 sweep

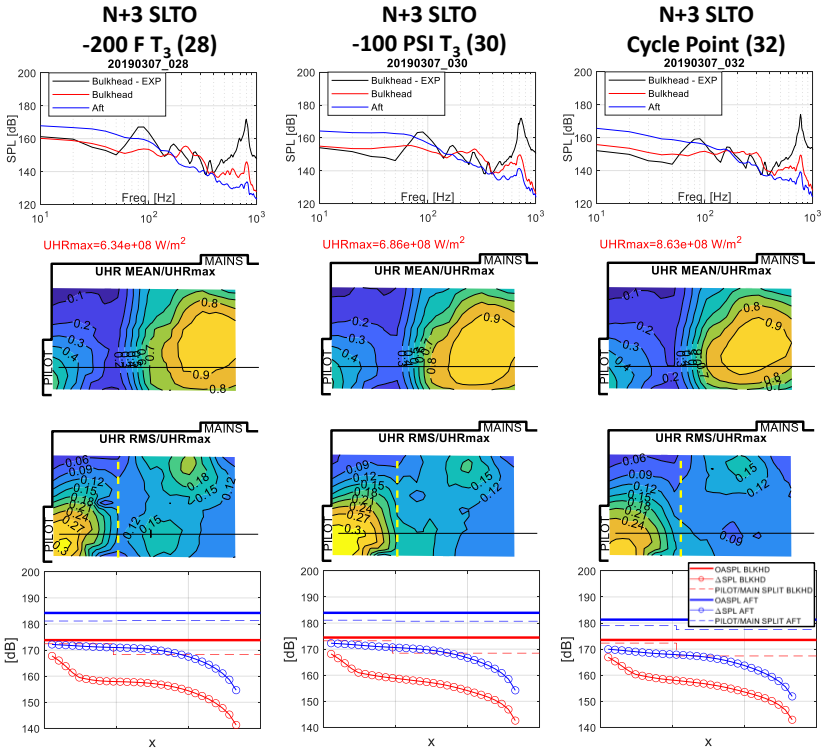

Figure 40d. Direct-noise analysis for N+3 SLTO T_3 sweep

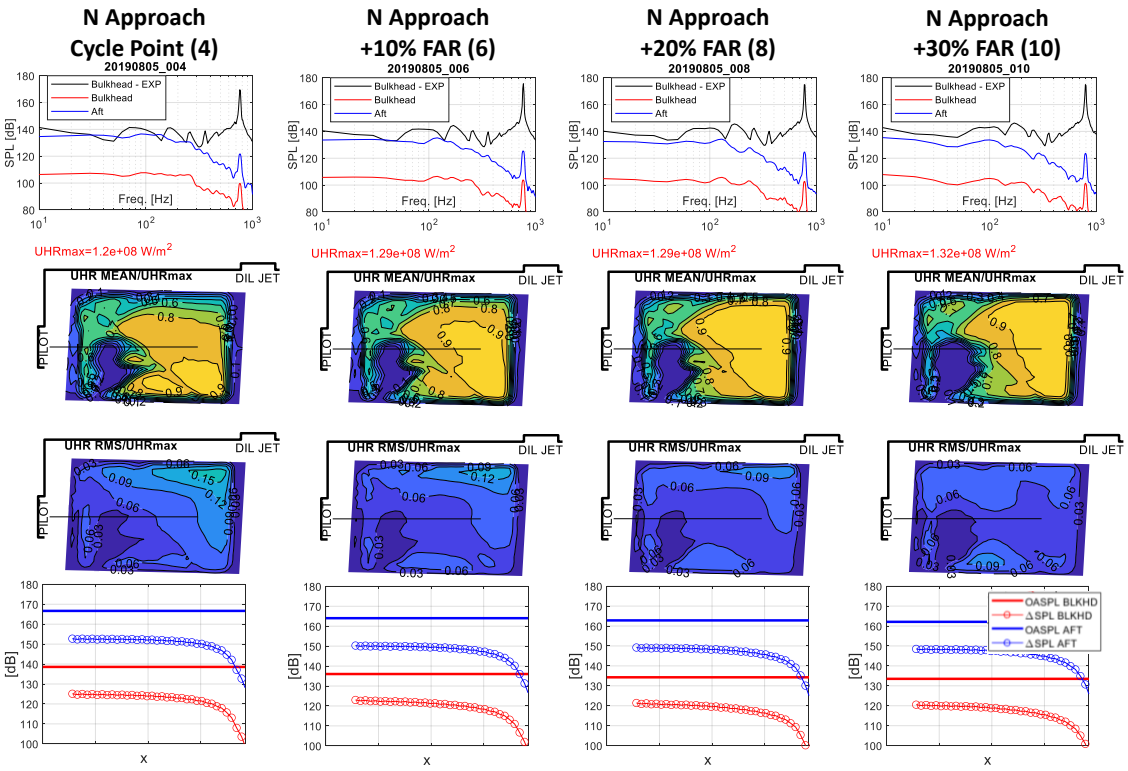

Figure 41a. Direct-noise analysis for N APPROACH FAR sweep

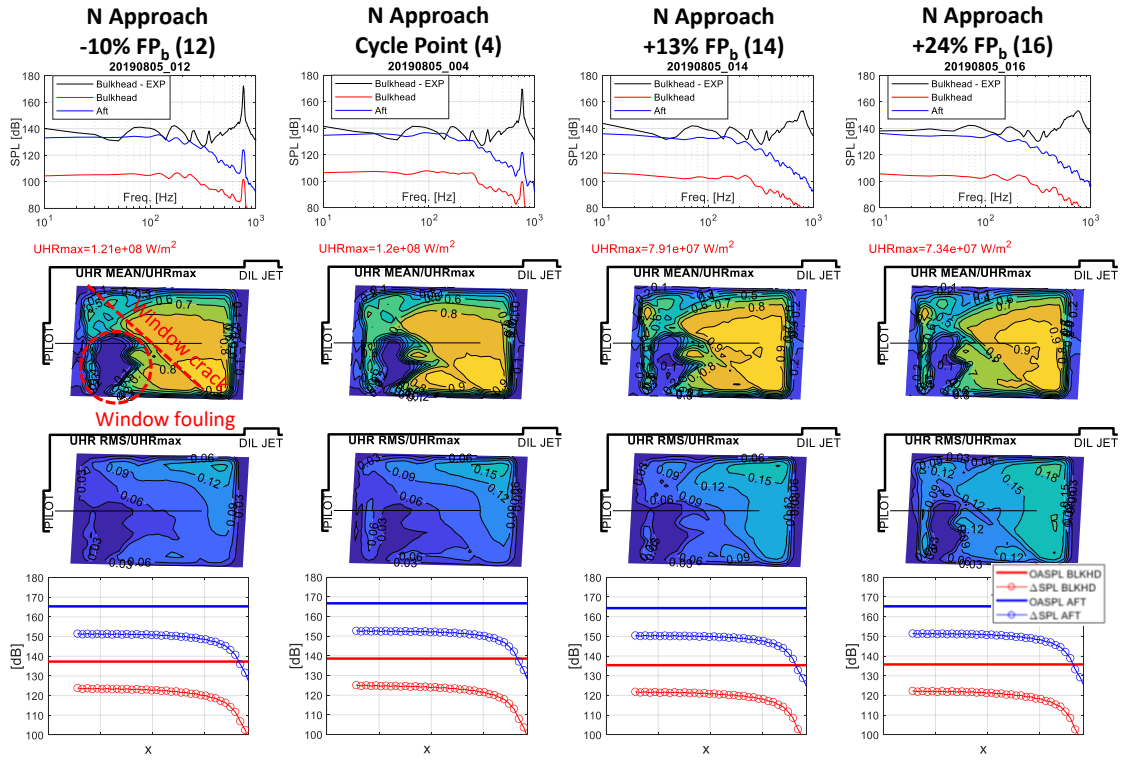

Figure 41b. Direct-noise analysis for N APPROACH FP_b sweep

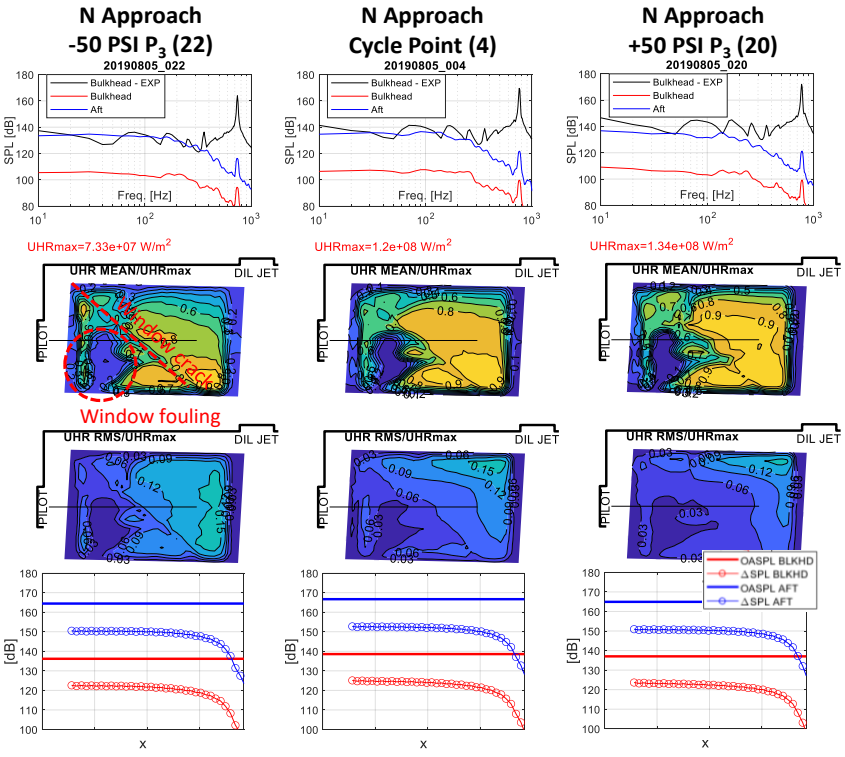

Figure 41c. Direct-noise analysis for N APPROACH P_3 sweep

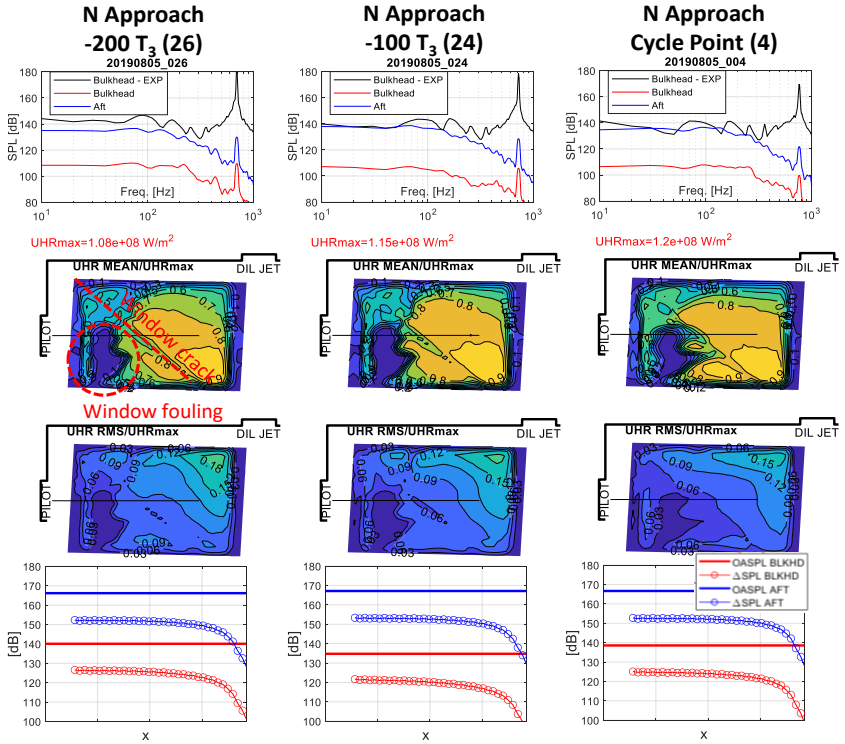

Figure 41d. Direct-noise analysis for N APPROACH T_3 sweep

Multi-Point Statistical Analysis

Two-point space-time correlation analysis was applied to the UHR field data to extract combustion length scales and convection features. A program was written to interactively allow the user to choose a field point for the reference correlation location (x_o,y_o) which then computes the following space correlation of a sequence of time steps (τ).

$$R(x_0, y_0, x, y, \tau) = \frac{\overline{q(x_0,y_0,t)q(x,y,t+\tau)}}{\overline{q(x_0,y_0,t)^2}}$$

The user than can interactively choose the propagation angle that best captures the movement of the coherent structure. From that the convection speed is displayed as is the compute integral combustion length scales from the zero-time delay field. It was found that selecting the reference location at an RMS peak resulted in a "well-centered" correlation (i.e., the correlation peak was coincident with the reference location and contours of lower values where symmetric around that point).

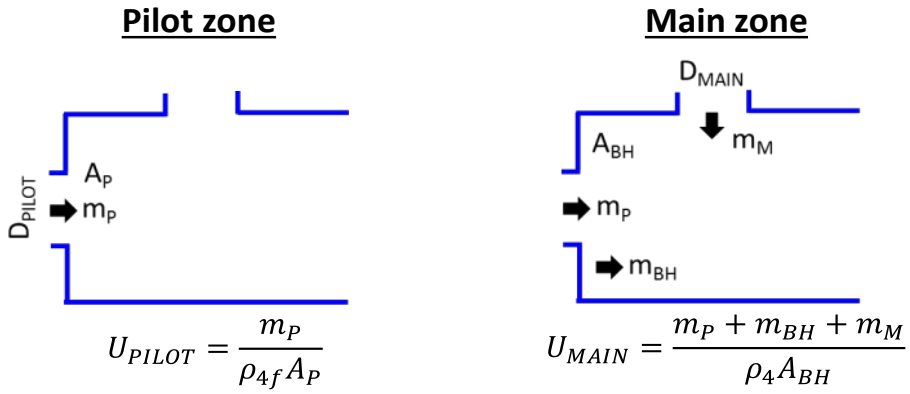

Figure 42. Length and velocity scales for pilot and main combustion zones

Figure 42 defines the reference velocity (U_{REF}) and length (D_{REF}) used for the pilot and main combustion zones to normalize velocity and length scales. In the pilot combustion zone, the exit diameter of the pilot mixer was used for D_{REF} and the mass flow rate through the mixer divided by combustor front-end density (ρ_{4f}) and pilot exit area (A_P) to compute U_{REF}. In the main combustion zone, the reference length was the exit diameter main mixer. The reference velocity in this zone included upstream pilot and bulkhead flows combined with the mains flow divided by the area of the bulkhead (A_{BH}) and combustor density after the dilution jets (ρ_4), as illustrated in the figure.

Figures 43a and b show examples for the N+3 climb condition at a P_3 excursion. Looking at Fig. 43a (pilot region), in the top row, the left and middle contour plots are of the mean and RMS UHR. The circular symbol with an "x" shows the selected reference location (x_o,y_o). The bottom three rows show the spatial distribution of the correlation function at nine time delays ($\tau = 0 - 0.8\,ms$). Also shown is the chosen convection direction (found by trial and error). In the top right of Fig.43a, the line plots of the correlation in the direction of the convection

direction are given for five time steps (*0 ms* = black, *0.1 ms* = red, *0.2 ms* = blue, *0.3 ms* = magenta, *0.4 ms* = cyan). The second and third time step (*0.1 and 0.2 ms*) were used to compute an average convection speed, $1.13U_{REF}$. Also given is the integral combustion scale in the direction of the convection direction, $0.787D_{REF}$. In the main region (Fig. 43b) the correlation plots are not a clear in part due to limited imaging window size which requires an extrapolation of the zero time correlation to estimate the combustion length scale ($0.683D_{REF}$). Characterizing the main combustion zone is also difficult since the structures don't appear to move in a single direction, but instead are stretch both downstream and vertically downward.

It should also be pointed out that the emergence of coherent structures at $\tau = 0.5 - 0.6\ ms$ for the pilot (Fig. 43a) and the high correlation of the main region with the pilot (Fig. 43b) suggest a strong, periodic interaction. The period is approximately *0.7 ms* corresponding to ~1.4 kHz (possibly related to the full wavelength longitudinal mode from bulkhead to choke).

N+3 Climb and SLTO

Figures 44a, b, c, and d plot the convection angle, convective speed and integral length scale of the UHR structures versus the combustion parameter sweeps *FAR*, FP_b, P_3, and T_3, respectively. The upper portion of each plot displays the pilot zone (filled red squares = climb; filled blue triangles = SLTO) and the lower portion displays the main zone (open red squares = climb; open blue triangles = SLTO). The numbers in each symbol identifies the point number of the test. Referring to the corresponding appendix Tables A3 and A4 (sorted by configuration and operating condition), the exact operating conditions can be identified.

The trending of the UHR structure parameters versus the combustion parameters is a somewhat scattered. The *FAR* sweep shows the most systematic variations in the UHR structure parameters (Fig. 44a). For the pilot zone, the convection angle decreases with increasing *FAR* as the direction becomes more directly downstream and the length scale decreases modestly from $0.75\text{-}0.55D_{PILOT}$. The convection speed is invariant near the reference velocity, U_{PILOT}.

For the main zone, the convection angle decreases with increasing *FAR* becoming more downward vertically, the convection speed slows from $1.0\text{-}0.5U_{MAIN}$ and the length scale reduces from $0.6\text{-}0.2D_{MAIN}$. Based on these observation, it appears that as the *FAR* is increases, the main combustion zone is increasingly entrained upstream into the pilot zone, likely due to a strengthening center recirculation bubble of the pilot zone.

Figures 45a and b plot all the above N+3 climb and SLTO data in legacy scaling law parameters of Matthews-Rekos and ANOPP, respectively.

N+3 and N Approach

For the approach conditions, the two-point analysis was adjusted to the features displayed in the UHR field, specifically, there were two distinct high RMS regions in the field, one in the upper region of the combustor and a second in the lower region. Hence, the UHR structures were separately identified for each region. Figures 46a and b show a typical correlation analysis in the upper and lower zones, respectively for N and N+3 approach. Unlike the N+3 climb and SLTO, there is no periodic feature suggested at the later time delays.

Figures 47a, b, c, and d plot the convective angle, convective speed and integral length scale of the UHR structures versus the combustion parameter sweeps *FAR*, FP_b, P_3, and T_3, respectively, for the N and N+3 approach conditions. The upper portion of each plot displays the upper region (filled red circles = N configuration; filled blue circles = N+3 configuration) and the lower portion displays the lower region (open red circles = N configuration; open blue circles = N+3 configuration). Again, the numbers in each symbol, identifies the point number of the test. The reference length and velocity are the same as the pilot zone of the N+3 configuration (left side of Fig. 42).

For both the N and N+3 configurations, the convective angle, convective velocity and integral length scales are very similar to each other for most conditions. In one sense, this result is not surprise since the burner configuration is very similar (other than the different arrangement of downstream traverse jets). However, given the very different looking UHR field (discussed in previous section), it is somewhat surprising. Also, worth pointing out is the low value of the convective speed (less than $0.5U_{REF}$) compared with the convective speed for the N+3 climb and SLTO pilot zone ($\sim 1U_{REF}$). These different values are due to the different locations of the UHR structures. For climb and SLTO, they are close to the mixer whereas for approach, they are further downstream. For the latter case, a more appropriate velocity reference could arguably include the bulkhead cooling and the area be the burner cross-sectional area (instead of the swirler exit area).

Figures 48a and b plot all the above N+3 and N approach data in legacy scaling law parameters of Matthews-Rekos and ANOPP, respectively.

In summary, a 2-pt UHR correlation analysis has been performed on the N+3 combustor (all operating points) and a limited number of operating points for the N combustor that have identified several statistic characterizations that may be useful for high-fidelity simulations. It also has identified a periodic interaction between the pilot and mains for the N+3 configuration.

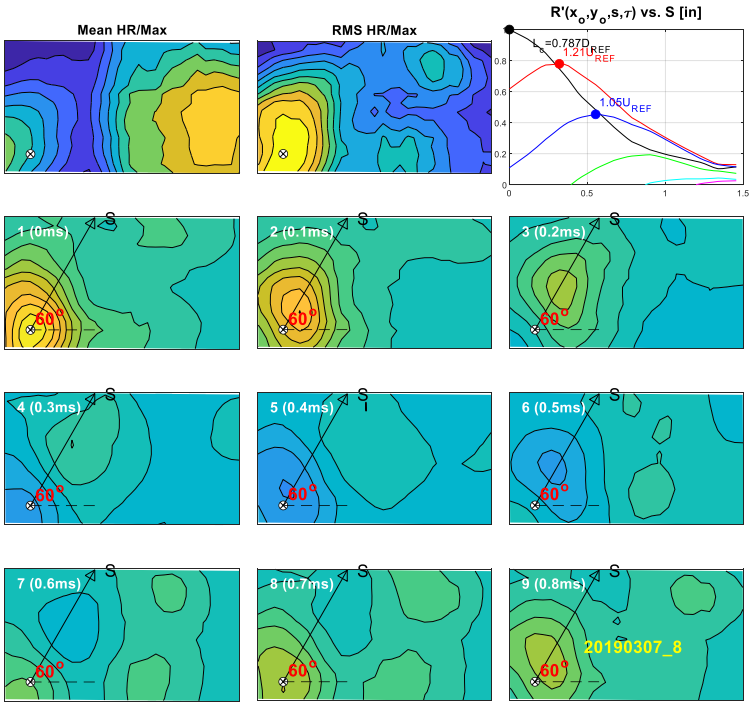

Figure 43a. Time-space UHR correlation N+3 Climb cycle point (pilot combustion zone)

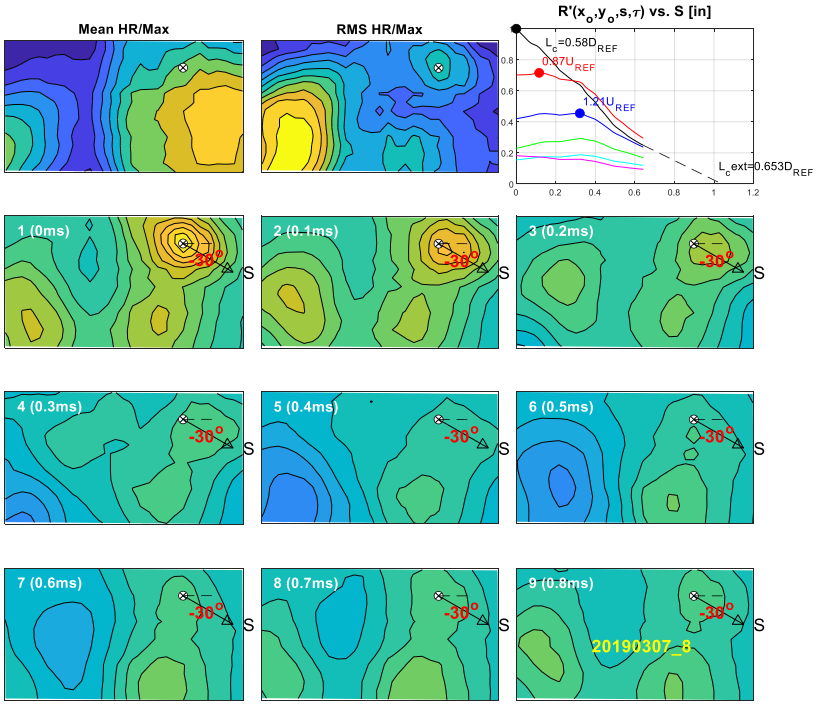

Figure 43b. Time-space UHR correlation N+3 Climb cycle point (main combustion zone)

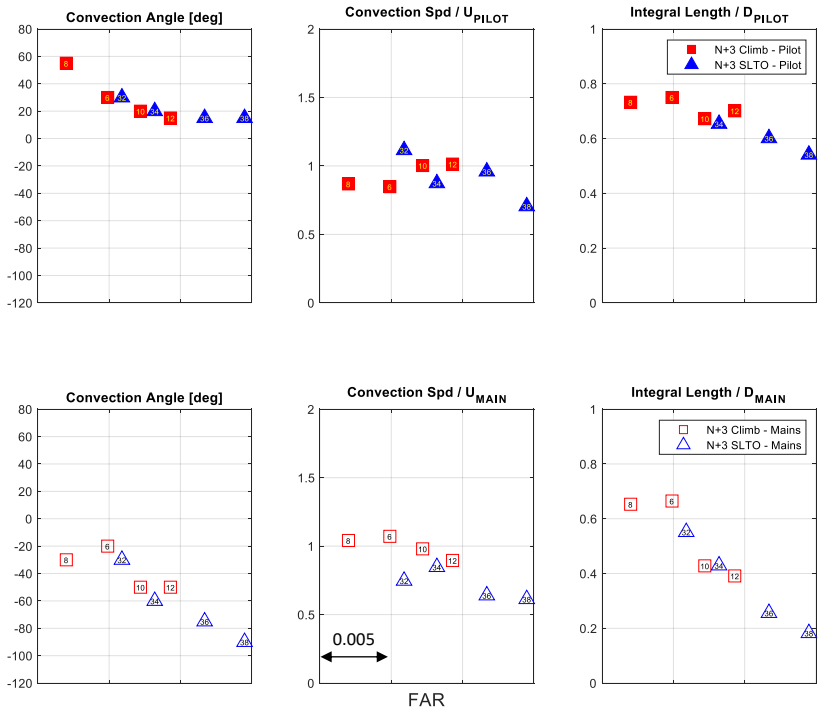

Figure 44a. Multi-point correlation results for N+3 CLIMB and SLTO versus FAR

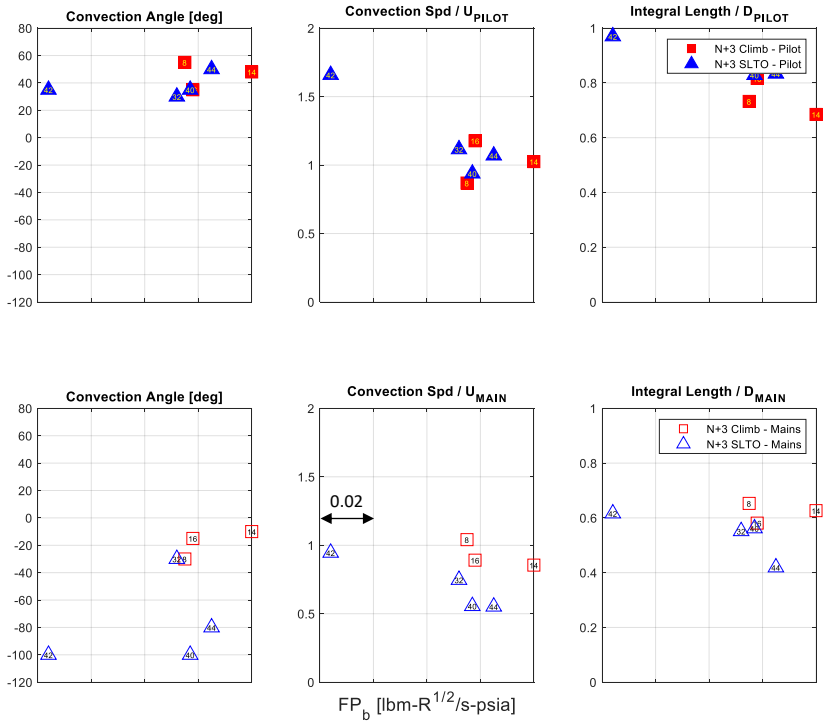

Figure 44b. Multi-point correlation results for N+3 CLIMB and SLTO versus FP_b

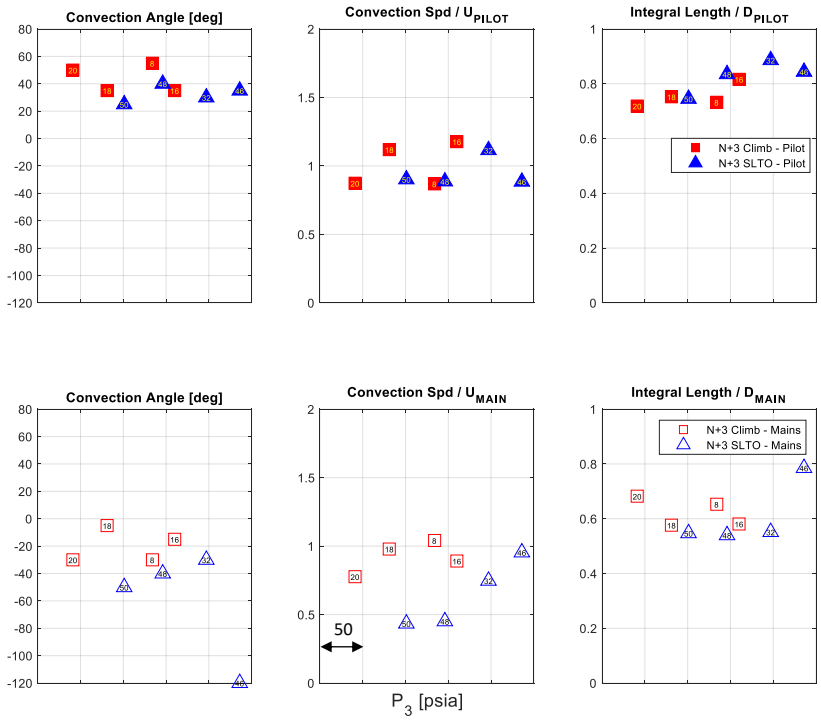

Figure 44c. Multi-point correlation results for N+3 CLIMB and SLTO versus P_3

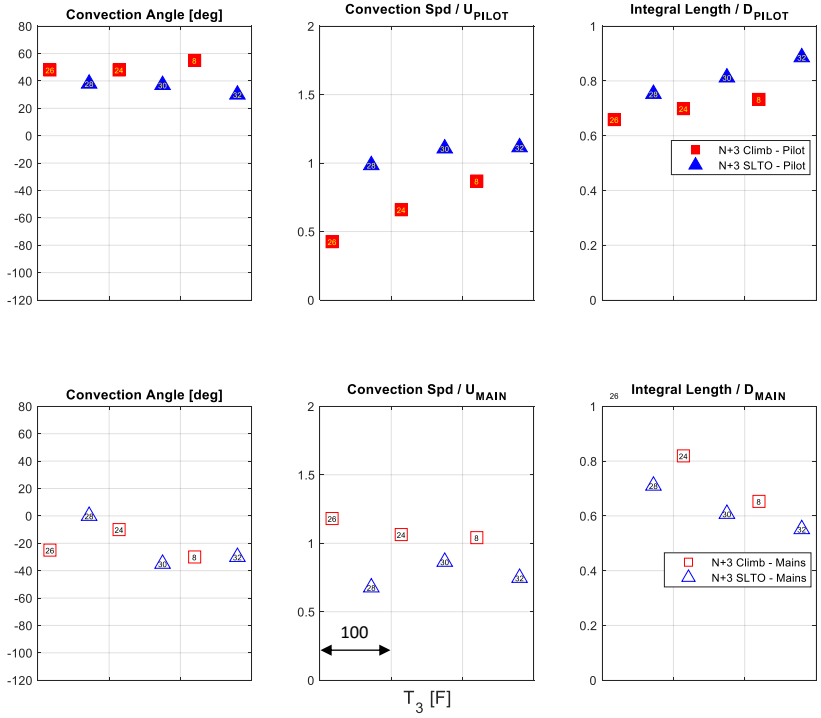

Figure 44d. Multi-point correlation results for N+3 CLIMB and SLTO versus T_3

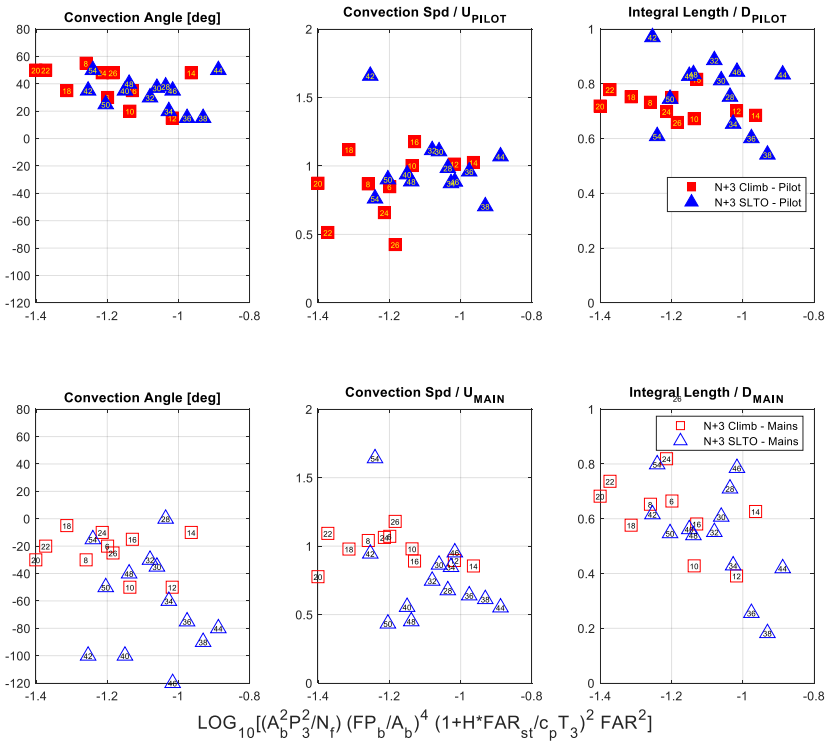

Figure 45a. Multi-point correlation results for N+3 CLIMB and SLTO versus M-R scaling

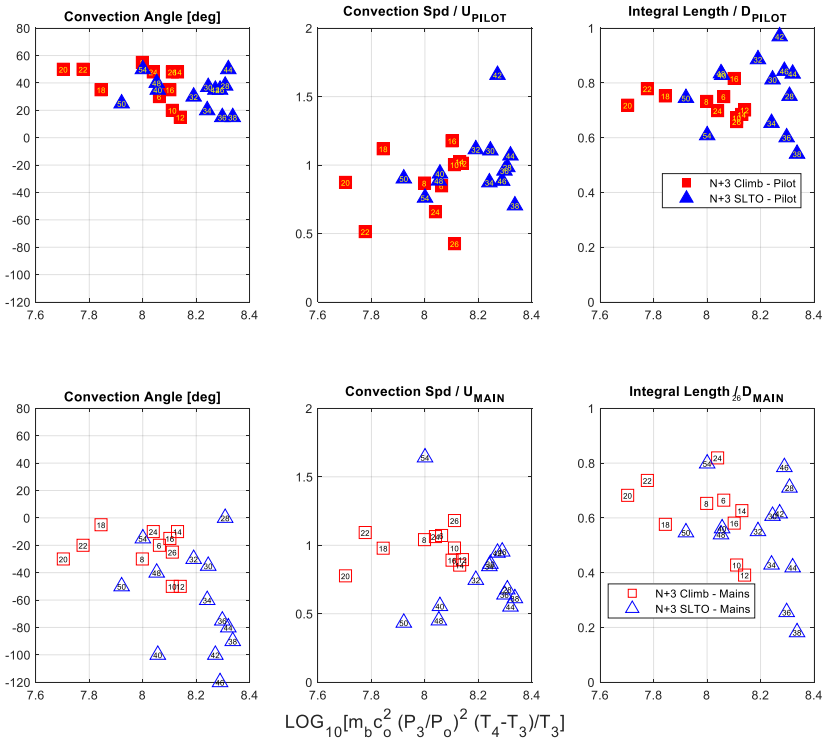

Figure 45b. Multi-point correlation results for N+3 CLIMB and SLTO versus ANOPP scaling

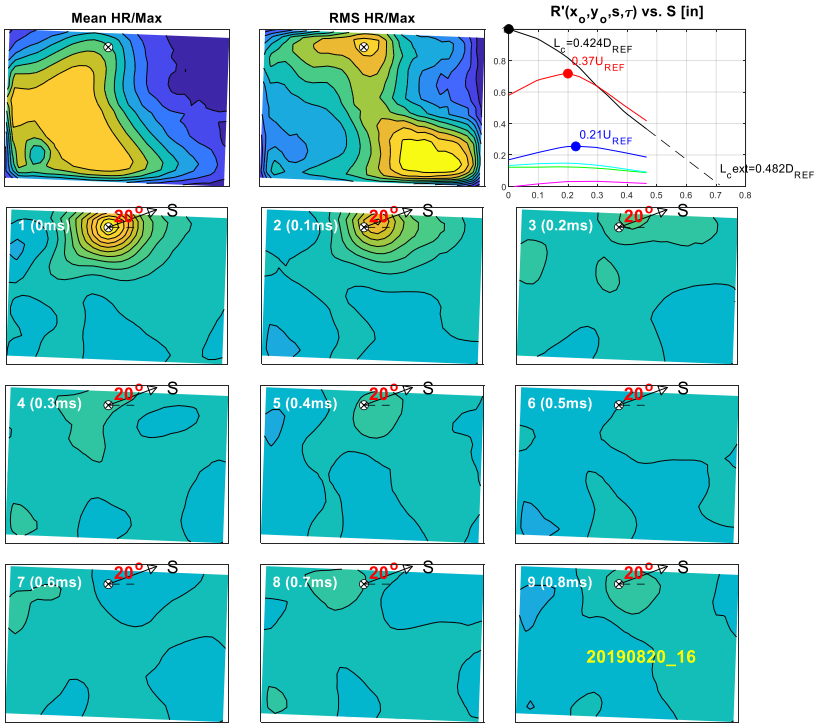

Figure 46a. Time-space UHR correlation N+3 Approach -10% FP_b excursion (upper combustion zone)

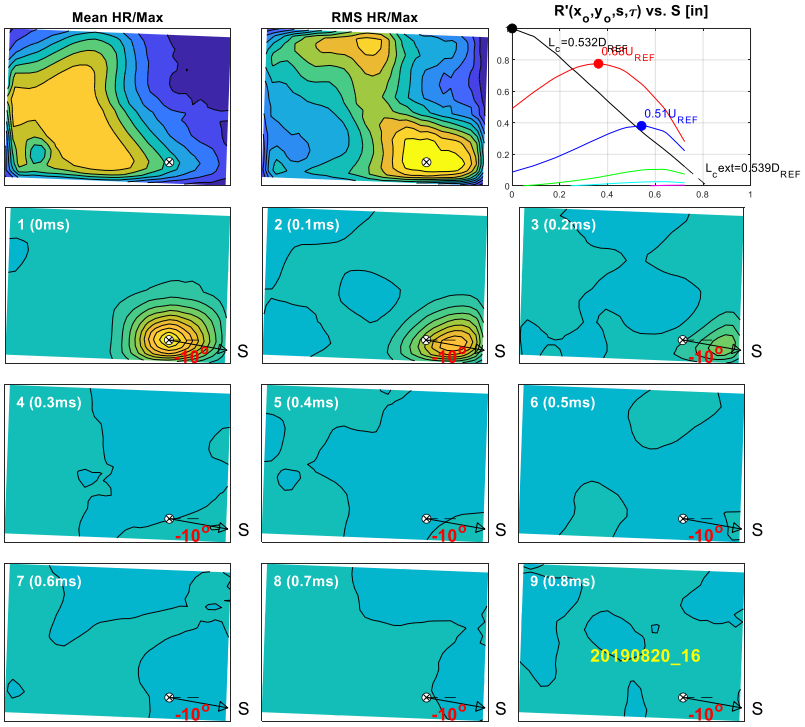

Figure 46b. Time-space UHR correlation N+3 Approach -10% FP_b excursion (lower combustion zone)

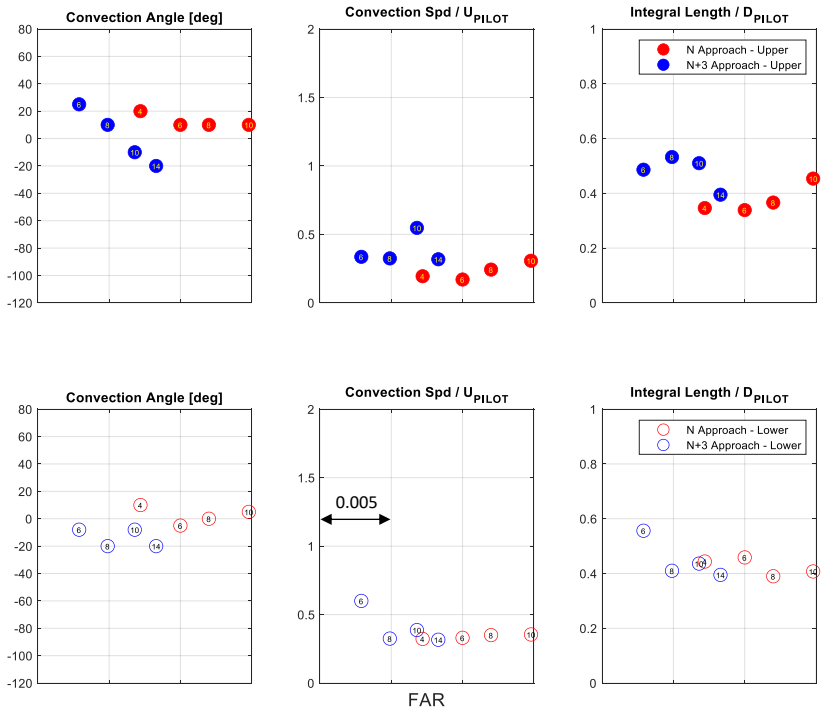

Figure 47a. Multi-point correlation results for N and N+3 APPROACH versus FAR

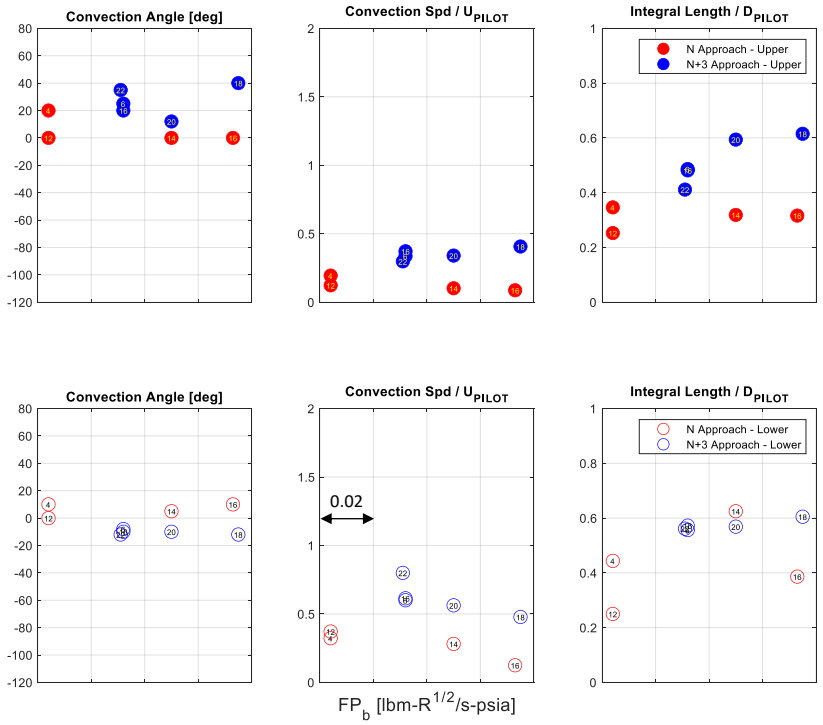

Figure 47b. Multi-point correlation results for N and N+3 APPROACH versus FP_b

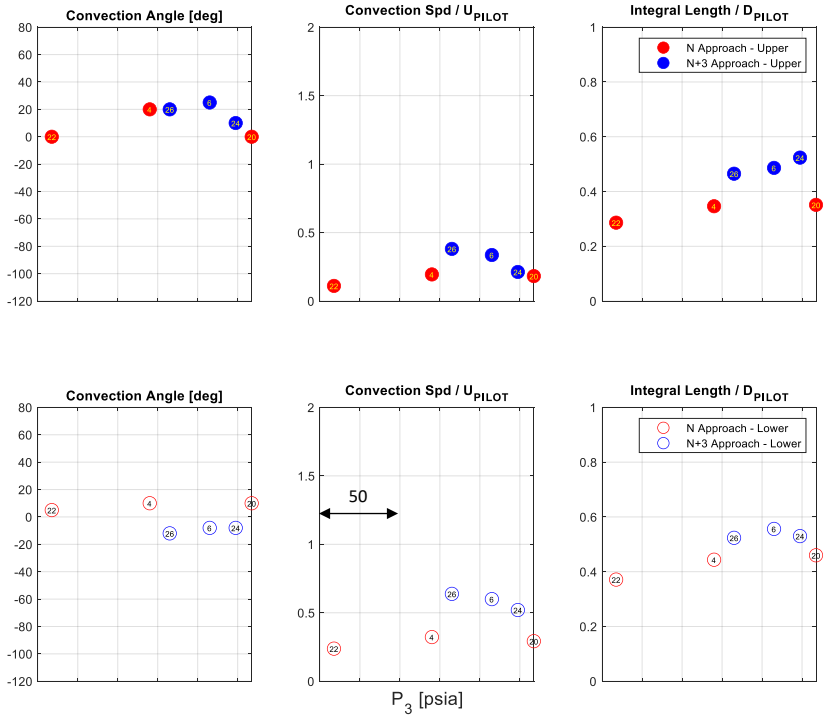

Figure 47c. Multi-point correlation results for N and N+3 APPROACH versus P_3

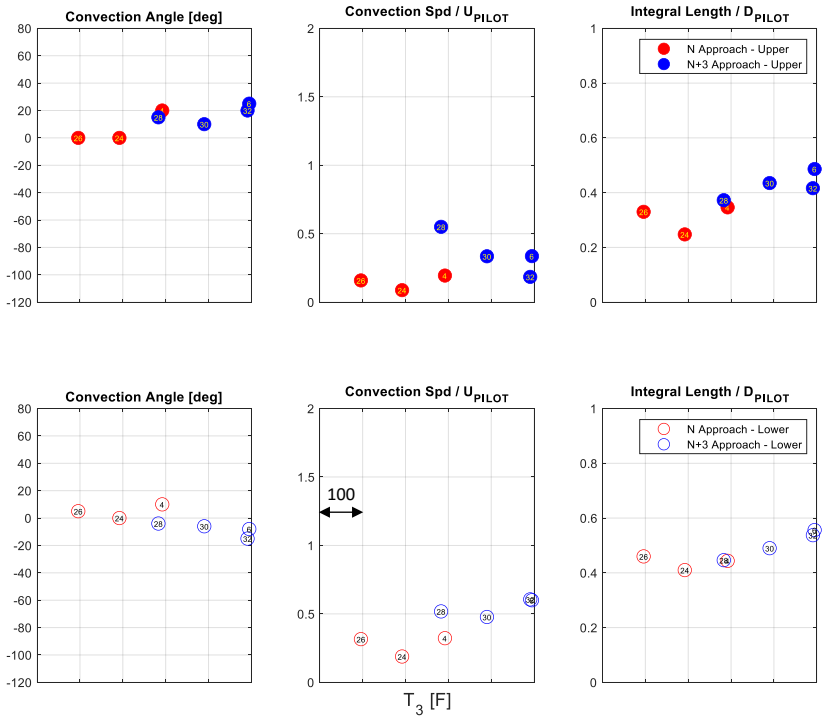

Figure 47d. Multi-point correlation results for N and N+3 APPROACH versus T_3

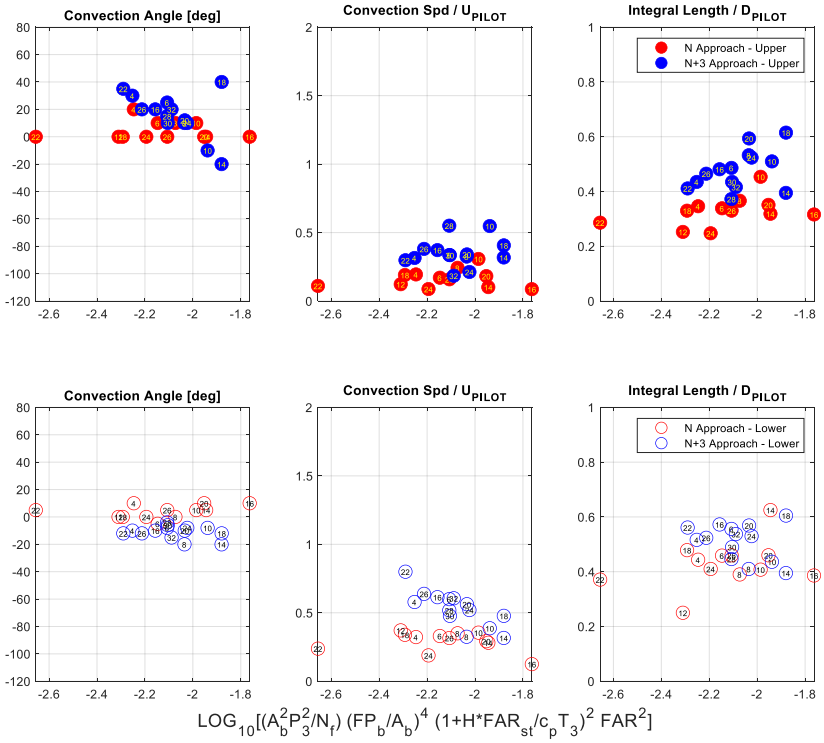

Figure 48a. Multi-point correlation results for N and N+3 APPROACH versus MR scaling

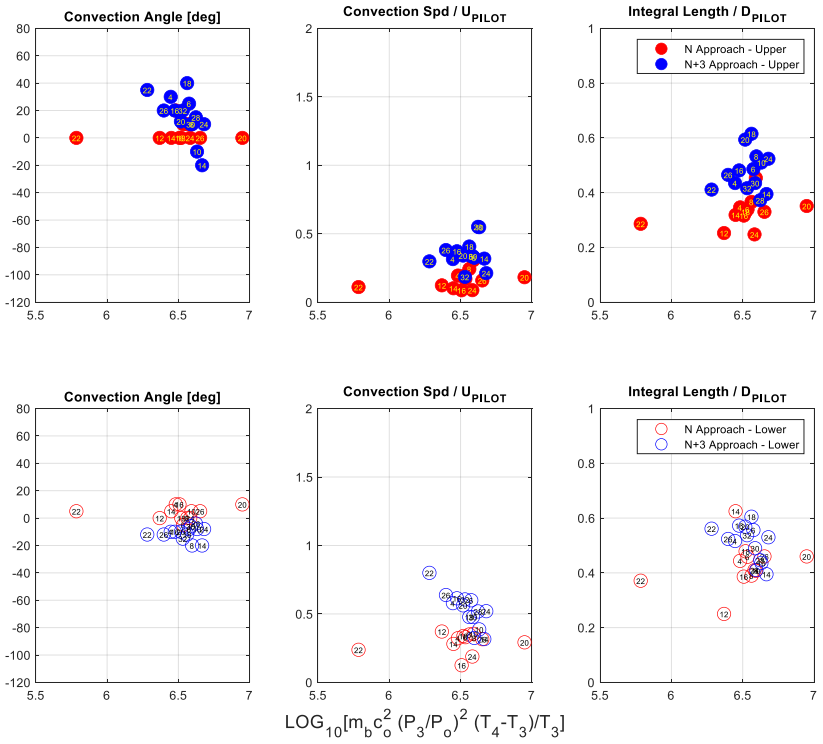

Figure 48b. Multi-point correlation results for N and N+3 APPROACH versus ANOPP scaling

Dual-TC Measurements

Time domain unsteady temperature measurements were obtained at the combustor exit with a TDLAS (Tunable Diode Laser Absorption Spectroscopy) approach to evaluate this technique at high pressure conditions for the purpose of determining its usefulness in future studies of indirect noise. For comparison, a dual-TC probe was used to obtain frequency domain temperature measurements at the same axial plane.

A custom instrumentation flange (first shown in Fig. 5) was fabricated to mount both the TDLAS sight tubes and the dual-TC probe. Figure 49 shows the flange location in the test rig, located between combustion section and the VRASC/choke section and had a trapezoidal flow cross-section that matched the combustion section. Note, the instrumentation flange was thicker (1.5 in) than the normal instrumentation flange (0.5 in) that existed for UHR and dynamic pressure measurements. Figure 50 shows the flange with the TDLAS tubes installed and, notionally, the location of the dual-TC probe.

The design of the dual-TC is shown in Fig. 51 for a similar probe which was developed by Honeywell under NASA funding **[17]**. The dual-TC concept consists of two co-located thermocouple junctions with different response time constants. In the figure, there is a 0.004-inch diameter and a 0.010-inch diameter junction. The actual probe used in this study had 0.003- and 0.010-inch junctions. Both junctions were of type B. The basic approach is to use the cross-correlation of the two signals to derive a corrected power spectrum estimate of the actual temperature fluctuation as described by Strahle and Muthukrishnan **[18]**. Assuming a first-order, linear differential response of the thermocouple signal (with time constant τ) to the actual temperature fluctuation, the true temperature signal is given by

$$X \approx \frac{Y}{(1 + i\omega\tau)}$$

where Y is the Fourier transform of the thermocouple signal and X is the Fourier transform of the true temperature signal. The time constant τ is derived from cross-correlation (R) of the two thermocouple signals (with different time constants). As shown in **[18]**, the peak in the imaginary part of the correlation is the inverse of the faster time constant (i.e., $f_\tau = 1/\tau$) and the asymptotic value of the real part is the ratio of the faster and slower time constants. For the current testing, Fig. 52 shows a typical correlation result together with the coherence (top) which indicates good signal to noise. The cross-correlation indicates a time constant of about 42 ms for the smaller junction and a time-constant ratio of about 6. Since the thermal response of the junction is proportional to the 1.5 power of the diameter, the expected ratio is $(.010/.003)^{1.5} = 6.1$, which is consistent with the data.

Figure 53 shows the dual-TC results for a range of pressures from 100 to 200 psia for the N+3 configuration, pilot only operating condition. This data is from the initial TDLAS/dual-TC arrangement shown on the left side of Fig. 54. The left plots of Fig. 53 show the time domain of the two thermocouples (red is the smaller junction; blue is the larger junction) normalized by the adiabatic flame temperature (T_4). The data shows good agreement with T_4, independent of operating pressure. The corresponding raw and corrected spectra (in term of the deviation from

mean: $(T-\bar{T})/\bar{T}$ where $\bar{T}$ is the mean measured temperature) are shown on the right side of Fig. 53. The results indicate the highest fluctuations occur around 2 Hz and the fluctuations are relatively flat between 10 and 200 Hz.

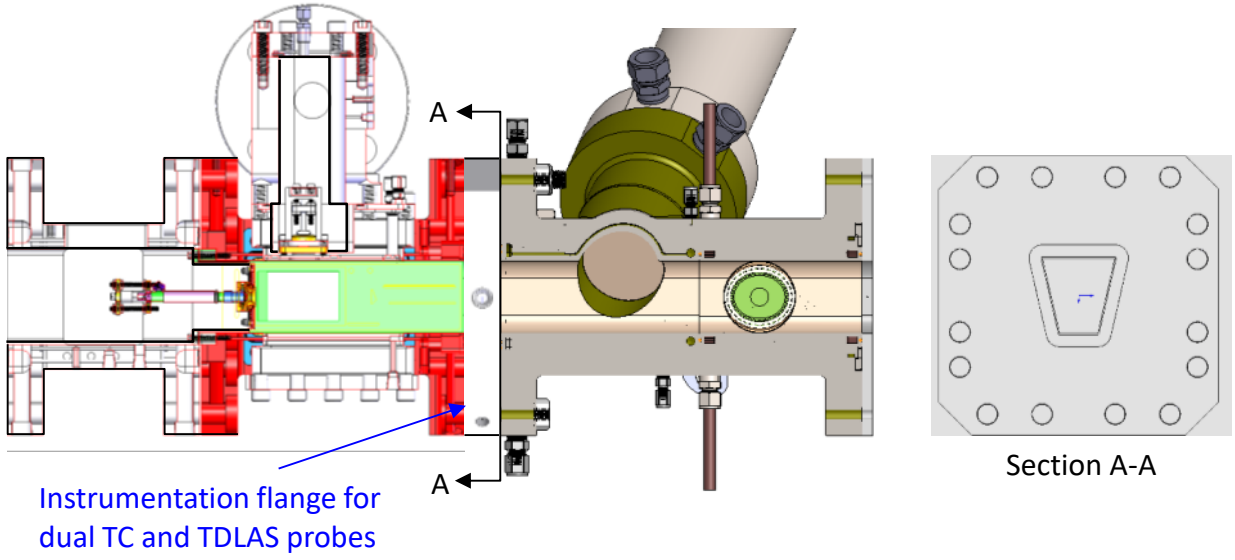

Figure 49. Test rig with instrumentation flange

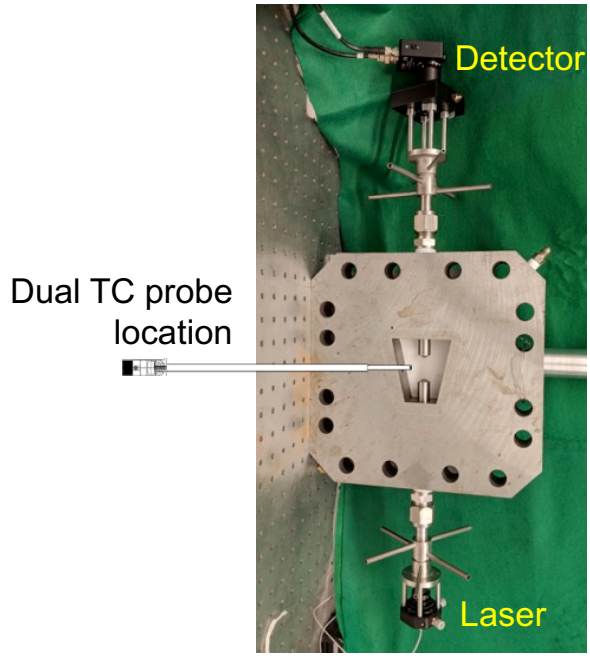

Figure 50. TDLAS instrumentation flange assembled shown with dual-TC location

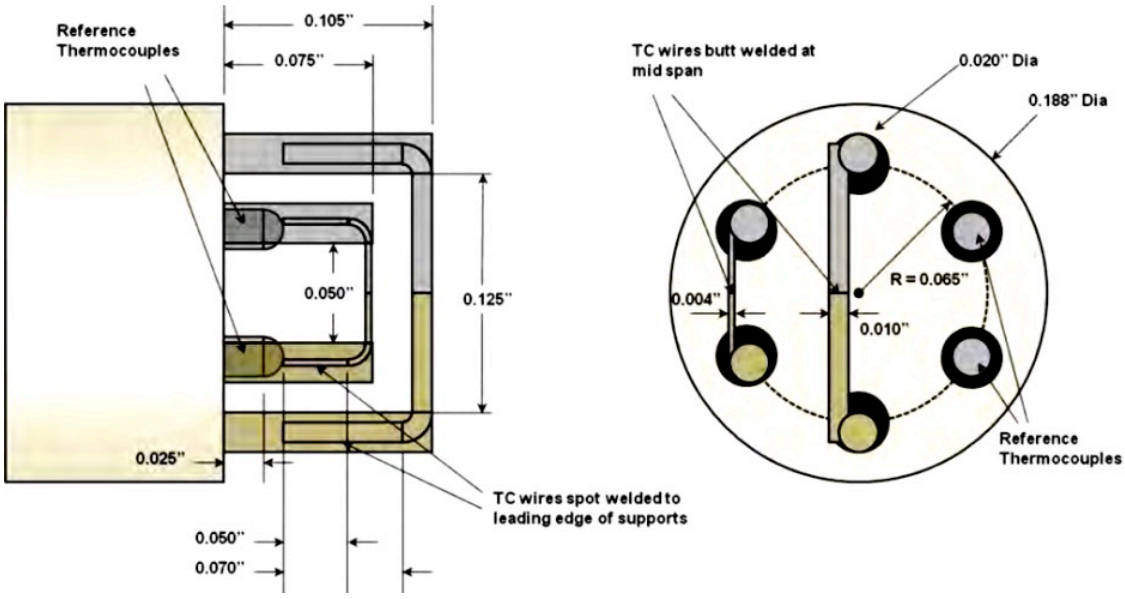

Figure 51. Dual-TC probe arrangement

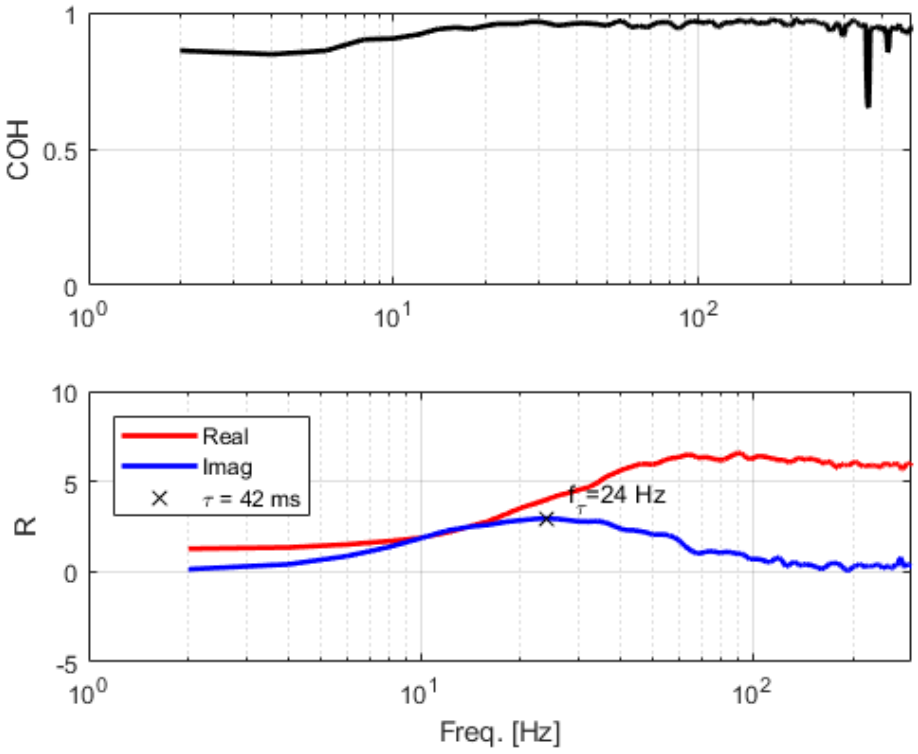

Figure 52. Typical dual-TC probe cross-correlation analysis

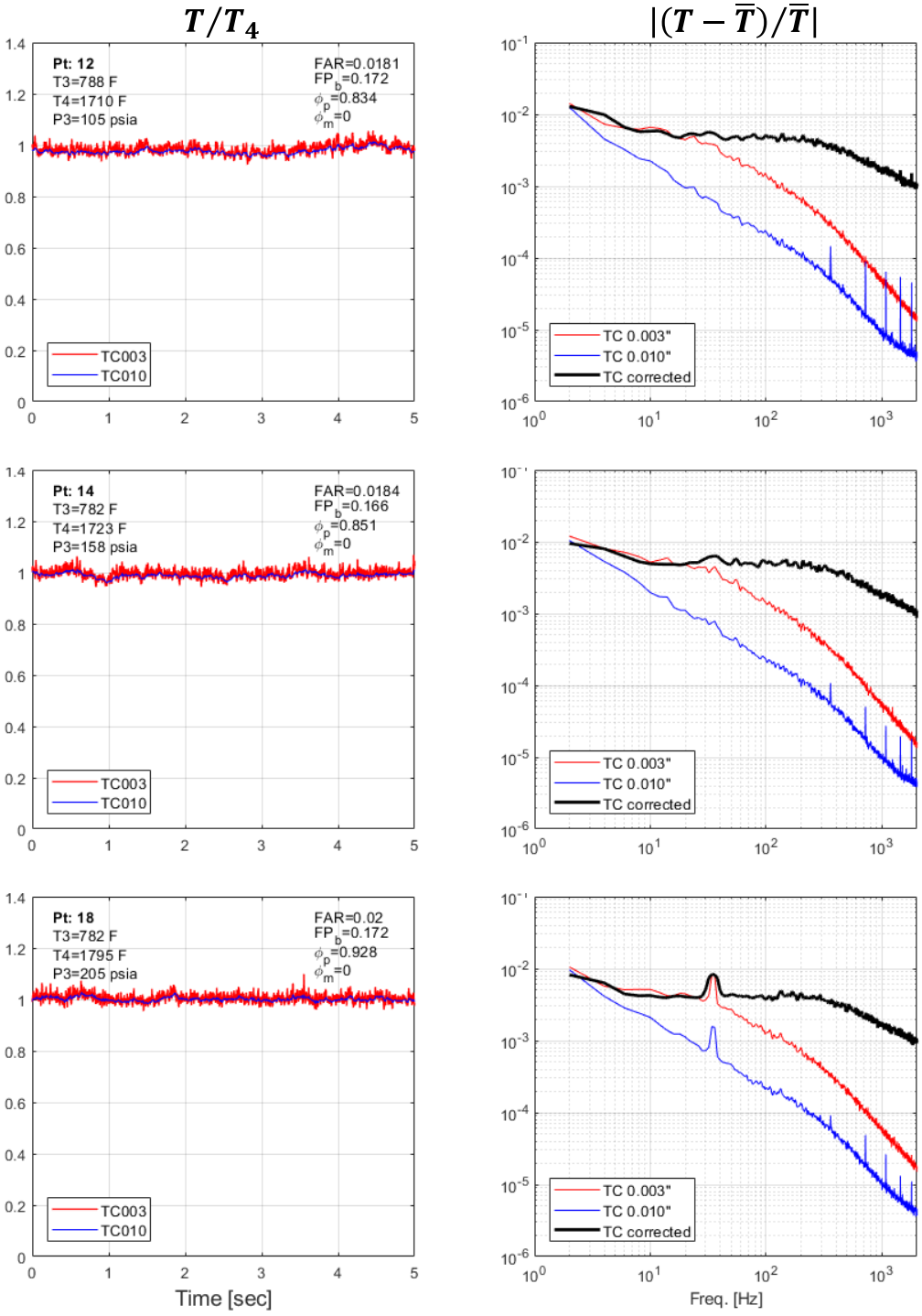

Figure 53. Typical dual-TC probe results over range of pressure

TDLAS Measurements

Characterization of combustion induced temperature fluctuations aft of the combustor was attempted using tunable diode laser absorption spectroscopy (TDLAS). This optical, non-intrusive technique provides a high frequency (1-50 kHz) temperature measurement by targeting water absorption in the exhaust gas. Efforts in the current work focused on integration of the TDLAS system into an instrumentation flange that was easily incorporated into the existing rig hardware, as well as demonstration testing and comparisons with the dual-TC approach.

TDLAS Hardware

The TDLAS technique is inherently a line-of-sight averaged measurement and therefore requires two points of optical access for laser input (pitch) and exit (catch). To achieve the required optical access in the complex combustion rig, an instrumentation flange was designed, fabricated and installed downstream of the combustor. The flange houses water-cooled sight tubes, as show in Fig. 50, which provides the necessary line-of-sight optical access. In addition, the tube allows variation in both the relative position and length of the absorption path for the temperature measurement. To reduce the overall complexity of the sight tube design, the windows are mounted on the cold end of the tube, exterior to the rig, which dramatically reduces the complexity of the window seal design and improves window reliability. An open-loop, nitrogen purge is integrated into the design to eliminate any influence of water absorption along the length of the sight tube internal volume. The overall instrumentation flange and sight tube design performed well in high temperature testing and no major drift in alignment was observed during hot/cold cycling. The only challenge encountered with the hardware was inaccuracy in the fabrication process that resulted in misalignment of the mounting flange on the sight tube with respect to tube centerline. This made the initial alignment process more difficult, but the clear aperture of the tubes was sufficient to overcome any major issue. Borescope images of the probe installed in the rig are presented in Fig. 54. Two different configurations have been tested with both a short pathlength of 1”, Fig. 54 (left) and a long pathlength of 2.5”, Fig. 54 (right). All results presented here correspond the long pathlength configuration.

TDLAS System Details

The TDLAS system used for this effort was configured for mid-Infrared (MIR) water absorption bands around 2.5 microns **[19]**. In general, MIR features provide 2-10x higher absorption line strengths than more commonly used transitions in the near-Infrared (NIR) around 1400nm. This higher signal strength improves sensor performance and potentially enables the use of shorter path lengths for improved spatial resolution. The only drawback of MIR probe development is the reduced number of off-the-shelf optical components and the need for more exotic optical materials (i.e. windows, lenses and fibers). Preliminary high temperature shakedown tests were performed in the rig near light-off conditions (T_3 = 600 F, P_3 = 70 psia), with the TDLAS system configured for scanned direct absorption measurements. While this configuration is the most straightforward absorption architecture, the shakedown tests quickly demonstrated the strong impact of gas-phase emission and beam steering resulting from rig vibrations and density gradients in the flow. While these non-resonant effects can be dealt with to some extend with direct absorption, the levels found in the current work were too high and additional mitigation strategies are required. As such, the TDLAS system was reconfigured for wavelength modulation spectroscopy (WMS) which is a phase-sensitive technique that is able to more readily reject lower frequency noise sources. Specifically, this technique combines high

frequency laser current modulation and a lock-in filter tuned to this frequency to reject noise outside the filter passband. This technique is particularly well-suited for harsh environment with non-resonant noise sources that can be much greater than the target absorption signals.

TDLAS temperature measurements typically employ the signal ratio from two absorption features. This ratio eliminates the direct dependence on number density and results in a ratio quantity that is a strong function of temperature. The current WMS implementation utilizes 2f (2^{nd} harmonic) detection with 1f (1^{st} harmonic) normalization for calibration-free measurements. To determine the temperature sensitivity of the 2f/1f signals, a brute force simulation approach was applied which incorporates thorough characterization data of each laser to accurately simulate the laser output intensity and wavelength **[20]**. The spectral data used for these simulations is taken from the HITRAN Hitemp 2010 spectral database with minor modifications to incorporate additional data in the literature. For the current work two output frequencies around 4029 cm^{-1} and 3920 cm^{-1}. The lasers were modulated at 100 kHz and 75 kHz, respectively, with a scan frequency of 1 kHz. This results in a sensor response on order of 1 kHz (currently only using up-scans for data processing). Modulation depths were selected to achieve a modulation parameter m=2.2, which typically is associated with the highest 2f/1f signal peaks. Simulations for one wavelength are presented in Fig. 55, showing the simulated laser output intensity, transmitted intensity, and extracted 2f and 1f signals. These simulations are repeated over a range of temperatures (for a given pressure) and are used to determine the necessary 2f/1f peak versus temperature correlations used to calibrate subsequent data.

TDLAS Demonstration Data

WMS TDLAS data was acquired for scaled high-power conditions at three pressures of 80, 100 and 150 psi. This data was acquired simultaneously (but not synchronously) with dual-TC and ITP pressure measurements for direct comparison. Simulations performed prior to this testing determined that one of the selected lines was more suited for low to moderate pressure measurements due to the relatively large linewidth and pressure broadening that occurs. As such, the current TDLAS application is most suited for the 75psia case. Sample 2f/1f profiles for each wavelength are show in Fig. 56a. Peak values for each of these profiles is extracted and used to determine the temperature based on the spectral simulation results. Fig. 56b presents a 1 sec time series of WMS TDLAS derived temperature data for the 75-psi test condition. This data is presented as the normalized temperature deviation from the mean. Overall the signal quality and signal-to-noise ratio for the 2f/1f WMS scheme was good and sufficient to achieve quality results. However, the calculated temperature was determined to be significantly lower than the expected absolute value based on simple adiabatic flame temperature calculations. Examination of the data, data processing and spectral data used for the modeling does not show an obvious reason for the discrepancy. It is thought that this temperature difference arises from a combination of mixing and dilution by the nitrogen purge resulting in cold spots along the pathlength, inaccuracies in the spectral data used for the simulations, and other small approximation errors. The purge dilution is expected to be the largest source of apparent error.

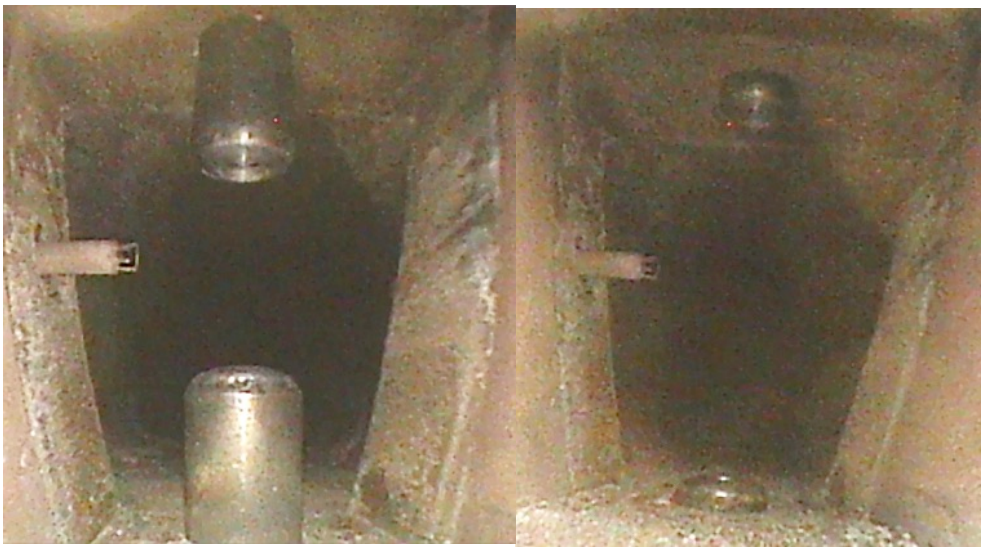

Figure 54. TDLAS and Dual-TC probe installed in rig (view is forward looking aft): (left) initial probe configuration tested with 1” separation, (right) final configuration with 2.5” separation

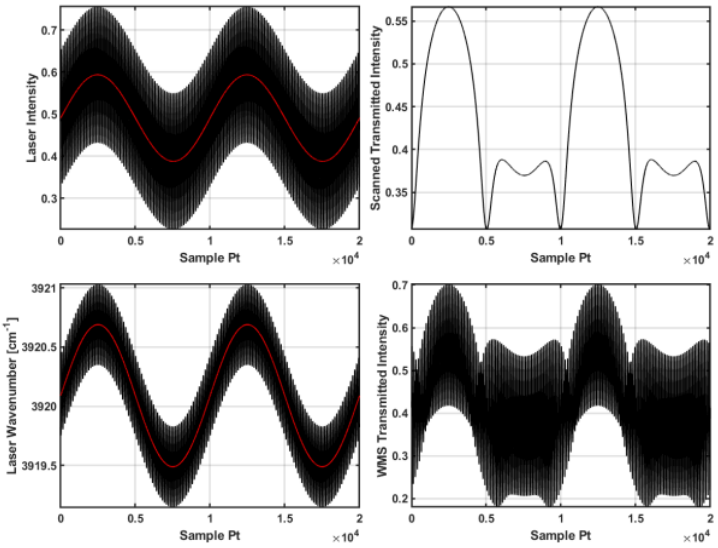

(a) Simulated Laser output intensity and wavelength, transmitted laser intensity

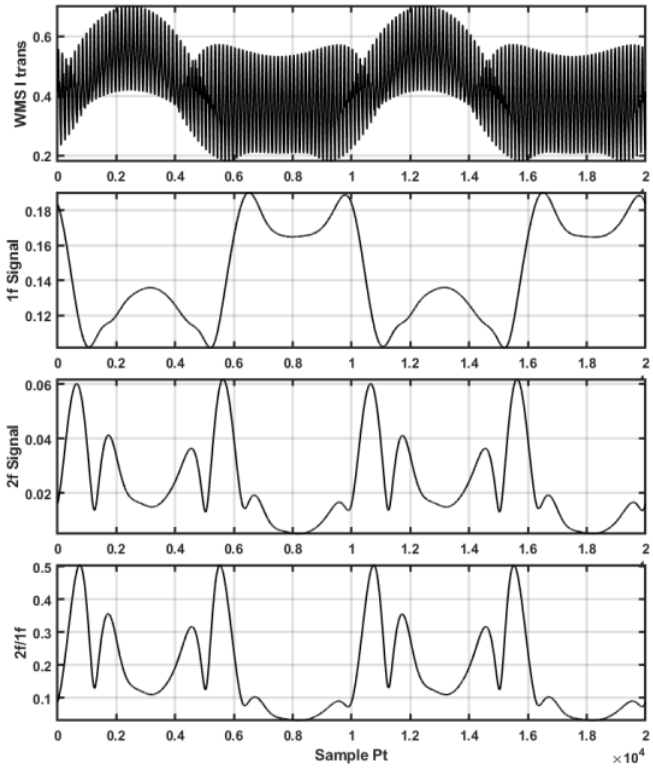

(b) Extracted WMS 2f, 1f and 2f/1f signals using lock-in filter

Figure 55. Simulated laser output signals (a), and resulting harmonic signals after lock-in filter applied (b)

-

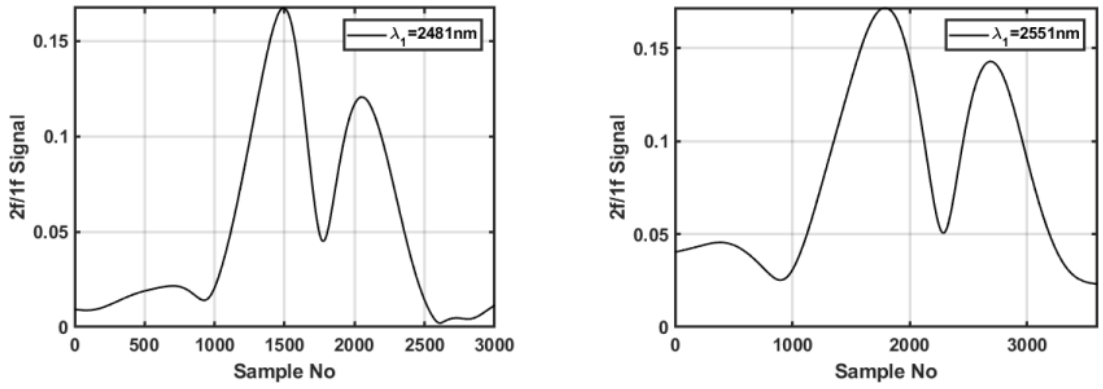

(a) Extracted 2f/1f profiles for both wavelengths

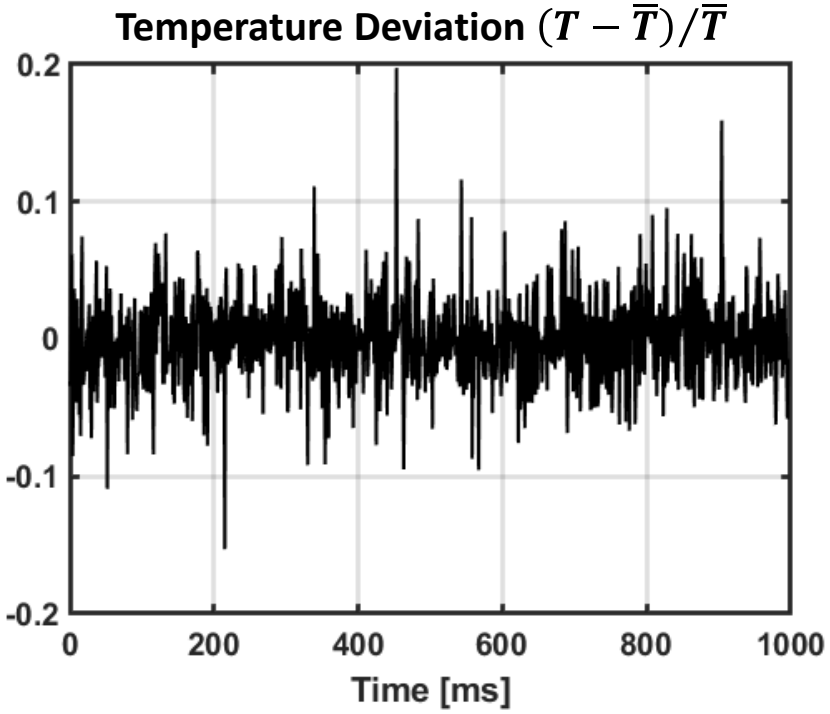

(b) Normalized temperature deviation $(T-\overline{T})/\overline{T}$

Figure 56. Representative WMS TDLAS results for 80 psia scaled high-power condition

TDLAS / Dual-TC Comparison

Figure 57 shows the comparison of the TDLAS temperature measurement with the dual-TC measurements for a range of pressures from 80 to 150 psia for the larger TDLAS probe separation distance of 2.5 inches (Fig. 54 right side). The configuration was the N+3 combustor with both the pilot and mains were fuel (conditions are listed in the figure, but do not correspond to any specific N+3 operating condition). The plots are similar to Fig. 53 which gave the initial dual-TC measurement result (with the smaller probe separation of one inch, Fig. 54 left side)

Unlike Fig. 53 (pilot only), the dual-TC time domain plots (left side of the figure, red and blue lines) are noticeable lower than the adiabatic flame temperature, T_4. This suggests that the addition of the main combustion zone introduces locally cold areas compared with the pilot only operation which the data suggests is well mixed. Without surveying the plane, it is not possible to be conclusive as to why the pilot/main data is significantly lower than T_4.

The TDLAS results are shown as the black lines in the time and frequency domain plots. For all operating pressures, the TDLAS derived temperature is significantly lower than the adiabatic flame temperature (time domain plots). As mentioned above, it is suspected that the TDLAS measurement in strongly influenced by the nitrogen purge within the sight tubes. During the current testing, this purge flow was kept relatively low, with a jet momentum flux ratio less than 0.1. This conservative set point was selected out of concern for the impact of the nitrogen purge interacting with the freestream. It is thought that perhaps the purge was in-fact too low and was not adequately purging the full length of the 8" sight tubes. This ultimately resulted in cold spots along the absorption path, outside of the hot combustion freestream, that reduced the line-of-sight averaged temperature. In addition, the 3920 cm^{-1} absorption feature used for these tests is particularly sensitive to low temperature regions potentially exacerbating the issue.

The fluctuation component of the TDLAS is evaluated by plotting the spectrum of the normalized deviation from the mean temperature measurement (plots on the right side of Fig. 57). At lower pressure (see 80 psia, top right plot), the agreement with the corrected dual-TC measurement is excellent. The additional scatter in the TDLAS data is due to the limited record length (2 sec versus 30 sec for the dual-TC probe). In addition, the TDLAS signal that is low-pass filtered at f_τ with a one-pole Butterworth filter is shown as the green lines. The purpose of this filtering is to simulate the 0.003 in diameter thermocouple response. Comparing the green and red lines in the time and frequency domain show reasonable agree (other than the mean value) which further indicates the TDLAS system is performing well.

As the pressure is increased to 100 and 150 psia, the spectral agreement between TDLAS and the dual-TC does degrade mostly due to the increased noise in the TDLAS signal. Specifically, as pressure increases the 2f/1f normalized TDLAS peaks will decrease due to impacts of pressure broadening. This reduced signal ultimately reduces the signal-to-noise of the TDLAS signal causing the apparent magnitude of the spectrum to increase relative to the dual-TC probe.

In summary, the TDLAS system has been successfully implemented in the harsh and complicated combustor environment, and the WMS 2f/1f scheme performed well in drastically reducing the non-resonant noise sources (i.e. combustion emission, beam steering and

vibrations). While the absolute temperature derived from the TDLAS was lower than expected, this is attributed to cold spots along the absorption path that need to be further investigated.

Recommended Improvements

A number of improvements and questions for further investigation have been identified as a result of this work, including:

- Select an alternative absorption line to the 3920 cm^{-1} used for the current work. A number of other candidate absorption features are available with higher lower state-energy and lower broadening coefficients. This will reduce the influence of low temperature regions along the absorption path and will also improve the TDLAS probe performance at higher pressures. One such candidate would be around 4041 cm^{-1} but requires the procurement of another laser diode.

- Perform more investigation of the influence of purge flow by completing a parametric study of the TDLAS line of sight averaged temperature over a wide range of purge flows, low to very high. This would provide better understanding of the optimal settings for probes with this sort of purge.

- Refine the probe design and eliminate the need for purge by relocating the window to the probe tip. This would require a more complicated high temperature window design but would completely eliminate the need for precise purge along the length of the sight tube. In addition, integration of the optical elements closer to the probe tips, versus outside of the rig, would reduce the impact of vibrations considerably.

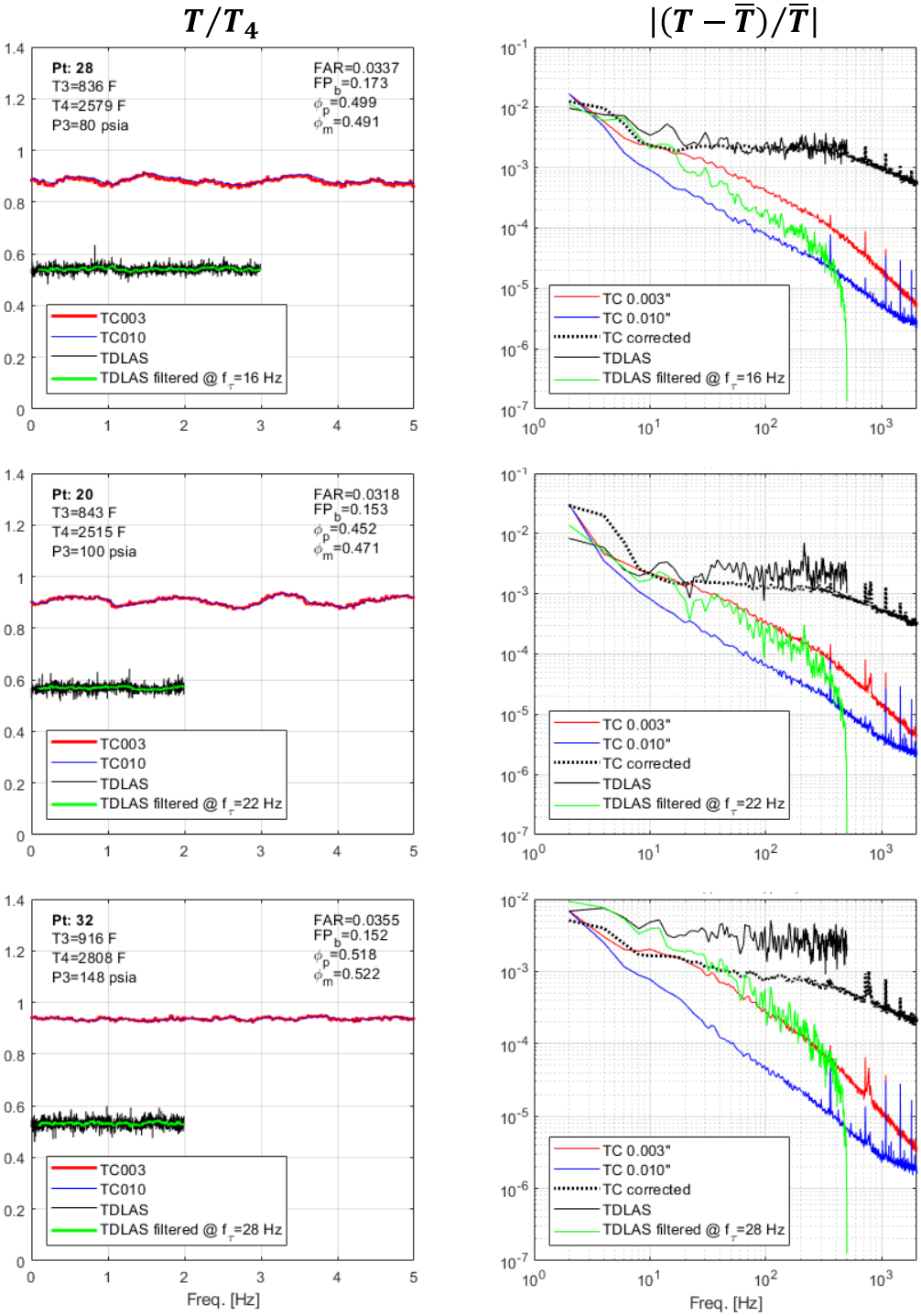

Figure 57. TDLAS comparison with dual-TC probe results over range of pressure

Summary

This program has developed a first of its kind database of detailed unsteady measurements characterizing noise sources of advanced (N+3) low-emissions aero-combustors. The program addresses the need for fundamental combustion noise experiments which, in the near term, enable improvements to reduced-order models for use in system level noise assessments at the preliminary design stage for advanced air transport vehicles. In the long term, this program addresses validation needs of high-fidelity prediction methods suited for detailed multi-disciplinary acoustics/emissions combustor design.

The key finding of this study was a modified pressure scaling which employs a model-based acoustic transfer function to relate combustor dynamic pressure to unsteady heat release was found to enable legacy scaling laws over a wide range of the N configuration (RQL-type combustor) and the N+3 configuration. Positive *FAR* excursions were found to deviate from the legacy scaling laws and actually reduced the noise level apparently by improving the flame stability. Such results may suggest broadband combustor noise reduction strategies for advanced aero-combustors.

Comparison to legacy spectrum scaling showed in many cases similarity to the N and N+3 configuration data, but notable difference occurred for the N+3 configuration, particular for combustion parameter sweeps that tended to destabilize the main RJIC flame (e.g., reduced T_3)

UHR (Unsteady Heat Release) imaging (via chemiluminescence) was used to compute the direct noise field and perform multi-point statistical analysis of the UHR field. Comparison of the computed direct noise field to measured surface dynamic pressures suggests the indirect noise field was a significant component of the total dynamic pressure inside the combustor for this study.

References

1. Berton, J., Envia, E. and Burley, C., "An Analytical Assessment of NASA's N+1 Subsonic Fixed Wing Project Noise Goal," AIAA Paper 2009-3144.

2. Hultgren, L.S., "Core-Noise Research: Aircraft Noise Reduction Subproject – Emerging Technology Challenges," NASA Acoustics Technical Working Group, April 2015.

3. McKinney, R.G., Sepulveda, D., Sowa, W., and Cheung, A.K., "The Pratt &Whitney TALON X Low Emissions Combustor: Revolutionary Results with Evolutionary Technology", Aerospace Sciences Meeting, January 2007.

4. "Low NOx Fuel Flexible Combustor Integration," NASA Contract NNC10BA12B, Pratt & Whitney, Kramer, S., May 23, 2013.

5. "Fuel Flexible Combustor for High-OPR, Compact-Core N+3 Propulsion Engine – Charts for Green Aviation presentation", March 2016.

6. "Fuel-Flexible Combustor for High-OPR Compact Core N+3 Propulsion Engine," NASA Contract NNC14CA30C, United Technologies Research Center, Smith, L.L., September 30, 2014.

7. Lord, W.K., Suciu, G.L., DiOrio, A.G., Greitzer, E.M., & Tan, C.S., "Aircraft and Technology Concepts for an N+3 Subsonic Transport Phase II: Final Report on High-Efficiency, High-Pressure Ratio Small Core Engines," NASA Contract NNX11AB35A, Final Report, October 2014.

8. Smith, L.L., "Fuel Flexible Combustor for High-OPR Compact-Core N+3 Propulsion Engine," NASA Contract NNC14CA30C, Final Report, September 2019.

9. Mishra, A., Bodony, D. J., "Evaluation of Actuator Disk Theory for Predicting Indirect Combustion Noise," *Journal of Sound and Vibration*, Vol. 332(4), pp. 821-838, February 2013.

10. Ihme, M., Bodony, D.J., and Pitsch H., "Prediction of Combustion-Generated Noise in Nonpremixed Turbulent Jet Flames using Large-Eddy Simulation," AIAA Paper 2006-2614, 12th AIAA/CEAS Aeroacoustics Conference, Cambridge, MA, 2006.

11. Mathews, D.C. and Rekos, N.F., "Prediction and Measurement of Direct Combustion Noise in Turbopropulsion Systems," *Journal of Aircraft*, Vol. 14, No. 9, September 1977, pp. 850-859.

12. Ho, P.Y. and Doyle, V.L., "Combustion Noise Prediction Update," AIAA Paper 79-0588, AIAA 5th Aeroacoustics Conference, Seattle, WA, 1979.

13. McCormick, D.C., et al., “Acoustics of Future Low-Emissions Combustor Technology”, Sep. 2016-Sep 2017 Annual Report, NRA NASA Contract NNC16CA39C.

14. Culick, F. E. C., "Combustion Instabilities in Liquid-Fueled Propulsion Systems – A Overview," Paper No.1, AGARD Conference Proceedings No. 450, October 1988

15. Crighton, D.G., Dowling, A.P., Ffowcs Williams, J.E., Heckl M. and Leppington, F.G, Modern Methods in Analytical Acoustics, Springer-Verlag, 1992.

16. Morse, P.M. and Ingard, K.U., “Theoretical Acoustics”, Princeton University Press, 1986, p. 555.

17. Gordon, G., “Acoustic Database for Turbofan Engine Core-Noise Sources, Volume I—Final Report”, NASA/CR – 2015-218879/VOL1, September 2015.

18. Strahle, W.C. and Muthukrishnan, M., “Thermocouple Time Constant Measurement by Cross Power Spectra”, AIAA Journal, Technical note, Nov. 1976, Vol. 14, No. 11, pp 1642-1644.

19. Goldenstein, C. S., Spearrin, R. M., Jefferies, J. B., and Hanson, R. K., “Wavelength-modulation spectroscopy near 2.5 um for H_2O and temperature in high-pressure and – temperature gases,” Applied Physics B DOI: 10.1007/s00340-013-5751-1, 2014

20. Sun, K., Chao, X., Sur, R., Goldenstein, C. S., Jefferies, J. B., and Hanson, R. K., “Analysis of calibration-free wavelength-scanned modulation spectroscopy for practical gas sensing using tunable diode lasers,” Measurement Science and Technology 24, 12 2013